Materials Design of High Nitrogen Manganese Austenitic Stainless TWIP Steels for Strip Casting

Von der Fakultät für Georessourcen und Materialtechnik

der Rheinisch -Westfälischen Technischen Hochschule Aachen

zur Erlangung des akademischen Grades einer

Doktorin der Ingenieurwissenschaften

genehmigte Dissertation

vorgelegt von Dipl.-Ing.

Linda Mosecker

aus Oschatz

Berichter:

Univ.-Prof. Dr.-Ing. Wolfgang Bleck

Prof. Dr. rer. nat. Joachim Mayer

Tag der mündlichen Prüfung: 22. April 2016

Diese Dissertation ist auf den Internetseiten der Hochschulbibliothek online verfügbar

-- Thank you all-- HMMGT

Abstract

High nitrogen manganese austenitic stainless TWIP steels achieve attractive mechanical properties and excellent strain hardening behavior. However, high nitrogen steel melting methods are generally associated with high pressures to enhance the nitrogen solubility in the melt. Thin strip casting offers an attractive option that not only shortens the process route but also allows the alloying with nitrogen at atmospheric pressure. In the present work, the materials design of austenitic Fe-Cr-Mn-N steels for the production by strip casting is presented. A thermodynamics based model using CALPHAD method was developed to predict and control the thermal and mechanical stability of the austenitic phase by calculating the Gibbs free energy change ($\Delta G^{\gamma \to \varepsilon}$) and the stacking fault energy (SFE). The application of a non-constant composition-dependent interfacial energy, $\sigma^{\gamma/\varepsilon}$, is introduced and the effect of higher ordered interaction parameter and strain energy term on SFE is discussed. Fe-Cr-Mn-N alloys with nominal chemical composition in the range of 13-14 wt.% Cr, 20-26 wt.% Mn and 0.4-0.6 wt.% N were melted and processed by strip casting in laboratory and industrial scale. The solubility of nitrogen in the melt and the phase stability during solidification at atmospheric pressure are predicted by thermodynamic model calculations as function of balanced chromium to manganese concentration. The as-cast and cold-rolled microstructure is characterized by light optical microscopy and electron probe microanalysis to analyze the secondary dendrite arm spacing, grain size distribution and microstructure segregation. The phase distribution and deformation substructures with respect to character and location of grain and sub-grain boundaries, distribution of grain orientation and local variations in residual strain are determined by X-ray diffraction and electron back-scatter diffraction. The deformation mechanisms and mechanical properties of the investigated Fe-Cr-Mn-N alloys are discussed to depend on temperature, SFE and ordered microstructural phenomena like short range ordering (SRO). Differences in the strain hardening behavior of the as-cast and cold-rolled/recrystallized strip material are explained by the change in grain size, differences in the density and distribution of the dislocation substructure and the critical stress for the onset of deformation twinning. The flow behavior is homogenous and no serrations in the flow stress occur during tensile deformation in the temperature range from -150 to 250°C. The absence of dynamic strain aging is attributed to the type of SRO and the activation energy for reorientation of the point defects, rather than the SFE. The RT SFE of the examined steels is determined between 24-31 mJ/m² which defines mechanical twinning as the dominant secondary deformation mechanism, resulting in high work hardening rate and formability. The occurrence of high temperature deformation twinning at 250°C is explained by the effect of nitrogen on the dislocation arrangements and the probability of Cr-N SRO. It is assumed that with increasing the interstitial nitrogen content the effect of SFE on the activity and character of mechanical twinning becomes less dominant, and the temperature sensitivity of the yield strength within the thermal and athermal temperature range increases. In comparison to conventional high-Mn TWIP steels, the investigated high nitrogen Fe-Cr-Mn alloys exhibit extra-ordinary high flow stress and strain hardening behavior, with YS up to 660 MPa and total elongation A50 of 47 %, meeting the requirements for application in automobile industry.

Kurzzusammenfassung

Austenitische hoch-stickstofflegierte TWIP Stähle weisen attraktive mechanische Eigenschaften und ein exzellentes Verfestigungsverhalten auf. Die konventionelle schmelzmetallurgische Herstellung stickstofflegierter Stähle erfolgt in der Regel im Vakuum unter hohen Drücken, um eine hinreichende Löslichkeit von Stickstoff in der Schmelze zu realisieren. Das Dünnbandgießen stellt dabei eine vielversprechende Alternative dar, mit der neben einer drastischen Verkürzung der Prozessroute auch ein Legieren mit Stickstoff bei Atmosphärendruck möglich ist. In der vorliegenden Arbeit wird eine Methode für das Legierungsdesign austenitischer Fe-Cr-Mn-N Stähle zur Herstellung über das Dünnbandgießen vorgestellt. Auf Basis thermodynamischer Berechnungen der Gibbs Energie ($\Delta G^{\gamma \rightarrow \varepsilon}$) und Stapelfehlerenergie (SFE) unter Verwendung der CALPHAD Methode wurde ein Model zur Vorhersage und kontrollierten Einstellung der thermischen und mechanischen Phasenstabilität entwickelt. Eine variable, legierungsabhängige Grenzflächenenergie, $\sigma^{\gamma/\varepsilon}$, wird definiert und der Einfluss von Wechselwirkungsparametern höherer Ordnung sowie die Berücksichtigung eines Dehnungsenergie Terms auf die SFE diskutiert. Fe-Cr-Mn-N Legierungen mit nomineller chemischen Zusammensetzung im Bereich von 13-14 Gew.% Cr, 20-26 Gew.% Mn und 0.4-0.6 Gew.% N wurden über Bandgießen im Labor- und Industriemaßstab hergestellt. Die Stickstofflöslichkeit in der Schmelze und die Phasenstabilität während der Erstarrung bei Umgebungsdruck wird mithilfe thermodynamischer Modelle als Funktion des Chrom-Mangan Gehaltes berechnet. Die Charakterisierung der Gefüge im Guss- und kaltgewalzten/ rekristallisierten Zustand der Bleche hinsichtlich des sekundären Dendritenarmabstandes und der Korngrößen- verteilung erfolgt mittels Lichtmikroskopie und Elektronenstrahlmikroanalyse. Die Analysen der Phasenverteilung und Verformungsmikrostrukturen in Bezug auf den Charakter und die Lage von Korn- und Subkorngrenzen, die Verteilung von Körnern mit unterschiedlicher Orientierung und lokale Dehnungsunterschiede erfolgen mittels Röntgenbeugungsanalyse und Elektronenrückstreu- beugung. Die Verformungsmechanismen und mechanischen Eigenschaften der untersuchten Fe-Cr-Mn-N Stähle werden in Anhängigkeit von der Temperatur, der SFE und Nahordnungsphänomenen (SRO) diskutiert. Die Unterschiede im Verfestigungsverhalten der Bleche im Guss- und kaltgewalzten/ rekristallisierten Zustand wird anhand der Korngröße, Dichte und Verteilung von Versetzungssubstrukturen und der kritischen Spannung für den Beginn der Zwillingsbildung erörtert. Das Fließverhalten im quasistatischen Zugversuch für den untersuchten Temperaturbereich zwischen -150 to 250°C ist homogen; Instabilitäten in der Fließkurve treten nicht auf. Die Absenz der Reckalterung wird auf die Art der Nahordnung und die daraus resultierende Aktivierungsenergie der Neuorientierung der Punktdefekte zurückgeführt. Die SFE der untersuchten Stähle bei Raumtemperatur wird zwischen 24-31 mJ/m² benannt und die mechanische Zwillingsbildung als dominanter sekundärer Verformungsmechanismus definiert. Daraus resultiert eine hohe Verfestigungsrate und Verformbarkeit der Materialien. Das Auftreten von mechanischer Zwillingsbildung im hohen Temperaturbereich um 250°C wird mit dem Einfluss von Stickstoff auf die Versetzungsbildung und –anordnung sowie auf die Wahrscheinlichkeit der Ausbildung von Cr-N SRO erklärt. Es wird angenommen, dass mit zunehmendem Gehalt an gelöstem Stickstoff der

Einfluss der SFE auf die Aktivität und den Charakter der Verformungszwillinge geringer ist. Die Temperatursensitivität der Streckgrenze im thermischen und athermischen Temperaturbereich nimmt mit höherem Stickstoff Gehalt zu. Im Vergleich zu konventionellen hoch Mangan TWIP Stählen, zeichnen sich die untersuchten hochstickstofflegieren Fe-Cr-Mn Stähle durch außergewöhnlich hohe Fließspannungen und ein hervorragendes Verfestigungsvermögen mit Streckgrenzen bis zu 660 MPa und Dehnungen bis 47 % aus; was diese Stähle außerordentlich attraktiv für ein breites Anwendungsspektrum im Automobilbereich macht.

Table of contents

1   Introduction

The application of conventional austenitic stainless steels in automobile industry is limited mainly due to the higher costs of the alloyed nickel [1]. Therefore, the replacement of nickel by manganese has been found advantageous to achieve an attractive property/cost balance [2]. High-manganese stainless twinning induced plasticity (TWIP) steels offer high potential for application e.g. in car bodies due to an excellent combination of strength, ductility and strain hardening behavior [3].
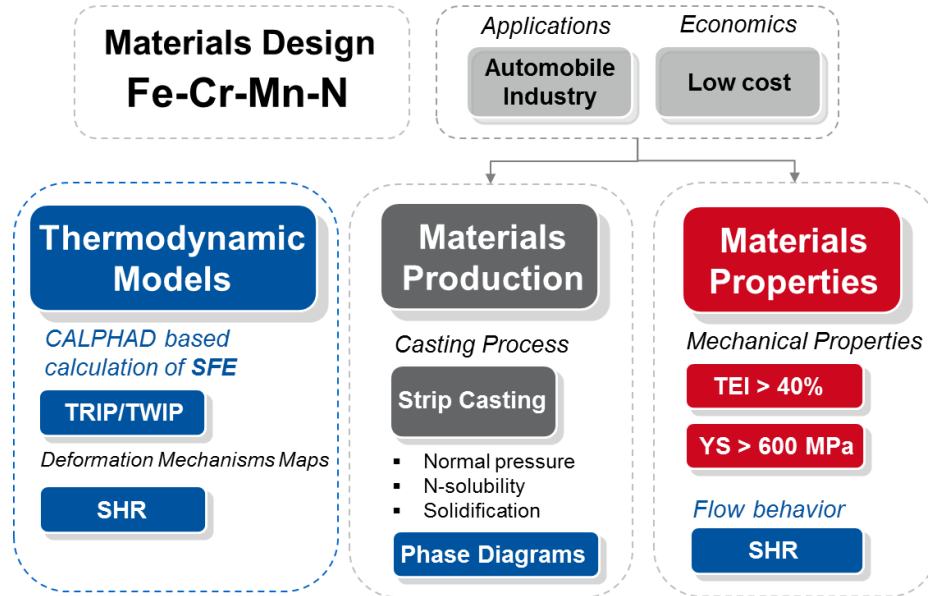
Figure 1 Systematic structure of the materials design approach for austenitic stainless Fe-Mn-Cr-N TWIP steels produced by strip casting.

The thermodynamic stability of the austenitic microstructure is obtained mainly by alloying nitrogen to the Fe-Cr-Mn system, which enhances strength, ductility and localized corrosion [1][2]. In these steels, chromium is added to achieve the corrosion resistance. Moreover, chromium increases the solubility of nitrogen in the melt [4] which is of main interest for the production of these steels by strip casting under atmospheric pressure. In the current work the material design of high-nitrogen Fe-Cr-Mn TWIP steels was defined as threefold model to goal the application and economics requirements (Figure 1). Three main questions can be addressed as the aim of this work:

Thermodynamic Models Development of a CALPHAD based model to predict and control the thermal/ mechanical stability of the austenitic phase in the Fe-Cr-Mn-N steels by calculating the Gibbs free energy change $\Delta G^{\gamma \to \varepsilon}$ and the stacking fault energy (SFE).

Materials Production Strip casting of the material under normal pressure without solidification through the delta-ferrite region, by regulation of the nitrogen solubility and phase stabilities over a wide temperature range as function of the chemical composition.

Mechanical Properties Adjusting the mechanical properties to the requirements for automobile application: yield strength > 600-700 MPa for crash assemblies [5] and total elongation > 40% with analyzing the characteristic deformation behavior.

2 Theoretical fundamentals

2.1 High nitrogen austenitic stainless steels

High nitrogen stainless twinning induced plasticity (TWIP) steels have been found to achieve attractive mechanical properties, high energy absorption capacity and excellent strain hardening behavior. Besides, the combination of high resistance to strain induced martensite formation, low magnetic permeability, and favorable localized corrosion properties in addition to wet corrosion resistance, high nitrogen containing austenitic stainless steels are used in power generation, pulp and paper industry, transportation industry (ship building) and petrochemical industry [6]. For the use in automobile applications, the steel exhibits high strength, fracture toughness and energy absorption potential that allows light weight designs, reducing fuel consumption as well as emissions [7]. Furthermore, the austenitic structure of the steel provides a good toughness at low temperatures, allowing application in cryogenic environments, like superconducting magnet housings [6][8]. Since the steel is non-magnetic and has a low induced radio activity, it can be used in vacuum vessel of fusion reactors [9]. Due to its high strength and corrosion resistance medicine and food industry are further area of application [10]. The strong austenite stabilization effect of nitrogen leads to increased resistance against stress corrosion cracking and hydrogen embrittlement, which is of main importance as it causes delayed fracture. In comparison to conventional high-Mn TWIP steels [11]-[13], the homogenous flow and work hardening characteristics of Fe-Cr-Mn-N steels indicate differences in the strain-induced hardening mechanisms. The occurrence of Cr-N SRO phenomena [14]-[16] and the resultant interactions with dislocations and stacking faults are believed to play a major role in the deformation behavior of these alloys. The strong affinity between Cr and N atoms generates Cr-N SRO clusters. Oda *et al.* [14] suggested that N in the austenitic Fe-1.5Mn-15Cr-15Ni alloy gathers around Cr atoms to form interstitial-substitutional complexes; analyzed using X-ray absorption fine structure analysis. More recently, Li *et al.* [17] reported Cr-N SRO in the Co-29Cr-6Mo-(0.1-0.16)N alloy based on results of atom probe tomography. Moreover, Cr-N SRO is assumed to influence the energy barrier for the γ->ε phase transition [17], which along with the stacking fault energy (SFE), is relevant to the deformation mechanisms and mechanical behavior of Fe-Cr-Mn-N steels. The composition and temperature dependent SFE strongly influences the plasticity mechanisms and work hardening behavior of austenitic high-Mn steels [11]-[13][18]. Increasing the SFE causes the active deformation mechanisms to change from strain-induced martensite formation and dislocation glide, to mechanical twinning and dislocation glide, and to pure dislocation glide [19]. The effect of N additions on the SFE in Fe-Cr-Mn steels is reported to be non-monotonic, exhibiting a minimum SFE at ~0.4 wt.% N in Fe-15Cr-17Mn [20][21] and Fe-20Cr-17Mn [22] alloys. The decrease in SFE at low N contents was explained due to the segregation of interstitial N atoms to stacking faults [23]. While at higher N contents the SFE increases as the bulk effect becomes more pronounced [21]. Furthermore, segregation effects of N to dislocations and stacking faults [20][23], Cr-N SRO [24] and the distribution of alloying elements within the *fcc* lattice are also reported to affect the SFE [16]. In addition, the experimental method of SFE measurement may also affect the SFE values. For instance, the method of measuring the SFE by analyzing the geometry of extended three-fold nodes using transmission electron microscopy (TEM) was found to overestimate the SFE in Fe-Cr-Ni alloys [25]. Recent analysis on the impact of nanodiffusion on SFE in Fe-Mn-C alloys using *ab initio* calculations in combination with *in situ* TEM analysis [26], reveal promising approaches to understand the microstructure phenomena that control the behavior of austenitic Fe-Cr-Mn-N alloys.

2.1.1 Production of high nitrogen stainless steels

In the production of high nitrogen austenitic stainless steels two main problems appear that make the melting process challenging, in order to achieve the desired advantages of the material. The nitrogen solubility of 0.045 wt.% in liquid iron at 1600°C [27] at atmospheric pressure is very low [28]. Hence high nitrogen steel melting methods are generally associated with high pressures to enhance the nitrogen solubility in the melt [29]. The effect of gaseous nitrogen pressure on the nitrogen solubility limit in Fe-13Cr-22Mn is presented in **Figure 2.1-1a**.
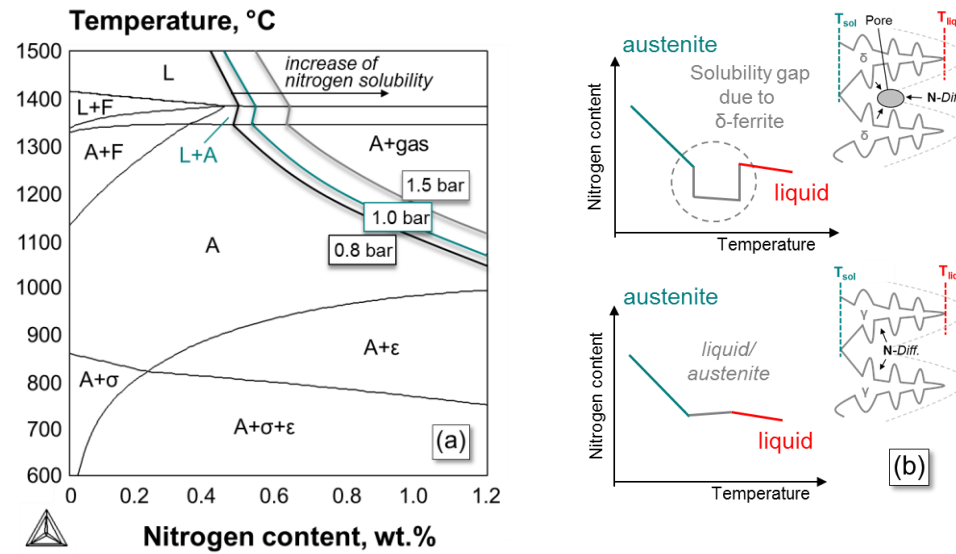
Figure 2.1-1 Phase equilibrium and nitrogen solubility limit as function of gaseous nitrogen pressure in a Fe-13Cr-20Mn steel (a) and schematic temperature dependence of nitrogen solubility due to the formation of δ-ferrite (b) after [28].

In order to induce high nitrogen concentrations into the melt chromium is added to increase the solubility at high temperatures (**Figure 2.1-2**). However, chromium is a strong δ-ferrite stabilizer at the same time. The δ-ferrite solidification in iron alloys is associated with a wide solubility gap and a sudden drop of nitrogen solubility in the melt (**Figure 2.1-1b**). This leads to the formation of pores and outgassing of nitrogen, which results in degraded surface quality of the strip and the loss of nitrogen in the austenitic microstructure [28]. Related to the hot-rolling process, δ-ferrite volume fractions between 10-40 vol.% are regarded critical, particularly if the δ-ferrite is within the strip surface [30]. Tarboton *et al.* [31] proposed an empirical equation, Eq. (2.1), to predict the occurrence of δ-ferrite at 1250°C for Fe-Cr-Mn-N steels. The predictive ability exhibits a mean absolute error of 2.9 vol.% and can be applied within 8-20wt.% manganese; therefore the application for high alloyed systems is limited.

$$\delta\text{-ferrite [vol.\%]} = 31.24 - 262.6C(wt.\%) + 1.535Mn(wt.\%)\ldots \qquad (2.1)$$

The only element that enhances the nitrogen solubility in the melt, as well as suppresses the formation of δ-ferrite during solidification, is manganese. The effect of manganese is known to be two times less the effect of chromium on the nitrogen solubility in Fe-Cr-Mn-N alloys [32].

Additions of chromium and manganese increase, and nickel reduces the nitrogen solubility. In general, the nitrogen solubility in Fe-Cr-Mn alloys is much higher than in Fe-Cr-Ni alloys with comparable chromium contents [27]. At high alloying contents, a marked deviation from Sieverts' law is observed, indicating that at high nitrogen concentrations the conditions of the infinite dilute is not applicable anymore; nitrogen exhibits a negative influence on its own solubility [33].
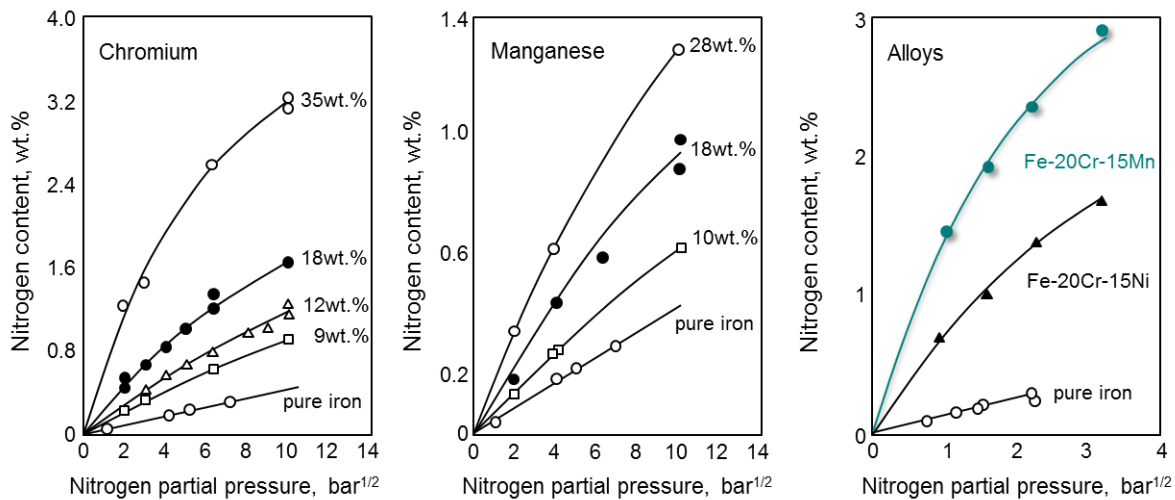

Figure 2.1-2 Effect of chromium and manganese on the nitrogen solubility
in pure iron [34] and iron alloys [27].

In the newly designed di-interstitial Fe-Cr-Mn-CN alloys, carbon is added to achieve a primary austenitic solidification in order to avoid nitrogen degassing in all processing steps [7]. The careful adjustment of the interstitial carbon and nitrogen content and in particular the carbon/nitrogen ratio was found to play a major role to control the degassing of nitrogen in these alloys. The widening of the austenitic phase field due to the carbon and nitrogen alloying was found to be more effective than for only nitrogen alloying [7][21]. However, carbon contents > 0.1 wt.% decrease the weldability of the material, which is of main importance for automotive applications.

Until now, the standard facilities used for nitrogen alloying in the molten state are induction or electric arc furnaces, (pressure) electro slag remelting furnace (ERS), argon oxygen decarburization (AOD) converter, plasma arc and high-pressure melting with hot isostatic processing (HIP) [6][2]. These techniques however are cost-intensive, which is one of the main reasons that high nitrogen stainless steels could not yet be established in the price-controlled automobile industry. Thin strip casting offers an attractive option that not only shortens the process route but also allows nitrogen alloying within the equilibrium solubility limit at atmospheric pressure. As the solubility of nitrogen in the melt is strongly dependent on the temperature, pressure and chemical composition. Therefore, the production of high nitrogen stainless steels by strip casting at normal conditions (atmospheric pressure of 1 bar) requires a balanced control of the chemical composition and precise adjustment of the casting conditions. In comparison to continuous strip casting with conventional technologies, the thin strip casting represents a new generation of efficient and economic casting technology to supply steel strip products of high quality at low cost [35]. Over the last decade enormous investments in the development of strip casting process have been made, due to the high potential to substantially

reduce the investment cost of steel strip production. The strip production directly from the melt offers different advantages. Due to the small strip thickness, the hot rolling effort is reduced to a minimum and the process route can be considerably shortened [36]. Hence, the strip casting process allows to produce strip with a thickness less than 1.8 mm at a stable cost [35]. One main problem for the production of high manganese steels is the strong segregation behavior of manganese that leads to heterogenic microstructure; disadvantages to the mechanical behavior. The rapid solidification during strip casting enables the production of high manganese steels with very short wavelength microsegregations, microstructure homogeneity and smaller inclusion size [36][37]. However, the high casting velocity requires an accurate control of the process parameters. Even minor deviations lead to a substantial deterioration of the strip quality, such as surface cracks or uneven strip thickness [35]. Austenitic stainless steels [37]-[39] and high manganese TWIP steels [36][40] have been already produced via strip casting as reported in literature for various chemical compositions. Besides, there are minor publications for austenitic high nitrogen stainless steels. The latest work was presented by Liu *et al*. [41] related to the development of the Fe-25Mn-22Cr-2Si-0.7N steel produced by strip casting and the investigation of the as-cast microstructure.

2.1.2   Yield strength variation in Fe-Cr-Mn-N steels

Several authors have investigated the mechanisms by which additions of nitrogen improves the strength in austenitic stainless steels, while the fracture strain and fracture toughness are not affected at elevated temperatures [42]. The yield strength of nitrogen alloyed austenitic stainless steels consists of the main three constitutes (ΔR): strength of the matrix, grain boundary hardening and solid solution hardening [43]. In **Figure 2.1-3** (left) the contributions to the yield strength are shown as function of nitrogen content after [43].
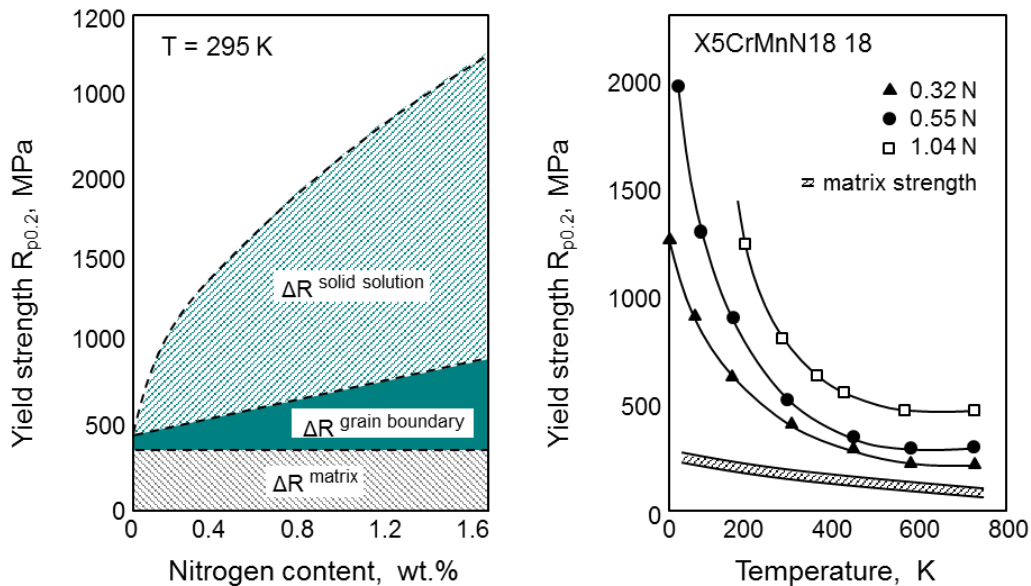

Figure 2.1-3 Yield strength of austenitic steels as function of nitrogen content and temperature. The increase in strength results from the matrix strength, the grain boundary hardening and the solid solution hardening due to the interstitial nitrogen [43][44].

The *matrix strength* correlates to the friction stress of the nitrogen free *fcc* lattice that is mainly controlled by the solid solution hardening of the substitutional elements like chromium and manganese. The impact of the matrix strength to the yield strength is low compared to the grain boundary or solid solution hardening. The yield strength as function of *grain size* follows the standard Hall-Petch relation investigated for conventional high-manganese steels [5] and austenitic Fe-Cr-Mn-N steels [43]. Grain boundaries act as obstacles to the dislocation movement. With decrease in grain size the effective area of grain boundaries increase, which leads to enhanced strength. The grain boundary hardening increases proportionally to the alloyed nitrogen content (**Figure 2.1-3** left). The effect of nitrogen on grain boundary hardening has been explained by the occurrence of planar dislocation structures in high nitrogen austenitic stainless steels [6]. By addition of high nitrogen contents dislocation cross-slip is suppressed in favor of planar dislocation glide [Tera09]. Short range ordering of Cr-N has been considered as primary reason for planar dislocation glide in these steels, besides the SFE [19]. It is observed by Terazawa *et al.* [45] that planar dislocations pile-up against the grain boundary, activating another slip system from the grain boundary in the adjacent grain. The piled-up dislocations cause a marked stress concentration at the grain boundary that results in high grain boundary hardening. The highest impact on the strength results from the interstitial solid solution of nitrogen (**Figure 2.1-3** left). It is assumed that nitrogen alloying of 1 wt.% increases the yield strength about 450 MPa only by the contribution of solid solution [43].

The effect of solid solution strengthening due to interactions of the solute atoms with dislocations mainly derives from dimension mismatching and the effect on the elastic lattice properties [46]. According to Gavriljuk *et al.* [47][48], nitrogen increases the concentration of free electrons promoting the covalent component of the interatomic bonding and the formation of Cr-N SRO. The effect of nitrogen on the electron subsystem by intensifying the metallic character strengthens the binding between immobile interstitial atoms and dislocations [49]. The nitrogen-induced distortion of the metallic sublattice and the change in the electron subsystem leads to a strong blocking of dislocation sources in grains adjacent to those where the slip starts [50], enhancing the strength, ductility and impact toughness [47][48]. After Bazaleeva [49], the interaction between nitrogen atoms and dislocations in *fcc* solid solution is connected presumably with the formation of Suzuki atmospheres on packing defects and explains the more effective blocking of dislocations. Nitrogen additions to steels containing larger chromium concentrations increases both the Young's modulus and the elastic shear modulus [51], the result being attributed to the strong affinity between Cr and N atoms [24]. It is assumed that the SRO zones locally enhance the elastic shear modulus and induce anisotropic elastic strain in the nearest surrounding of nitrogen atoms [24]. In the presence of Cr-N SRO, the dislocation movement requires additional force to pass the local ordered zone, which leads to the increased solid solution strengthening in Fe-Cr-Mn-N steels. Furthermore, nitrogen alloyed steels exhibit distinct temperature sensitivity of the yield strength, **Figure 2.1-3** (right). With decrease in temperature the yield strength increases markedly with the nitrogen content. While at high temperature only small decrease in yield strength is observed, in comparison to carbon alloyed materials that show steadily decrease of yield with increasing temperature [27]. This characteristic behavior of the yield strength as function of temperature in nitrogen alloyed austenitic steels is similar to the performance of *bcc* metals but in contrast to the behavior of *fcc* material [24]. Due to the high strength at low temperatures, nitrogen alloyed austenitic stainless steels are proposed for applications at cryogenic temperatures, such as housings for superconductive magnets [4][27].

The improvement of the yield strength in austenitic steels is further achieved by microstructure adjustment. The main strategies are discussed in the literature refer to: grain size refinement, pre-straining of the cold-rolled/RX material and recovery/ partial recrystallization of pre-strained sheets. With decreasing the mean *grain size* the yield strength of the material can be increased very effectively. As mentioned before, the yield strength as function of grain size is sufficiently described using the Hall-Petch relation [27]. However, industrial process limitations of conventional cold rolling and the recrystallization conditions restrict the minimum of grain size that can be achieved [52]. Besides, the grain size significantly impacts the deformation mechanism and by that the mechanical behavior [19]. It has been shown that in austenitic TWIP steels the strength increases and the elongation decreases as the mean grain size decreases [19][53][54]. After Akbari *et al.* [19], the length, volume fraction and number of deformation twin boundaries increase with grain size in the coarse-grained samples of an Fe-24Mn-0.6C steel (grain size ~100 μm). While at very fine grain size (~2 μm) deformation twinning and dynamic recovery is limited. This is in accordance to Dini *et al.* [53], where grain refinement was found to suppress mechanical twinning in TWIP steels. The enhanced strain hardening behavior and relative high ductility of fine grained TWIP steels was explained by the suppressed dynamic recovery in Fe-Mn-Al-Si alloys [54]. *Cold deformation* of solution treated austenitic stainless steels offers a very effective way to raise the yield strength [44][55]. **Figure 2.1-4a** shows the effect of cold deformation on the yield strength for different Fe-Cr-Mn-N steels, in comparison to conventional type 304, 310 and 316 stainless steels represented as scatter band, after [44].
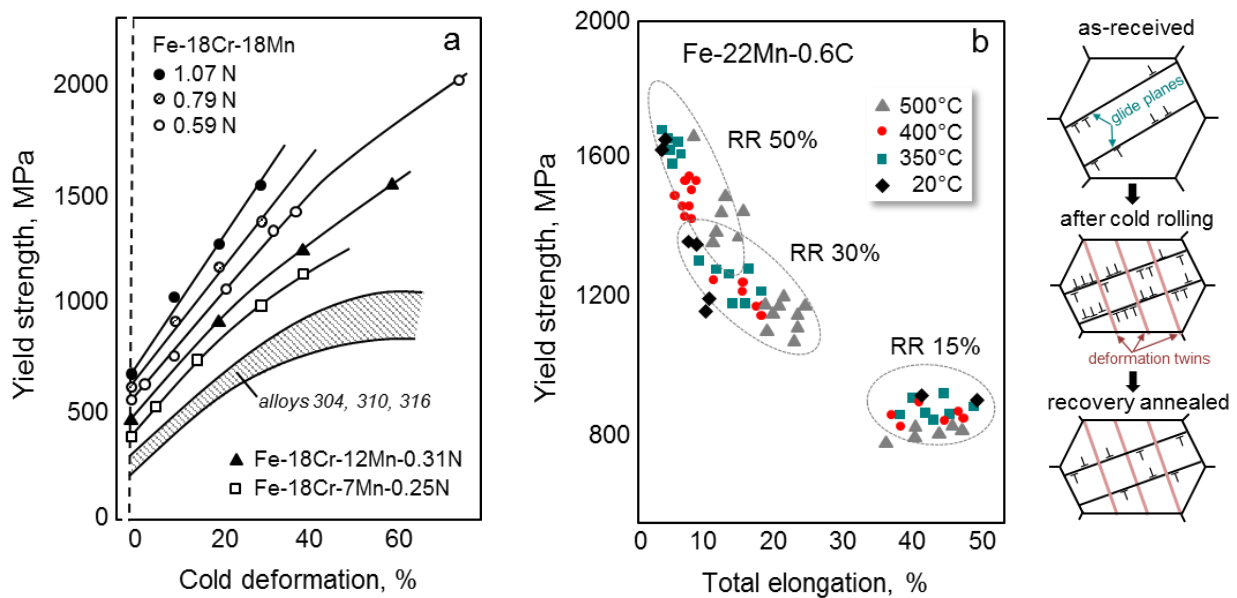
Figure 2.1-4 Yield strength of austenitic steels (a) over degree of cold deformation [44] and (b) after 15%, 30% and 50% cold rolling reduction (RR) followed by recovery annealing at different temperatures for 3-60 min [56][52] and the referred microstructure evolution after [57].

It has been observed that the improvement of yield strength by cold deformation is due to the development of stable dislocation substructure assisted by the formation of very fine deformation twins. The high initial ductility of these materials accommodates the loss in formability due the pre-

straining that offers good retained formability [52]. However the degree of pre-straining needs to be adjusted with respect to the remained ductility. According to Bouaziz *et al.* [52] two main problems occur with this approach: the severe reduction of the strain hardening coefficient and the introduction of significant anisotropy in the mechanical properties. Both factors result from the strong reduction of formability, which is turned out to be problematic especially at cut edges. In order to improve the formability of pre-strained sheets without significantly reducing the yield strength intensive investigations of the annealing treatment was carried out [52][57]. In the process, subsequent recovery or partial recrystallization treatment can be used to tailor the mechanical properties. This method takes advantage of the thermal stability of the mechanical twins (**Figure 2.1-4b)**, induced during the pre-straining at RT [52]. Up to recrystallization start temperature the mechanical twins are stable. The effect of annealing temperature and cold rolling reduction is show in **Figure 2.1-4b**. After [56][52], with increase in the recovery annealing temperature the yield strength decreases and the total elongation is raised. The best yield strength to ductility relation was obtained using high cold rolling reductions (~80%) and annealing at the lower limit of partial recrystallization for Fe-31Mn-3Al-3Si [53]. However, the sensitivity of the mechanical properties to small variations in this temperature region is extremely high, which may cause difficulties in an industrial application [52].

2.2 Stacking fault energy of austenitic steels

The stacking fault energy (SFE) of austenitic high manganese steels represents one critical parameter to define the variations in the strain hardening behavior as function of the deformation mechanisms like strain-induced martensite formation (Transformation Induced Plasticity TRIP), deformation twinning (twinning induced plasticity, TWIP) and pure dislocation glide (DG) [19]. In **Figure 2.2-1a** the SFE mechanism map for the Fe-Mn-C system is shown, presenting the variation in the SFE with respect to the chemical composition and the existence range of TRIP and TWIP mechanism [19][58]. Above the TRIP/TWIP transition line the activation of deformation twinning defines the variations and levels of work-hardening rate diagrams (**Figure 2.2-1b**, IV+V).
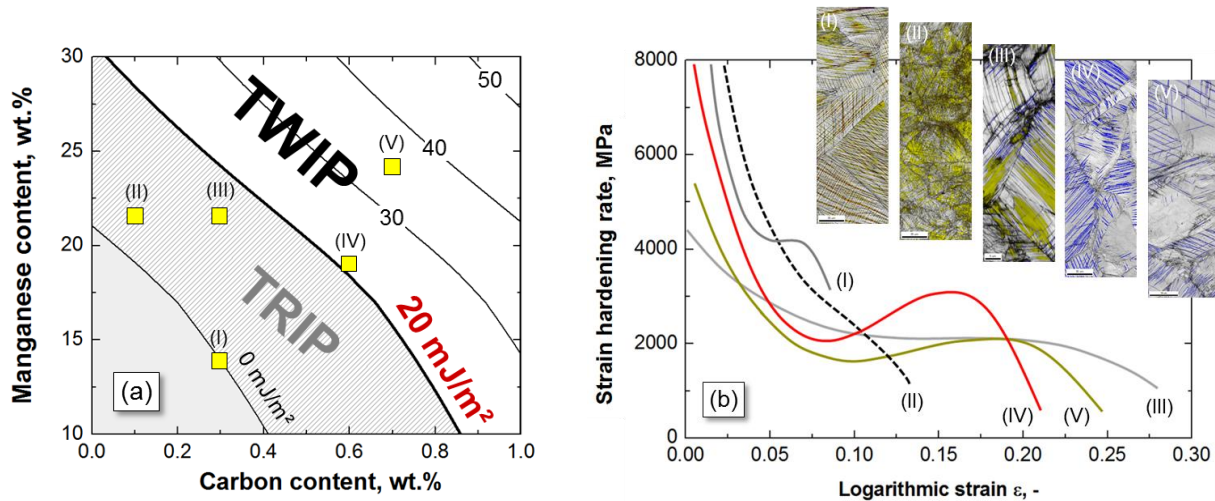

Figure 2.2-1 Calculated SFE for various Fe-Mn-C alloys (a) and
the respective deformation microstructure and strain hardening behavior (b).

In this range of SFE, lower SFE values result in the formation of finer twins, progressive decrease in the mean free path of dislocations by continuation of the plastic deformation referred to as dynamic Hall-Petch effect, and cutting of dislocation substructures by twin boundaries [59]. While in the SFE range below the TRIP/TWIP transition line the deformation induced martensitic transformation is possible, resulting in a markedly high strain hardening rate at low strains but sudden drop of work-hardening rate until fracture (**Figure 2.2-1b**, I-III). The effect of nitrogen on SFE in in austenitic stainless steels has been extensively discussed in the literature. However the reported trends of the SFE over nitrogen content differ with respect to the investigated alloying system or the respective domains of nitrogen contents that are analyzed (**Figure 2.2-2**). The SFE has been determined to increase with nitrogen content in Fe-Cr-Mn [60][61], Fe-(Mn)-N [62], Fe-Mn-Si-Al [63] and Fe-Cr-Mn-0.25C [64][65] steels. While a decrease of SFE over nitrogen content was referred in Fe-Cr-Ni-Mo [66], Fe-Cr-Mn [67], Fe-Cr-Ni [67][68], Fe-Cr-Ni-Mn [69] and Fe-Mn-N [162] alloys. According to the studies by [20][21][23][71][72], a non-monotonous behavior of SFE as function of nitrogen content was described for various Fe-Cr-(Ni)-Mn steels and Fe-Cr-Mn-C alloys with increasing carbon content up to 0.4 wt.% [60][73][76].
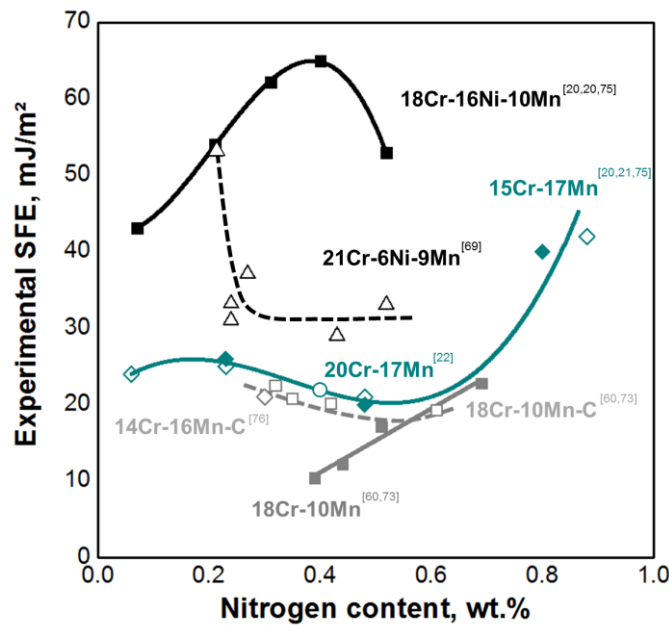
Figure 2.2-2 Experimentally measured SFE values over nitrogen content for different Fe-Cr-Ni-Mn, Fe-Cr-Mn and Fe-Cr-Mn-C alloys.

Due to the inconsistent experimental results, no general accepted method exists for the SFE calculation in the Fe-Cr-Mn-N system that can be applied to a wide range of chemical compositions. Various assumptions on the effect of nitrogen on SFE are discussed in the literature. Proposed by Suzuki [74], the interaction between solute atoms and the faulted area of extended dislocations is dominant in dilute solutions. The Suzuki segregation leads to an increased solute concentration at the stacking fault with respect to the matrix that hinders the dissociation of the stacking fault and the dislocation motions. In concentrated solutions, the Fisher effect associated with the existence of local ordering, is the dominant strengthening mechanism [75]. According to Flinn [75], the Fisher interaction is more important than the Suzuki effect in contribution to the strength of solid solutions.

Recently, the impact of nanodiffusion on the SFE in Fe-Mn-C alloys was analyzed combining *ab initio* calculations with *in situ* transmission electron microscopy analysis. It has been shown, that the measured SFE by TEM is strongly dependent on the applied experimental conditions [26]. The temperature induced outward diffusion (depletion) of carbon from the SFs during measurement is discussed to cause a change in SFE, compared to calculated values. Differences between experimental and theoretical SFE may be attribute to a change in the interfacial energy with the depletion of carbon and the local variation of the chemical composition that is not yet described and implemented in a SFE model. In order to estimate the SFE in austenitic stainless steels with different chemical compositions, various methods using quantum mechanical first-principle approaches [62][77][78], computational thermodynamics assessments [20][23][79][80][81] and experimental analysis have been investigated [82][83][84][85]. In the following, these methods will be discussed in more detail for the determination of SFE in nitrogen alloyed austenitic stainless steels.

2.2.1 *Ab-initio* calculations of SFE

The effect of interstitial nitrogen content on stacking faults in *fcc* Fe-N alloys has been studied by Kibey *et al.* [62][86] using first-principles, density functional theory (DFT) to calculate generalized stacking fault energies. The generalized stacking fault energies data served as input to the continuum Peierls-Nabarro model, which can be utilized to determine several useful macro-parameters [62]. It is reported, that nitrogen stabilizes the *fcc* phase relative to *hcp* phase; addition of nitrogen makes the *fcc* stacking energetically more favorable relative to *hcp* stacking. The stacking fault width and the critical shear stress for the onset of cross-slip of screw dislocations was found to depend non-monotonically on the nitrogen content [86], which is in agreement with experiment [20][72]. However, within this study only pure *fcc* metals have been investigated. Further work needs to be addressed to the effect of solute addition on the generalized stacking fault energies for ternary and more complex, multi-component alloys [62].

2.2.2 Experimental determination of SFE

The most established experimental methods for SFE determination uses transmission electron microscopy (TEM) for the direct observation of specific dislocation configurations, such as extended three-fold nodes [87][72] and Shockley partial dislocation pairs [85], shown in **Figure 2.2-3**. The node is generated by three separate partial dislocations that bound the stacking fault. Using the three-fold node method, the SFE can be calculated from the size of the extended three-fold node in equilibrium after Eq.(2.2) [88] or Eq.(2.3) [89]:

$$SFE = \frac{\mu b_p^2}{2R_o} \tag{2.2}$$

$$SFE = 0.26 \frac{\mu b_p^2}{R_i} \tag{2.3}$$

where μ is the shear modulus, b_p is the Burgers vector of a partial dislocation, R_o and R_i are the outer and inner radius of the node curvature, respectively. The weak-beam bright-field (WBBF) method provides a more precise determination of the dislocation three-fold node sizes then the conventional bright-field method [20]. According to Pierce [90], the apparent SFE measured from nodes in deformed samples is likely to be lower than the true value due to solute impedance forces.
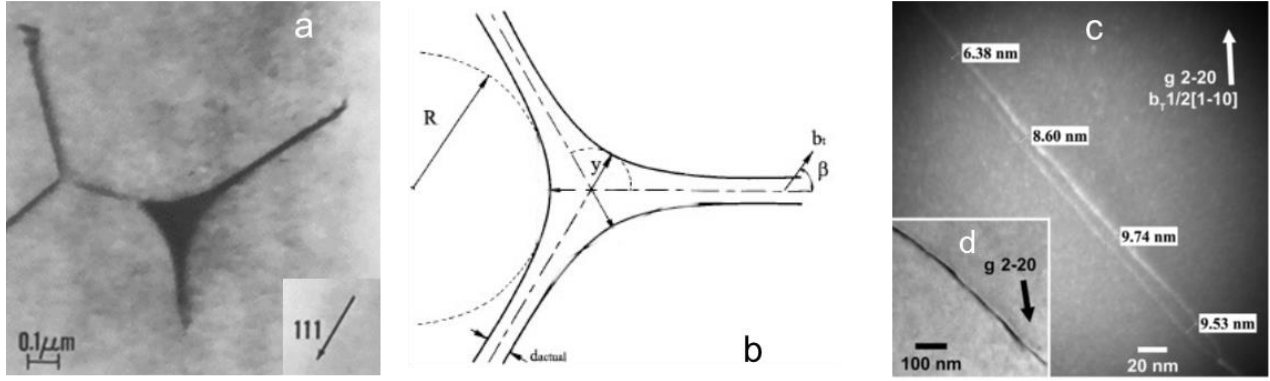
Figure 2.2-3 Extended dislocation node pair (a) [89], schematic of the three-fold node (b) [90], weak-beam dark-field (c) and bright-field image (d) of a partial dislocation pair [85].

In comparison to SFE measurements from Shockley partial dislocation pairs, measurements from extended dislocation nodes are usually higher and result in greater uncertainty [85]. Based on the isotropic elasticity theory, the classical equation that relates the SFE and partial dislocation separation after [91] can be written as:

$$\text{SFE} = \frac{\mu b_p^2}{8\pi d_{actual}} \frac{2-\upsilon}{1-\upsilon}\left(1 - \frac{2\upsilon\cos2\beta}{2-\upsilon}\right) \tag{2.4}$$

where υ is the Poisson's ratio, d_{actual} is the actual partial dislocation separation and β is the total dislocation character angle. For materials that show significant elastic anisotropy, the validity of Eq.(2.4) is restricted [90]. To resolve the individual partial dislocations, weak-beam dark-field (WBDF) TEM imaging is necessary. The WBDF image of a partial dislocation pair is shown in **Figure 2.2-3c** taken from Pierce *et al.* [85]. In comparison the bright-field image of same dislocation in **Figure 2.2-3d** illustrates the increased resolution of the WBDF technique. For low-SFE material the partial dislocation separations was found to display greater variations and susceptibility to image forces [90]. Fluctuates in the foil surfaces further influences the width of the partials. The sample preparation is of main importance to obtain reliable results.

Using diffraction methods, like X-ray or neutron diffraction, the SFE is indirectly determined by the stacking fault probability as function of dislocation density obtained from line profiles and peak shifts [92][93][94]. The SFE measurement by X-ray diffraction requires a knowledge of the dislocation configuration, in terms of barriers and pile-ups of extended dislocations [92]. The uncertainty of this method is closely correlated to the information about the dislocation substructure evolution that is related to various factors [92], like local ordering and atomic interactions in Fe-Cr-Mn-N steels [66][217]. The statistical error of the SFE determination by X-ray diffraction is reduced in comparison to TEM methods, as a relatively large volume can be measured. However, the X-ray signals are restricted to the surface area of the sample, consequently the structural parameters obtained are dependent on the surface condition of sample [60]. In-situ neutron diffraction is another potential method to obtain the SFE for different conditions. Until now, limitations arise from the available methods to analyses the neutron diffraction profile and from the accessibility of the Synchrotron measurement times [60].

2.2.3 Thermodynamics based methods for SFE calculation

The *ab initio* calculation of SFE for systems other than binary alloys is attended by enormous computing time. The boundary conditions for including interstitial elements in higher ordered systems are difficult to define with respect to e.g. the element distribution, the atomic interactions or the magnetic contributions, especially for temperatures above 0K. The experimental determination of the SFE by TEM requires long time experience and high preparation effort in order to obtain statistical and reproducible analysis. For the materials design, the application of thermodynamic based models is the most reasonable method to calculate the SFE for a wide range of chemical composition. For thermodynamic modeling of the SFE, the stacking fault can either be treated as an interface or as a second phase [81]. In the first case, the formation of a stacking fault is described as the change in the stacking sequence of a crystal by shear displacement, producing an interface that is separating the matrix. After Ferreira and Müllner [81], this interface exhibits a different chemical bonding than the matrix and can be treated as a specific case of a Gibbs interface:

$$\Delta G_{surf} = A\gamma^{\infty} \tag{2.5}$$

where A is the interfacial area and γ^{∞} is the interfacial energy per unit area of the interface. Based on the volume approach the stacking fault is treated as separate phase with different stacking, confined from the matrix by two interphase boundaries that exist parallel to the faulted planes [81]. These interphase boundaries are further represented by partial dislocations that confine the stacking fault. If a stacking fault is introduced to the perfect crystal, the variation in the stacking sequence causes a change in the Gibbs free energy of the system and can be expressed by:

$$\Delta G_{vol} = V^{SFP}\left(G_V^{SFP} - G_V^M\right) + 2A\sigma \tag{2.6}$$

where V^{SFP} is the volume of the stacking fault phase (SFP), G_V^{SFP} and G_V^M are the Gibbs free energies per unit volume of SFP and matrix, respectively, and σ is the interfacial energy per unit area of the interface boundary. If the stacking fault is assumed as a second phase embryo, the stacking fault energy comprises both volume and surface energy contribution [95]. With it, the difference in Gibbs free energy of the system in equilibrium is assumed to be the same for both cases. Thus, the following equations can be written:

$$\Delta G_{surf} \equiv \Delta G_{Vol} \tag{2.7}$$

$$\frac{\delta\Delta G_{surf}}{\delta A} = \frac{\delta\Delta G_{Vol}}{\delta A} \tag{2.8}$$

The ideal stacking fault energy, given as energy per unit area, arises from Eq.(2.8) as follows:

$$SFE_{ideal} = \gamma^{\infty} = 2s\left(G_V^{SFP} - G_V^M\right) + 2\sigma \tag{2.9}$$

The interplanar spacing, s, represents the spacing between the SFP structure and the matrix. A difference in the layer spacing between the SFP and matrix results in an elastic strain field that needs to be taken into account. Eq. (2.9) is then modified by the coherent strain energy, E_{strain}. The resultant effective stacking fault energy is expressed as:

$$SFE_{effective} = 2s\left(G_V^{SFP \to M} + E_{strain}\right) + 2\sigma \tag{2.10}$$

In general, the ideal SFE is treated as intrinsic material property corresponding to an infinite stacking fault, while the effective SFE accounts for a non-intrinsic material property including a strain energy term in addition to the ideal SFE, associated with infinite and terminated stacking faults, respectively [81]. In a particular case, the stacking fault is bounded by two partial dislocations and E_{strain} can be calculated by:

$$E_{strain} = \frac{\pi D \varepsilon_s^2}{2} = \frac{\mu \varepsilon_s^2}{4(1-\nu)} \qquad (2.11)$$

where μ is the shear modulus, ν is Poisson's ratio and ε_s is the strain normal to the fault plane. The strain energy contribution is considered as the sum of a dilatational and shear contribution [95] and is weakly dependent upon composition [96]. After Olsen and Cohen [95], the structure of a conventional stacking fault in the *fcc* lattice can be identified by the following role: the intrinsic fault is formed by the motion of a single Shockley partial dislocation on a closed packed plane, while the motion of such a dislocation on every second plane produces a bulk *hcp* embryo, with two planes in thickness, referred as intrinsic stacking fault. In consistency with classical nucleation theory, the free energy of the *hcp* embryo relative to the perfect *fcc* lattice can be expressed in terms of the free energy difference between the two phases ($\Delta G^{\gamma \to \varepsilon}$), the strain energy ($E_{strain}$) and a true surface energy (σ). With respect to Eq. (2.10), the stacking fault energy can be written as:

$$SFE = 2\rho_A(\Delta G^{\gamma \to \varepsilon} + E_{strain}) + 2\sigma \qquad (2.12)$$

where ρ_A is the density of atoms in a closed packed plane in moles per unit area. Thermodynamic parameters for the *hcp* and *fcc* phase in the Fe-Mn [97][98] and Fe-Cr-Ni [81][99] system are well assessed. However, the availably thermodynamic data, used in the most latest works by Curtze *et al.* [100] and Roncery *et al.* [7][101] for the Fe-Cr-Ni-(N) and Fe-Cr-Mn-CN systems, respectively, show major discrepancies with the experimental results especially with higher nitrogen contents. One main reason can be addressed to the thermodynamic model and the interaction parameter used to calculate the $\Delta G^{\gamma \to \varepsilon}$. The subregular model, applied by [7][100], only considers substitutional solid solution and therefore underestimates the effect of interstitial nitrogen on the *fcc* phase stability [58]. While in the study by [100], only first order interaction energies between interstitial and substitutional atoms were considered, which is not suitable to describe higher ordered systems [102]. Presented by [98], *ab initio* calculations can be used to critically assess literature data, for instance the enthalpies of formation, to improve the thermodynamic description of a system. In order to develop a SFE model that includes the effect of nitrogen in higher ordered systems, a reevaluation of the thermodynamic parameter for Fe-Cr-Mn-N alloys is required and presented in this work.

3   Methods of investigation

In the current chapter the employed theoretical and experimental methods used in the presented work are described. Based on the nitrogen solubility calculations and determination of phase diagrams, balanced chemical compositions were defined as pilot and industry strip-cast alloys (Chapter 4.2.3). The mechanical properties and flow behavior of the designed materials were characterized by tensile testing at various temperatures and applied strain. Microstructure investigations of the as-received and deformed microstructures were performed by optical microscopy (LOM), X-ray diffraction, electron probe microanalysis (EPMA) and electron back-scatter diffraction (EBSD). The deformation substructure was characterized in order to define the active deformation mechanism, correlated to the determined SFE.

3.1   Modelling approach

3.1.1   Stacking fault energy

3.1.1.1   Calculation of $\Delta G^{\gamma \to \varepsilon}$ – Thermodynamic two-sublattice model

Introduced by Hillert and Staffansson [103], in the thermodynamic two-sublattice model the observed *fcc* and *hcp* phases are treated as interstitial solid solutions of nitrogen in the γ-Fe and ε-Fe, respectively. The effective Gibbs free energy of the $\gamma \to \varepsilon$ phase transformation, $\Delta G^{\gamma \to \varepsilon}$, indicating the relative stability of the fcc phase, is calculated accounting the Gibbs free energy of the *fcc* and *hcp* phases, G^{γ} and G^{ε} as follows:

$$\Delta G^{\gamma \to \varepsilon} = G^{\varepsilon} \; - \; G^{\gamma} \tag{3.1}$$

In the evaluation of Cr-N, Mn-N and Fe-N binary systems, the M_2N phase is regarded as a nitrogen-rich solution within the hexagonal M (M = Fe, Cr, Mn). Therefore, the interstitial solution of nitrogen in the *hcp* phase of a metal can be described by the same thermodynamic parameters as the M_2N nitride. For the Fe-Cr-Mn-N system, the M_2N phase is approximated in the form of $(Cr,Fe,Mn)_1(N,Va)_{0.5}$ with the site occupancy of 1:0.5, where it is assumed that the interstitial sites are never simultaneously occupied [104]. The parameter $Cr_1Va_{0.5}$, $Fe_1Va_{0.5}$ and $Mn_1Va_{0.5}$ represent pure chromium, iron and manganese in the *hcp* state with vacancies (Va), respectively [105]. In the *fcc* phase, $(Cr,Fe,Mn)_1(N,Va)_1$, the number of sites in each sublattice is equal to one. The Gibbs free energy of every phase, G^{Φ}, with site numbers in each sublattice of a=c=1 for *fcc* and a=1, c=0.5 for *hcp*, can then be calculated:

$$G^{\Phi} = G^{\Phi}_{chem} + G^{\Phi}_{excess} + G^{\Phi}_{magn} \tag{3.2}$$

where

$$G^{\Phi}_{chem} = \sum_i y_i \left(y_{Va} {}^{\circ}G^{\Phi}_{i:Va} + y_N {}^{\circ}G^{\Phi}_{i:N} \right) + \left[aRT \sum_i y_i \ln y_i + cRT \left(y_N \ln y_N + y_{Va} \ln y_{Va} \right) \right] \tag{3.3}$$

with i,j = Fe, Mn, Cr. The first term of the chemical Gibbs energy, G^{Φ}_{chem}, refers to the ideal reference state of a solution that defines the Gibbs energy of interactions between neighboring atoms of elements in different sublattices [98], while the second term is the ideal entropy of mixing. The Gibbs free energies, ${}^{\circ}G^{\Phi}_{i:N}$, were taken from the evaluations of the binary systems Cr-N [106], Fe-N [106] and Mn-N [103] representing the state of energy in which all interstitial sites are filled with

nitrogen. The parameters $°G^\Phi_{i:Va}$ represent the Gibbs free energy of the pure elements in a hypothetical nonmagnetic state. These values were taken from the Scientific Group Thermodata Europe (SGTE) database for pure elements after Dinsdale [107]. The variables $y_{i,j}$ are the site fractions of the component i,j in the equal sublattice. For the substitutional sublattice,

$$y_{i,j} = \frac{x_{i,j}}{(1-x_N)} \tag{3.4}$$

and for nitrogen the interstitial sublattice with vacancies,

$$y_N = \frac{x_N}{c(1-x_N)} \tag{3.5}$$

where x denotes the mole fraction of each element in the system. The site fractions are correlated in the following relations:

$$y_{Fe} + y_{Mn} + y_{Cr} = 1 \tag{3.6}$$

$$y_N + y_{Va} = 1 \tag{3.7}$$

The excess term G^Φ_{excess} represents the contribution to the Gibbs free energy as the sum of all possible interactions within the system in one sub-lattice and between the two sub-lattices, which is expressed as:

$$\begin{aligned}
G^\Phi_{exess} = {} & y_N y_{va} \sum_{i=1} y_i L^\Phi_{i:N;va} + y_N y_{va} \sum_{i=1} \sum_{j=i+1} y_i y_j L^\Phi_{i;j:N;va} \\
& + \sum_{i=1} \sum_{j=i+1} y_i y_j \left(y_N L^\Phi_{i;j:N} + y_{va} L^\Phi_{i;j:va} \right) \\
& + y_{Cr} y_{Fe} y_{Mn} \left(y_N L^\Phi_{Cr;Fe;Mn:N} + y_{va} L^\Phi_{Cr;Fe;Mn:va} \right)
\end{aligned} \tag{3.8}$$

where the subscript comma in the interaction parameter, $L^\Phi_{i;j:N,Va}$, separates the elements that interact in the same sublattice and the colon separates those in different sublattices. $L^\Phi_{i;j:N:Va}$ exists only for the Fe-Cr-N *fcc* phase [106]. According to the Redlich-Kister [108] power series each binary or ternary parameter can vary with composition and temperature. The contribution to the Gibbs free energy due to magnetic ordering, G^Φ_{magn}, is given by the following expression:

$$G^\Phi_{magn} = RT \ln(\beta^\Phi + 1) f^\Phi(\tau) \tag{3.9}$$

where β^Φ is a composition-dependent parameter related to the total magnetic entropy, Eq. (3.10).

$$\beta^\Phi = \sum_i y_i y_{va} \beta^\Phi_{i:va} \tag{3.10}$$

The function $f^\Phi(\tau)$ represents the polynomial proposed by Hillert and Jarl [109] formulated as a Taylor expansion of the formalism after Inden [110] restricted to the third term, Eq. (3.11). The variable τ is defined as T / T^Φ_{Neel}, where T^Φ_{Neel} is the critical temperature for the change from (*fcc*) paramagnetic to (*hcp*) anti-ferromagnetic ordering. It was assumed that nitrogen had no effect on the magnetic term of the Gibbs free energy of the *fcc* and *hcp* phase [23][111][112].

$$\tau < 1 \quad f^{\Phi}(\tau) = 1 - \frac{1}{A}\left[\frac{79\tau^{-1}}{140p} + \frac{159}{497}\left(\frac{1}{p}-1\right)\left(\frac{\tau^3}{2}+\frac{\tau^9}{45}+\frac{\tau^{15}}{200}\right)\right] \tag{3.11a}$$

$$\tau > 1 \quad f^{\Phi}(\tau) = -\frac{1}{A}\left[\frac{\tau^{-5}}{10} + \frac{\tau^{-15}}{315} + \frac{\tau^{-25}}{1500}\right] \tag{3.11b}$$

The constant factor $A = \frac{518}{1125} + \frac{11692}{15975}\left(\frac{1}{p}-1\right)$ with p=0.28 are set to be equal for the *fcc* and *hcp* phases. According to Qui [106], negative values of T^{Φ}_{Neel} and β^{Φ} used to characterize the properties of an anti-ferromagnetic phase, therefore divided by -3 for *fcc* and *bcc* phases.

3.1.1.2 Calculation of SFE

In this work, the approach proposed by Olsen and Cohen [95], to calculate an ideal SFE was used, that defines the required Gibbs free energy to form an intrinsic stacking fault by the movement of a single Shockley partial dislocation on a closed packed plane. Since the motion of the partial dislocation occurs on every second plane, a hexagonal closed packed (*hcp*) crystalline structure is formed with a thickness of n atomic layers. According to Adler *et al.* [113] the core equation to calculate the SFE [mJ/mol] is:

$$SFE = n\rho \, \Delta G^{\gamma \to \varepsilon} + n\sigma^{\gamma/\varepsilon} \tag{3.12}$$

Where n, the number of planes, was set equal to 2, ρ is the molar surface density along {111} planes, $\Delta G^{\gamma \to \varepsilon}$ is the change of the molar Gibbs free energy due to the phase transformation of face cubic centered (*fcc*) austenite (γ) to *hcp*-ε-martensite and $\sigma^{\gamma/\varepsilon}$ defines the interfacial energy of the γ/ε-interface that can vary within different alloying systems [114][115]. The correlation between SFE and $\Delta G^{\gamma \to \varepsilon}$ according to Eq. (3.12) is shown in **Fig. 3.1-1**.

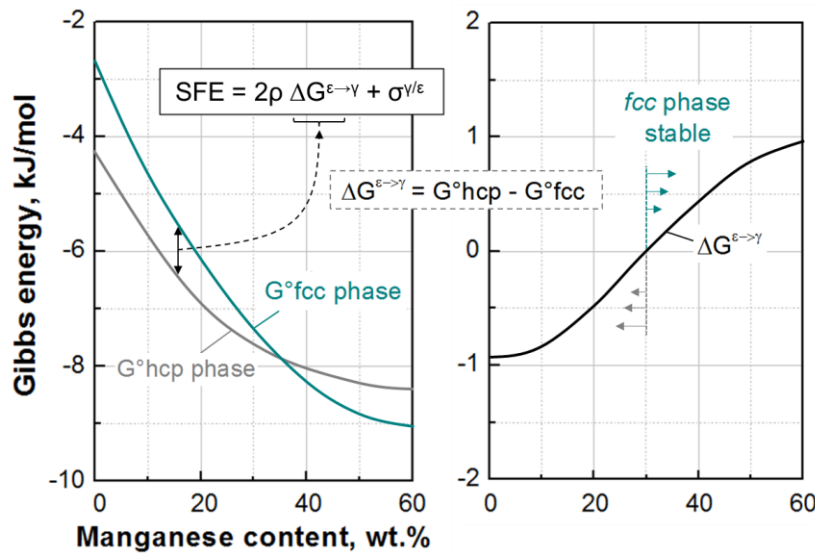**Fig. 3.1-1** Thermodynamic description of SFE by calculating the Gibbs free energy change $\Delta G^{\gamma \to \varepsilon}$ for the $\gamma(fcc) \to \varepsilon(hcp)$ phase transformation.

3.1.2 Phase diagram

The phase diagram calculations were carried out using the Thermo-Calc TCC software version S. The database TCFE 6 was chosen for all calculations, where iron was considered as main constitution of the alloy and chromium, manganese, nickel, carbon and nitrogen as main alloying elements. The gas phase and *fcc*, *bcc*, liquid, *hcp*, graphite, cementite, m23, and m7 phases were accounted for the analysis. The following reference states have been set: nitrogen (gas), iron and chromium (*bcc*), manganese (*fcc*), and carbon (graphite). Phase diagrams were plotted as function of temperature over nitrogen content for varying Mn, Cr content and Ni, C set constant to 0.5 wt.% and 0.1 wt.%, respectively.

3.1.3 Nitrogen solubility

The dissolution of nitrogen from the atmospheric gas phase in the liquid/solid metal occurs due to the splitting of the nitrogen molecules into atoms, by the following reaction:

$$\frac{1}{2}\{N_2\} = [N] \tag{3.13}$$

Assuming equilibrium between the nitrogen solubility in the metal and the gaseous phase of standard chemical potential, the equilibrium constant K_N for a given temperature can be expressed as ratio of the chemical activity a_N of nitrogen in solution and the partial pressure of nitrogen p_{N_2} in the surrounding gas atmosphere as:

$$K_N = \frac{a_N}{\sqrt{p_{N_2}}} = \frac{[\%N] \cdot f_N}{\sqrt{p_{N_2}}} \tag{3.14}$$

The activity coefficient f_N correlates the effect of alloying elements on the chemical activity of dissolved nitrogen to its concentration [%N] in wt.%. Implying the validity of Sieverts' law, f_N reaches unit. By adding an alloying element X (with X = Cr, Mn, Ni, C in this work) the concentration of dissolved nitrogen is changed. The activity coefficient for the Fe-N-X solution is then expressed by a Taylor series expansion of first and second order interaction parameters $e_N^{(X)}$ and $r_N^{(X)}$ of the alloying element X with the concentration [%X] in wt.%, respectively. Including the interaction of nitrogen with itself $e_N^{(N)}$, the logarithm of the activity coefficient is given as:

$$\log f_N = \log f_N^{(X)} + \log f_N^{(N)} \tag{3.15}$$

resulting in the following definition of

$$\log f_N^{(X)} = \sum_{X=1} e_N^{(X)} \cdot [\%X] + r_N^{(X)} \cdot [\%X]^2 \tag{3.16}$$

$$\log f_N^{(N)} = e_N^{(N)} \cdot [\%N] + r_N^{(N)} \cdot [\%N]^2 + \sum_{X=1} r_N^{(N,X)} \cdot [\%N][\%X]. \tag{3.17}$$

According to Svyazhin *et al.* [116] the parameter of 2nd order $r_N^{(N)}$ in Eq. (3.17) can be neglected, as $(\log f_N)_{[\%N] \to 0}$ is close to zero at the polynomial degree n=1, accounted for dilute solutions. Adjusting Eq. (3.13) by using the description of f_N from Eq. (3.15) the solubility of nitrogen at constant temperature and concentration of component X for Fe-N-X, can be calculated as:

$$\log \frac{[\%N]}{\sqrt{p_{N_2}}} = \log K_{N(Fe)} - \log f_N.$$

(3.18)

To calculate the nitrogen solubility for temperatures other than 1600°C, a temperature correction term as introduced by Schürmann and Kunze [117] was used:

$$\log f_N^{(T)} = \left(-0.75 + \frac{3280}{T}\right) \log f_N.$$

(3.19)

The model was evaluated by using different sets of interaction parameters proposed by several authors within the Fe-Mn-N and Fe-Cr-Mn-N alloying systems.

3.2   Materials processing

3.2.1   Laboratory processing

The Fe-Cr-Mn-N pilot alloys were produced as lab-scale strip-cast material on a vertical twin-roll caster, without additional inline hot-rolling step, at the Metal Forming Institute (IBF) of the RWTH Aachen University. The melting temperature T_{melt} and the casting temperature T_{cast} (melting pool) were set to 200 K > T_{liqu} (~1550±50°C) and 30-50 K > T_{liqu} (~1450±20°C), respectively. The nominal compositions of the melt and the as-cast strip material are listed in Tab. 4.2-3. Strips with a thickness of 1.6 mm and width of 150 mm have been produced as coils of ~20-25 m in length from a melt weight of ~180 kg.

The as-cast strip material of the pilot alloys was further cold-rolled to a final thickness of 0.6 mm and recrystallization heat treated as listed in in Tab. 4.2-3. The annealing time was set to increase with alloying content, with respect to the slower recrystallization kinetics; investigated in test runs. After machining the tensile samples from the sheet material (Chapter 3.3), the samples were recrystallized in a conventional lab-scale muffle furnace (Nabertherm N 41/H), wrapped in annealing foil to protect the surface from oxidation, afterwards quenched in water.

3.2.2   Industrial processing

The industrial strip-cast alloy (IC) was produced on the strip-cast line, vertical twin-roll caster, with inline hot-rolling step (25% hot rolled), at the Outokumpu Nirosta stainless steel plant in Krefeld, Germany. The melting process was performed within an induction furnace, separately of the strip-cast line. The melt was transported in a ladle to the double roller casting unit; without atmospheric control. The strip with a thickness of 1.7 mm and width of 1.100 mm has been produced as coil of ~25t in weight. The nominal composition of the as-cast strip material is listed in Tab. 4.2-4.

The as-cast hot-rolled strip was further cold-rolled to a final thickness of 1 mm and recrystallization heat treated in a continuous annealing line at Outokumpu Nirosta stainless steel plant in Krefeld, Germany, at 1150°C for 2-5 min followed by air cooling.

3.3 Mechanical testing

Tensile Specimens of the sheet material were machined in rolling direction according to DIN 50124 with a gage length of 50 mm (A_{50}) and 30 mm (A_{30}). Uniaxial tensile tests were performed after DIN EN 10002-1 with applied engineering strain rate of 10^{-3} s^{-1} using a Zwick 1484 tensile machine (Zwick Reoll GmbH). The true stress-strain rates were determined over the crosshead speed as change of displacement per time interval. Interrupted tensile tests at room temperature were carried out at logarithmic strains of 0.04, 0.14, 0.21, 0.31 and until fracture using A_{50} samples. Tensile tests at different temperatures were performed in a climate chamber in the temperature range from -150°C up to 250°C. For the temperature measurements a thermal element was applied directly on the specimen surface. A_{30} samples have been used to better control the homogenous temperature distribution in the samples. The accuracy of the temperature control was ±2 °C.

3.4 Microstructure analysis

3.4.1 Light optical microscopy

All specimens ware wet-grinded using SiC-paper and polished with diamond paste. The samples were finally electrochemical polished with electrolyte A2 from Struers GmbH. Microstructure etching was carried out at RT using Lichtenegger and Bloech color etching solution (H_2O, $(NH_4)HF$, $K_2S_2O_5$). The deformed microstructure analysis was performed at fracture site of the tensile samples in cross-section.

3.4.2 Scanning electron microscopy

Field emission scanning electron microscopy (FESEM) was carried out using the Σigma FESEM (Carl Zeiss Microscopy GmbH) operating at 10 kV and with a working distance of 9.3 mm. Secondary electron contrast was used to analyze the deformation microstructure. EDX analysis was performed with a Silicon Drift Detector (SDD) - X-Max^{50} (OXFORD Instruments GmbH).

3.4.3 X-ray diffraction

X-ray diffraction analysis was carried out using the Cu K radiation in a diffractometer (Philips-PW1380) with a monochromator at the Institute of Physical Metallurgy and Metal Physics, Aachen. The phase fraction analysis was performed on as-received as-cast and deformed cold-rolled/RX samples, in order to determine the existence of *bcc* delta-ferrite and deformation induced *bct* and/or *hcp* martensite.

3.4.4 Electron probe microanalysis

The microstructure segregation characterization was performed by using electron probe microanalysis (EPMA). Cross-sections of the polished samples were analyzed in an electron microprobe (CAMEBAX SX 50) operating at 15 kV and 80-100 nA at the Central Facility for Electron Microscopy, Aachen. For micro-segregation analysis of the as-cast strip material the local chemical composition was detected using elemental mappings in accordance to Daamen *et al.* [36]. The scanned area was set to 530 x 530 µm² with a step size of 2 µm. The measured X-ray intensities of the measured elements Fe, Cr, Mn and N were calibrated for quantitative information using bulk standards or standards of known chemical composition.

3.4.5 Electron back-scatter diffraction

The electron back-scatter diffraction (EBSD) measurements were performed using a JEOL JSM 7000F FEG-SEM with an EDAX-TSL Hikari camera and OIM DataCollection 6.2/OIM Analysis 6.2 software. The step size was adjusted to 0,5 µm for an area of 500x500 µm. The criterion for the definition of twin boundaries was 60° misorientation about the <111> axis, with an angular tolerance of 5° within the γ(*fcc*)-matrix. Specimens ware wet-grinded using SiC-paper, mechanically polished with diamond paste and electrochemical polished with electrolyte A2 from Struers GmbH. The microstructure analysis of the samples was performed in longitudinal-section. The vertical axis in the datasets/images was assigned as tensile axis (TA). In this work, the EBSD data are represented as image quality (IQ) maps, inverse pole figure (IPF) maps and kernel average misorientation (KAM) maps (examples presented in Fig. 3.4-1).
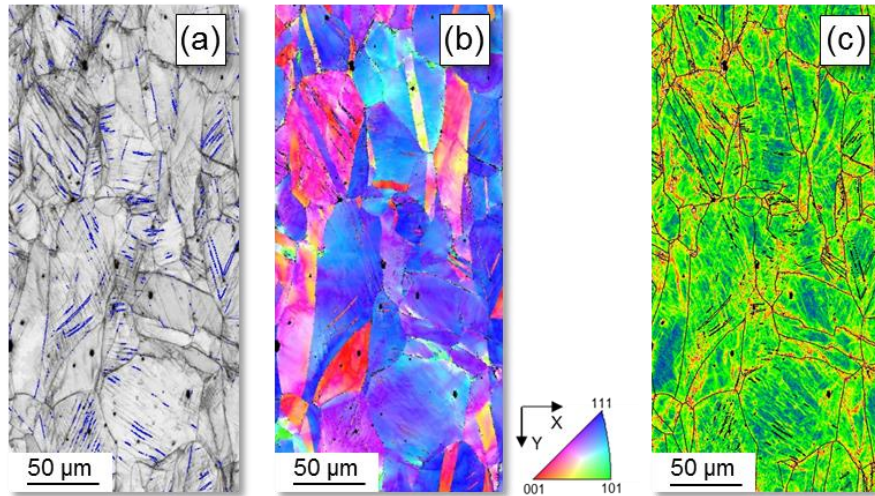

Fig. 3.4-1 EBSD analysis of the deformation microstructure of the alloy Fe-13Cr-22Mn-0.44N shown as: (a) image quality (IQ) map of the *fcc* phase with blue-colored marks indicate Σ3 twin boundaries, (b) inverse pole figure (IPF) map and (c) kernel average misorientation (KAM).

In an EBSD map scan the beam is guided across the sample surface in a defined regular grid. At each point the electron backscatter pattern is captured, the diffraction bands are detected and automatically indexed with the corresponding crystallographic orientation. With the given analysis about the phase and orientation at each point in the map, the EBSD data provides information about character, exact location and distribution of grain boundaries (IQ map), quantity and distribution of grains in specific orientations (IPF maps) and state of elastic strain and/or local variations in residual strain (KAM map). The IPF orientation component uses a basic RGB coloring scheme that is fitted to an inverse pole figure. The colors red, green, and blue are assigned to grains whose <001>, <101> or <111> axes, respectively, are parallel to the projection direction of the inverse pole figure. Intermediate orientations are colored by an RGB mixture of the primary components.

4 Results

4.1 Thermodynamics based modeling of SFE

4.1.1 Literature data for model validation

The thermodynamic model for calculation of $\Delta G^{\gamma\rightarrow\varepsilon}$ and SFE was validated by a number of available chemical compositions in the Fe-Cr-Mn-N system from literature with the given microstructures before and after deformation at room temperature and measured SFE values as shown in Tab. 4.1-1.

Tab. 4.1-1 Chemical composition and microstructure before/after deformation and experimental SFE values of austenitic stainless steels reported in the literature.

Reference		Chemical Composition, wt.%					Microstructure		SFE
Author	Year	Cr	Mn	Ni	N	C	*before deformation*	*after deformation*	mJ/m²
Remy and Pineau [118]	1977	4.8	29.6	-	-	0.02	γ	$\gamma + \varepsilon_D$	
		5.0	28.2	-	-	0.01	γ	$\gamma + \varepsilon_D$	
		5.1	31.3	-	-	0.01	γ	γ^T	
Lenel and Knott [119]	1987	11.8	10.4	-	0.19	-	γ	$\gamma + \alpha'_D$	
		13.4	10.2	-	0.23	-	γ	$\gamma + \alpha'_D$	
		12.6	9.5	-	0.32	-	γ	$\gamma + \alpha'_D$	
		12.7	9.1	-	0.22	-	γ	$\gamma + \alpha'_D$	
		12.1	8.3	-	0.16	-	γ	$\gamma + \alpha'_D$	
		11.8	8.3	-	0.18	-	γ	$\gamma + \alpha'_D$	
		11.8	8.1	-	0.21	-	γ	$\gamma + \alpha'_D$	
Nyilas and Obst [120]	1988	5.2	25.6	-	-	-	γ	γ	
		5.2	25.5	-	0.10	0.02	γ	γ	
		8.5	39.8	-	0.28	0.06	γ	γ	
		13.4	33.9	-	0.32	0.04	γ	γ	
Kitamura et al. [121]	1990	19.5	19.6	-	0.65	0.08	γ	γ	
		20.1	19.2	-	0.73	0.07	γ	γ	
Földéaki and Ledbetter [122]	1992	18.3	19.0	0.2	0.57	0.10	γ	γ	
		18.8	18.8	0.1	0.8	0.01	γ	γ	
		14.0	20.2	0.3	0.39	0.01	γ	γ	
Ilola et al. [67]	1996	22.2	12.3	0.4	0.97	0.02	γ	γ^T	
Uggowitzer et al. [123]	1996	18.2	19.0	1.2	0.61	0.08	γ	γ	
Vogt et al. [124]	1996	18.7	19.1	0.5	0.90	0.04	γ	γ	
Onozuka et al. [125]	1998	13.5	24.5	-	0.20	0.02	γ	γ	
Tomota et al. [126][127]	1998	17.2	18.8	0.2	0.51	0.07	γ	γ	
		19.1	19.4	0.4	0.84	0.05	γ	γ *(planar slip)*	
Mills and Knutsen [128]	1998	19.0	10.0	0.8	0.63	0.03	γ	γ	
Liu et al. [129][130]	1998/04	19.3	19.6	0.3	0.70	0.05	γ	γ	
Sorokina and Shlyamnev [131]	1999	14.0	14.0	-	-	-	$\gamma + \varepsilon + \alpha'$	$\gamma + \alpha'_D$	
		14.0	16.0	-	-	-	$\gamma + \varepsilon$	$\gamma + \alpha'_D$	
		14.0	18.0	-	-	-	$\gamma + \varepsilon$	$\gamma + \varepsilon_D + \alpha'_D$	
		14.0	22.0	-	-	-	γ	$\gamma + \varepsilon_D$	
Okada et al. [132]	2003	12.0	6.6	-	0.03	-	$\gamma + \varepsilon + \alpha' + \delta$	$\gamma + \varepsilon_D + \alpha'_D + \delta$	
		12.5	11.3	-	0.15	0.01	$\gamma + \varepsilon + \alpha'$	$\gamma + \varepsilon_D + \alpha'_D$	
		12.0	23.0	-	-	-	$\gamma + \varepsilon + \delta$	$\gamma + \varepsilon_D + \alpha'_D$	
		12.0	30.3	-	0.07	0.01	$\gamma + \varepsilon + \delta$	$\gamma + \varepsilon_D + \alpha'_D$	
Petrov [20][72]	2003/05	15.0	17.0	-	0.23	-	γ	γ	25
		15.0	17.0	-	0.48	-	γ	γ	21
Gavriljuk et al. [21]	2006	15.0	17.0	-	0.80	-	γ	γ	40
		15.0	17.0	-	0.88	-	γ	γ	42
Efros et al. [133]	2004	18.0	18.0	-	0.50	0.07	γ	γ	
		18.0	20.0	-	0.80	0.08	γ	γ *(planar slip)*	
Jandová et al. [22]	2004	19.8	17.4	0.1	0.40	0.06	γ	γ^T	23(±2)
Balitskii [134]	2004	18.3	19.1	-	0.62	0.05	γ	γ	
Saller et al. [61]	2006	14.0	20.0	1.0	0.30	<0.04	γ	γ^T	
		21.0	23.0	1.0	0.90	<0.04	γ	$\gamma^{(T)}$ *(planar slip)*	
Riedner et al. [135]	2008	21.0	23.1	1.5	0.88	0.04	γ	γ *(planar slip)*	

Lee et al. [60][136]	2008/10	18.0	9.7	-	0.33	0.03	γ	γ + ε_D + α'_D	
Kim et al. [137]	2009	17.8	9.7	-	0.39	0.03	γ	γ + ε_D + α'_D	10.4 (±0.4)
		18.1	9.7	-	0.44	0.03	γ	γ + ε_D + α'_D	12.2 (±0.4)
		17.7	9.6	-	0.51	0.03	γ	γ^T + ε_D + α'_D	17.1 (±0.3)
		18.6	10.0	2.1	0.53	0.02	γ	γ^T + ε_D + α'_D	
Hwang et al. [138]	2011	18.5	9.5	0.4	0.58	0.04	γ	γ^T (minor traces ε_D)	
Lee et al. [73]	2012	18.3	9.7	-	0.61	0.02	γ	γ^T (minor traces ε_D)	19.3 (±0.2)
Hwang et al. [139]	2011	17.5	9.8	-	0.69	0.03	γ	γ^T	22.8 (±0.5)
Mililitsky et al. [140]	2008	18.0	17.7	0.2	0.49	0.04	γ	γ^T	
Dai et al. [82]	2009	13.2	24.6	0.1	0.44	-	γ	γ^T	
Terazawa et al. [45]	2009	21.0	23.0	-	0.90	-	γ	γ (planar slip)	
Yang and Ren [141]	2010	17.9	15.3	<0.2	0.46	-	γ	γ	
		21.0	23.0	<0.3	0.97	-	γ	γ	
Xu et al. [142]	2011	18.7	12.5	-	0.55	0.05	γ	γ^T	
Choi et al. [143]	2011	20.3	5.0	0.2	0.10	0.02	γ + δ	γ + α'_D + δ	
		20.2	5.1	0.2	0.19	0.02	γ + δ	γ + α'_D + δ	
		20.1	5.0	0.2	0.28	0.02	γ + δ	γ + α'_D + δ	

(γ^T – mechanical twinning, ε^D and α^D – deformation induced hcp and bcc/bct martensite, δ – bcc ferrite)

4.1.2   Thermodynamic modeling of the Gibbs free energy change $\Delta G^{\gamma \rightarrow \varepsilon}$

4.1.2.1   Evaluation of the interaction parameter L^{Φ}

In order to calculate the Gibbs free energy change $\Delta G^{\gamma \rightarrow \varepsilon}$ for the high-manganese Fe-Cr-Mn-N system, the description of thermodynamic properties of manganese is of main importance. The interaction parameter of the *hcp* phase in the binary Fe-Mn system, $L^{(hcp)}_{Fe,Mn:Va}$, has been investigated in several studies with respect to the influence of the chemical composition as summarized in [144]. The calculated Gibbs free energy of the *fcc/hcp* phase and the resulting Gibbs free energy change $\Delta G^{\gamma \rightarrow \varepsilon}$ as function of manganese are shown in **Fig. 4.1-1** after (a,e) Huang [97], (b,f) Djurovic *et al*. [98], (c,g) Witusiewicz *et al.* [145] and (d,h) Nakano and Jacques [115]. The assessment of the Fe-Mn system by Huang [97] was based on the description of pure iron and manganese. The interaction parameter for the γ(*fcc*) phase, $L^{(fcc)}_{Fe,Mn:Va}$, was introduced to define the two δ/γ/liq equilibria; also predefined for the calculations after [98] and [145]. The thermodynamic description of the metastable ε(*hcp*) phase in the Fe-Mn system was adjusted by Huang [97] to assess higher ordered systems where the ε(*hcp*) phase is stable. Minor adjustment of the $L^{(hcp)}_{Fe,Mn:Va}$ parameter from [97] was proposed by Djurovic *et al*. [98] for the thermodynamic evaluation of the Fe-Mn-C system using the CALPHAD method, to better fit more recent data on the ε-martensite formation from Cotes *et al.* [96]. However, the model adjustment by [98] was mainly originated by improving the carbide equilibria for the formation of different metastable Fe_xC_y carbides, which is not directly applicable for the carbon-free Fe-Cr-Mn-N system. In comparison to [97] the slightly higher value of $^0L^{(hcp)}_{Fe,Mn:Va}$ from [98] results in a minor increased stability of the ε(*hcp*) phase with respect to the γ(*hcp*) phase (compare **Fig. 4.1-1a,b**). According to Djurovic *et al*. [98] the revision by [115] resulted in an improper Gibbs free energy for the ε(*hcp*) phase at high manganese contents >25 wt% (**Fig. 4.1-1d**), including a miscibility gap, for which there is no experimentally or theoretically support. Witusiewicz *et al*. [145] re-evaluated the Fe-Mn system close to that of [97] using new experimental data to determine the enthalpy of formation and the heat capacity of γ-Fe-Mn alloys, however producing less reasonable results at higher manganese contents [98], as can be seen from **Fig. 4.1-1c**. In the present work the evaluation by Huang [97] was used. First-principles descriptions of the *fcc/hcp* lattice stabilities of Fe-Mn alloys by Gebhardt *et al.* [146] are consistent with the thermodynamic calculations by [97], where a linear increase of $\Delta G^{\gamma \rightarrow \varepsilon}$ with additions of 15-40 wt.% manganese is obtained.
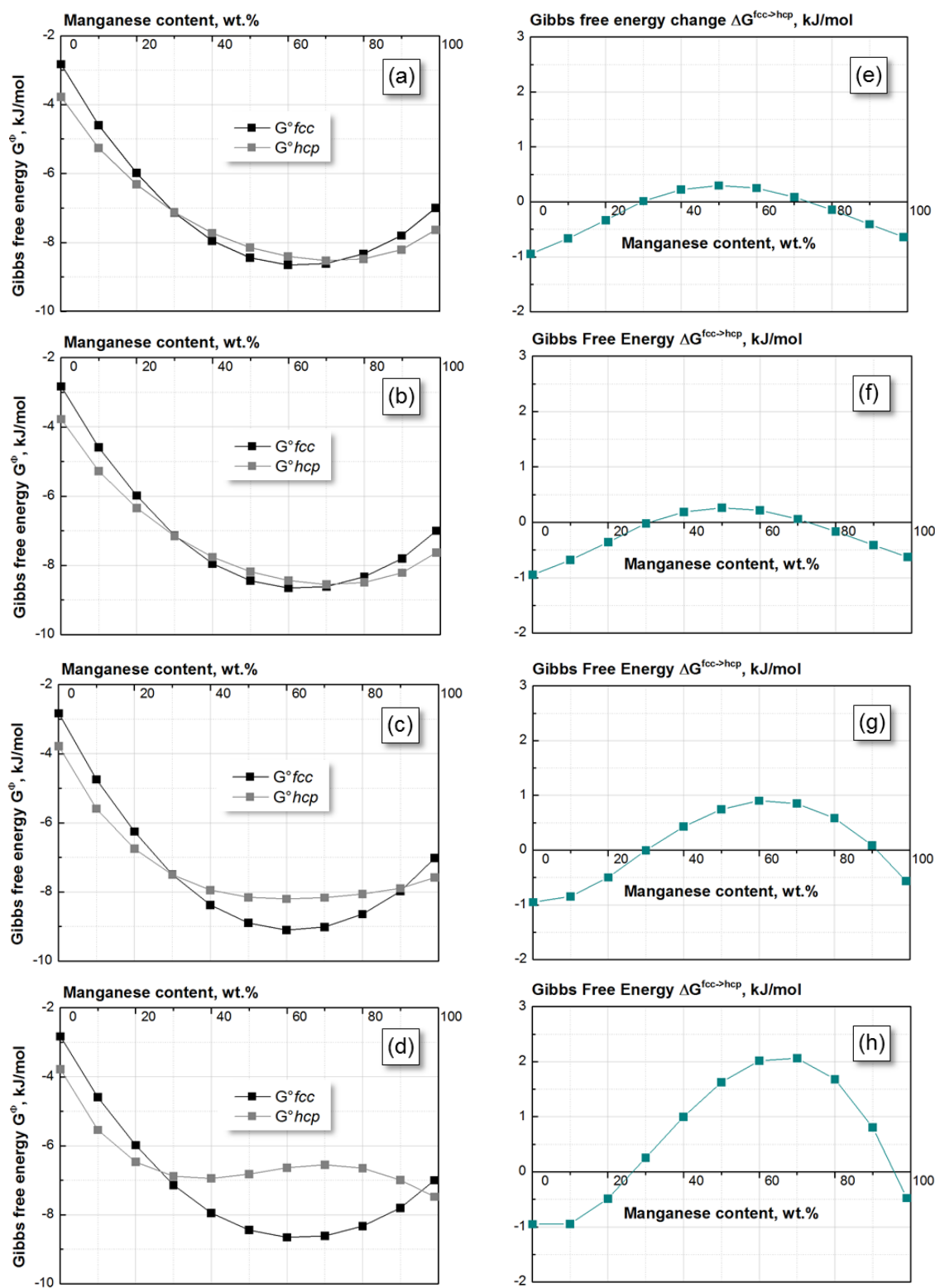
Fig. 4.1-1 Calculated $°G^{(fcc)}$ and $°G^{(hcp)}$ as function of manganese content (a-d) and the resulting difference in Gibbs free energy $\Delta G^{\gamma \rightarrow \varepsilon}$ in the Fe-Mn system at 298K (e-h) after (a,d) Huang [97], (b,e) Djurovic *et al.* [98], (c,f) Witusiewicz *et al.* [145], and (d-h) Nakano and Jacques [115].

Later, the higher ordered interaction parameter for the Fe-Cr-Mn-N system, including the ternary parameter $L^{(hcp)}_{Cr,Fe,Mn:Va}$ for the description of the *fcc* to *hcp* phase transformation temperature, was introduced by Qui [106] based on the $L^{(hcp)}_{Fe,Mn:Va}$ description after Huang [97], which was therefore used in the current work. The ternary interaction parameter $L^{(fcc)}_{Cr,Fe:N}$ was introduced by Frisk [105] to improve the solubility limits of nitrogen in austenite at high-pressures by fitting the experimental data from Feichtinger *et al.* [28]. However, after using this parameter in the $\Delta G^{\gamma\rightarrow\varepsilon}$ calculation, the experimental results from Lee *et al.* [60][73][136] and Hwang et al. [138][139] in the Fe-18Cr-10Mn system with higher nitrogen contents (see Tab. 4.1-1) could not be described sufficiently. For these steels, the model predicts a highly stable austenite phase, although after deformation the non-deformed γ-phase was transformed to ε- and α'-martensite (**Fig. 4.1-2a**). Previous results of Dimova et *al.* [147] on nitrogen solubility in Fe-22Cr-3Mn and Fe-21Cr-5Mn confirm considerably lower values as calculated for the *fcc* phase in the binary Fe-Cr system by Frisk [105]. Furthermore, the distances between the iso-$\Delta G^{\gamma\rightarrow\varepsilon}$ derivate with change in chemical composition, which implies uncertainties arising from the Cr-N interaction parameters.
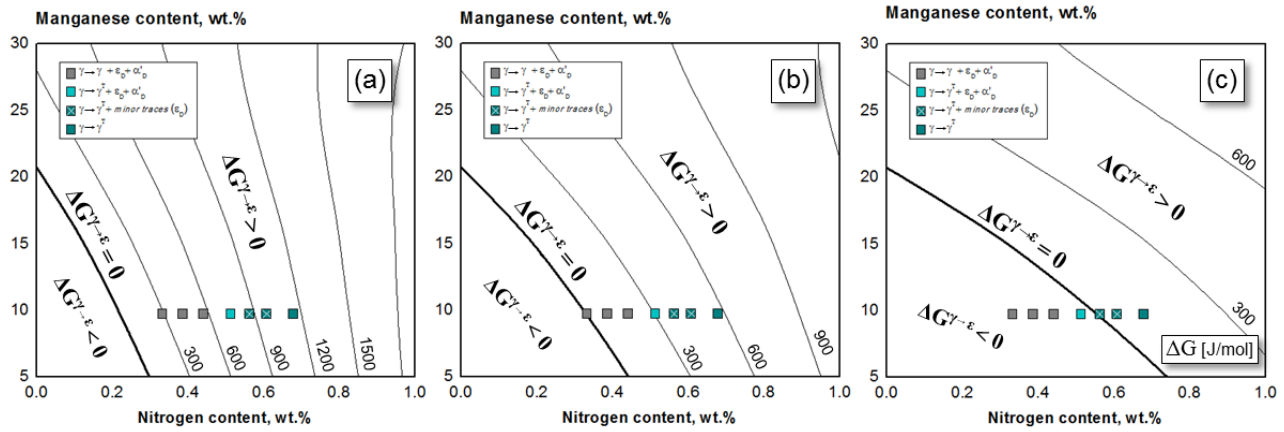

Fig. 4.1-2 Calculated $\Delta G^{\gamma\rightarrow\varepsilon}$-maps as function of manganese and nitrogen for Fe-18Cr-10Mn-N alloys at 300 K [60][73][139]. Variation of the $\Delta G^{\gamma\rightarrow\varepsilon} = 0$ line with respect to different interaction parameters: (a) $L^{(fcc)}_{Cr,Fe:N}$ and $L^{(fcc)}_{Cr,Fe:N,Va}$, (b) $L^{(fcc)}_{Cr,Fe:N}$ and $L^{(fcc)}_{Cr,Fe:N,Va} = 0$ after Frisk [105] and (c) $L^{(fcc)}_{Cr,Fe:N} = L^{(hcp)}_{Cr,Fe:N}$ and $L^{(fcc)}_{Cr,Fe:N,Va} = 0$ adapted within this work.

The parameter $L^{(fcc)}_{Cr,Fe:N,Va}$ as evaluated by Frisk [105] to adjust the miscibility gap of austenite and CrN nitride was set zero in this work due to its strong influence on the nitrogen solubility in austenite and thereby the stability of γ-phase (**Fig. 4.1-2b**). The $L^{(fcc)}_{Cr,Fe:N}$ was approximated by setting it equal to the parameter for the *hcp* phase, $L^{(hcp)}_{Cr,Fe:N}$ in order to adjust the $\Delta G^{\gamma\rightarrow\varepsilon} =0$ transition line as shown in **Fig. 4.1-2c**. A similar assumption was made by Frisk [66] for the binary parameter $L^{(hcp)}_{Cr,Mn:Va}$ that was set equal to $L^{(fcc)}_{Cr,Mn:Va}$ estimated by Lee [148] after examining the effect of manganese on the precipitation temperature of the *hcp* phase from fcc phase in Fe-Cr-Mn alloys. Since there are no further thermodynamic data available in the literature to reproduce the mentioned experimental observations, the adapted modification of the secondary and ternary interaction parameter $L^{(fcc)}_{Cr,Fe:N}$ and $L^{(fcc)}_{Cr,Fe:N,Va}$, respectively, lead to a reasonable accordance between experimental results and thermodynamic model calculation. All thermodynamic parameter used in the present work are listed in Tab. 4.1-2.

<u>Tab. 4.1-2</u> Thermodynamic parameters for the Fe-Cr-Mn-N system used from literature.*

fcc phase	*2 sublattice, sites 1:1, constituents $(Cr,Fe,Mn)_1(N,Va)_1$*	**Reference**
°G(fcc) Fe:Va	°G(bcc) Fe:Va $-1462.4+8.282T-1.15TlnT+6.4*10^{-4}T^2$	[149]
°G(fcc) Cr:Va	°G(bcc) Cr:Va $+7284+0.163T$	[150]
°G(fcc) Mn:Va	$-3439.3+131.884T-24.5177TlnT-0.006T^2+69600T^{-1}$	[151]
°G(fcc) Fe:N	°G(bcc) Fe:Va $+0.5$°G(gas) N_2 $-37460+375.42T-37.6TlnT$	[111]
°G(fcc) Cr:N	°G(bcc) Cr:Va $+0.5$°G(gas) N_2 $-124460+142.16T-8.5TlnT$	[111]
°G(fcc) Mn:N	$-75940+292.226T-50.294TlnT+265051T^{-1}$	[152]
L(fcc) Fe:N,Va	-26150	[148]
L(fcc) Cr:N,Va	20000	[111]
L(fcc) Mn:N,Va	$-69698+11.5845T$	[152]
*L(fcc) Cr,Fe:N***	*$-128930+86.49T+24330(y_{Cr}-y_{Fe})$*	[105]
L(fcc) Cr,Fe:N	$12826-19.48T$	this work
L(fcc) Cr,Fe:Va	$10833-7.477T-1410(y_{Cr}-y_{Fe})$	[150]
*L(fcc) Cr,Fe:N,Va***	*-162516 (only for fcc phase)*	[105]
L(fcc) Cr,Fe:N,Va	0	this work
L(fcc) Cr,Mn:N	-21237	[104]
L(fcc) Cr,Mn:Va	$-19088+17.5423T$	[148]
L(fcc) Fe,Mn:N	$53968-38.102T-28787(y_{Fe}-y_{Mn})$	[106]
L(fcc) Fe,Mn:Va	$-7762+3.865T-259(y_{Fe}-y_{Mn})$	[97]
L(fcc) Cr,Fe,Mn:N	-118000	[106]
L(fcc) Cr,Fe,Mn:Va	$6715-10.3933T$	[148]
β(fcc)	$-2.46y_{Cr}y_{Va}-2.1y_{Fe}y_{Va}-1.86y_{Mn}y_{Va}$	[106]
T Neel(fcc)	$-1109y_{Cr}y_{Va}-201y_{Fe}y_{Va}-1620y_{Mn}y_{Va}-y_{Fe}y_{Mn}y_{Va}[2282+2068(y_{Fe}-y_{Mn})]$	[106]
hcp phase	*2 sublattice, sites 1:1, constituents $(Cr,Fe,Mn)_1(N,Va)_1$*	
°G(hcp) Fe:Va	°G(fcc) Fe:Va $-2243.4+4.3095T$	[149]
°G(hcp) Cr:Va	°G(bcc) Cr:Va $+4438$	[150]
°G(hcp) Mn:Va	°G(fcc) Mn:Va $-1000+1.123T$	[153]
°G(hcp) Fe:N	°G(bcc) Fe:Va $+0.25$°G(gas) N_2 $-12015+37.98T$	[111]
°G(hcp) Cr:N	°G(bcc) Cr:Va $+0.25$°G(gas) N_2 $-65760+64.69T-3.93TlnT$	[111]
°G(hcp) Mn:N	$-60607+211.1807T-37.7331TlnT+129442T^{-1}$	[152]
L(hcp) Fe:N,Va	$10345-19.71T-(11130-11.84T)(y_N-y_{Va})$	[111]
L(hcp) Cr:N,Va	$21120-10.61T-6204(y_N-y_{Va})$	[111]
L(hcp) Mn:N,Va	$-7194-5.2075T-(11810-6.9538T)(y_N-y_{Va})$	[152]
L(hcp) Cr,Fe:N	$12826-19.48T$	[105]
L(hcp) Cr,Fe:Va	$10833-7.477T$	[105]
L(hcp) Cr,Mn:N	$-42187+32.48T$	[104]
L(hcp) Cr,Mn:Va	$-19088+17.5423T$	[104]
L(hcp) Fe,Mn:N	*no data available*	[106]
L(hcp) Fe,Mn:Va	$-5582+3.865T+273(y_{Fe}-y_{Mn})$	[97]
L(hcp) Cr,Fe,Mn:N	-185400	[106]
L(hcp) Cr,Fe,Mn:Va	34600	[106]
L(hcp) Fe:N,Va	$10345-19.71T-(11130-11.84T)(y_N-y_{Va})$	[111]
β(hcp)	$-2.46y_{Cr}y_{Va}-1.86y_{Mn}y_{Va}$	[148]
T Neel(hcp)	$-1109y_{Cr}y_{Va}-1620y_{Mn}y_{Va}$	[148]
bcc phase	*2 sublatices, sites 1:3, Constituents $(Cr,Fe,Mn)_1(N,Va)_3$*	
°G(bcc) Fe:Va	$1225.7+124.134T-23.5143TlnT-0.00439752T^2-5.89269*10^{-8}T^3+77358.5T^{-1}$	[149]
°G(bcc) Cr:Va	$-8856.94+157.48T-26.908TlnT+1.89435*10^{-3}T^2-1.47721*10^{-6}T^3+139250T^{-1}$	[154]
°G(bcc) Fe:N	°G(bcc) Fe:Va $+0.75$ °G(gas) N_2 $+93562+165.07T$	[111]
°G(bcc) Cr:N	°G(bcc) Cr:Va $+0.75$ °G(gas) N_2 $+311870+29.12T$	[111]

* All values are given in SI units J, mol and K. ** Parameter adjusted in this work parameter.

4.1.2.2 *Model validation with experimental data*

The calculated Gibbs free energy $\Delta G^{\gamma\rightarrow\varepsilon}$ maps at 300 K for the Fe-(Cr)-Mn-N system with constant chromium content of 5 wt.% and 18 wt.% are presented in **Fig. 4.1-3**, compared to the $\Delta G^{\gamma\rightarrow\varepsilon}$ maps without chromium. Increasing manganese and nitrogen results in an increase of $\Delta G^{\gamma\rightarrow\varepsilon}$ and a shift of the $\Delta G^{\gamma\rightarrow\varepsilon} = 0$ line to lower levels defining a stabilization of the *fcc* phase [96] [155]. The effect of up to 1 wt.% nitrogen on $\Delta G^{\gamma\rightarrow\varepsilon}$ is found to be 6 times the effect of manganese and 1.3-1.5 times the effect of carbon in Fe-Mn alloys with manganese variation between 5-35 wt.%, respectively [58].
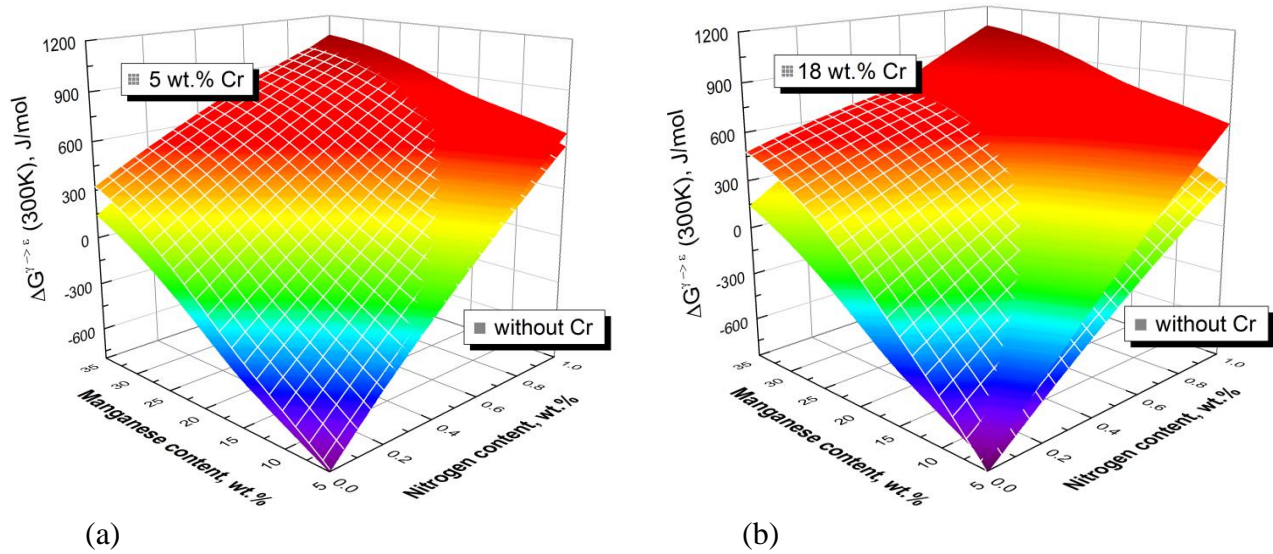

Fig. 4.1-3 Calculated $\Delta G^{\gamma\rightarrow\varepsilon}$ composition maps of Fe-Mn-N alloys (full-colored maps) and Fe-Cr-Mn-N alloys (white meshed maps) with (a) 5 wt.% Cr and (b) 18 wt.% Cr.

By adding chromium to the system, the *fcc* phase will be stabilized at lower nitrogen contents, as can be confirmed from the experimental results by Bracke *et al.* [64][65] in Fe-(0-10 wt.%)Cr-Mn-N-C steels, while at higher nitrogen contents the *hcp* phase becomes more favorable. This trend can be explained by the thermodynamic description of the *hcp* phase as M_2N nitride (see Chapter 3.1.1.1), which is Cr_2N nitride related to chromium. Accordingly, with increasing nitrogen content, chromium rather prefers to form a Cr_2N nitride than staying in the *fcc* solid solution. The preference of chromium to form a nitride will be enhanced both with increasing chromium and nitrogen in Fe-Mn by rising the chromium content from 5 wt.% **(Fig. 4.1-3a)** to 18 wt.% **(Fig. 4.1-3b)**. The thermodynamic calculation of $\Delta G^{\gamma\rightarrow\varepsilon}$ is verified by a number of chemical compositions in the Fe-Cr-Mn-N system available in the literature with the given microstructures before and after deformation at room temperature summarized in Tab. 4.1-1. The calculated $\Delta G^{\gamma\rightarrow\varepsilon}$ over nitrogen content is presented in **Fig. 4.1-4a**. In the present work, for all steels with estimated Gibbs energy $\Delta G^{\gamma\rightarrow\varepsilon} > 0$, the microstructures before and after deformation at room temperature are reported to be fully austenitic. The slightly negative $\Delta G^{\gamma\rightarrow\varepsilon}$ values of the two TRIP/TWIP alloys (**Fig. 4.1-4** light blue dots) are predicted close to $\Delta G^{\gamma\rightarrow\varepsilon} = 0$, which is quite reasonable as the microstructure exhibits mechanical twinning and transformation induced martensite formation after deformation. Whenever the initial austenitic microstructure is transformed to ε_D- and/or α'_D-martensite by deformation, the

calculated $\Delta G^{\gamma\rightarrow\varepsilon}$ values are negative. In this regard, the prediction of the available microstructural phases in the non-deformed as-received state - to be fully austenitic or partially martensitic (thermal ε- and/or α'-martensite) - is not possible since the composition dependency of the driving force for the $\gamma\rightarrow\varepsilon$ transformation is still not clearly described. For most of the reviewed steels with nitrogen and chromium contents lower than 0.1 wt.% and 5 wt.%, respectively, the calculation predicts positive $\Delta G^{\gamma\rightarrow\varepsilon}$ (**Fig. 4.1-4b**). That means, thermodynamically and mechanically the formation of ε- and/or α'-martensite is impossible, though, ε_D- or α'_D-martensite is observed in the microstructure. In the alloys with manganese contents lower than 5 wt.% delta ferrite up to 60 vol.% occurs in the as-received microstructure [84], which cannot be described with the applied model. This results in an overestimation of the *hcp* phase stability. Further, it is observed that higher alloying contents of Mn > 30 wt.% and Cr > 25 wt.% deviate with high scatter (**Fig. 4.1-4b**). It is concluded that the model can be applied for alloys with multi-phase microstructure. With increase in nitrogen a linear trend of increasing $\Delta G^{\gamma\rightarrow\varepsilon}$ is observed (**Fig. 4.1-4c**). However the *fcc/hcp* phase stability needs to be evaluated with respect to additional phases. Based on the evaluated boundary conditions, the model validity in the present work is set to: 0.1-1.0 wt.% nitrogen:, 5-25 wt.% chromium and 5-30 wt.% manganese.
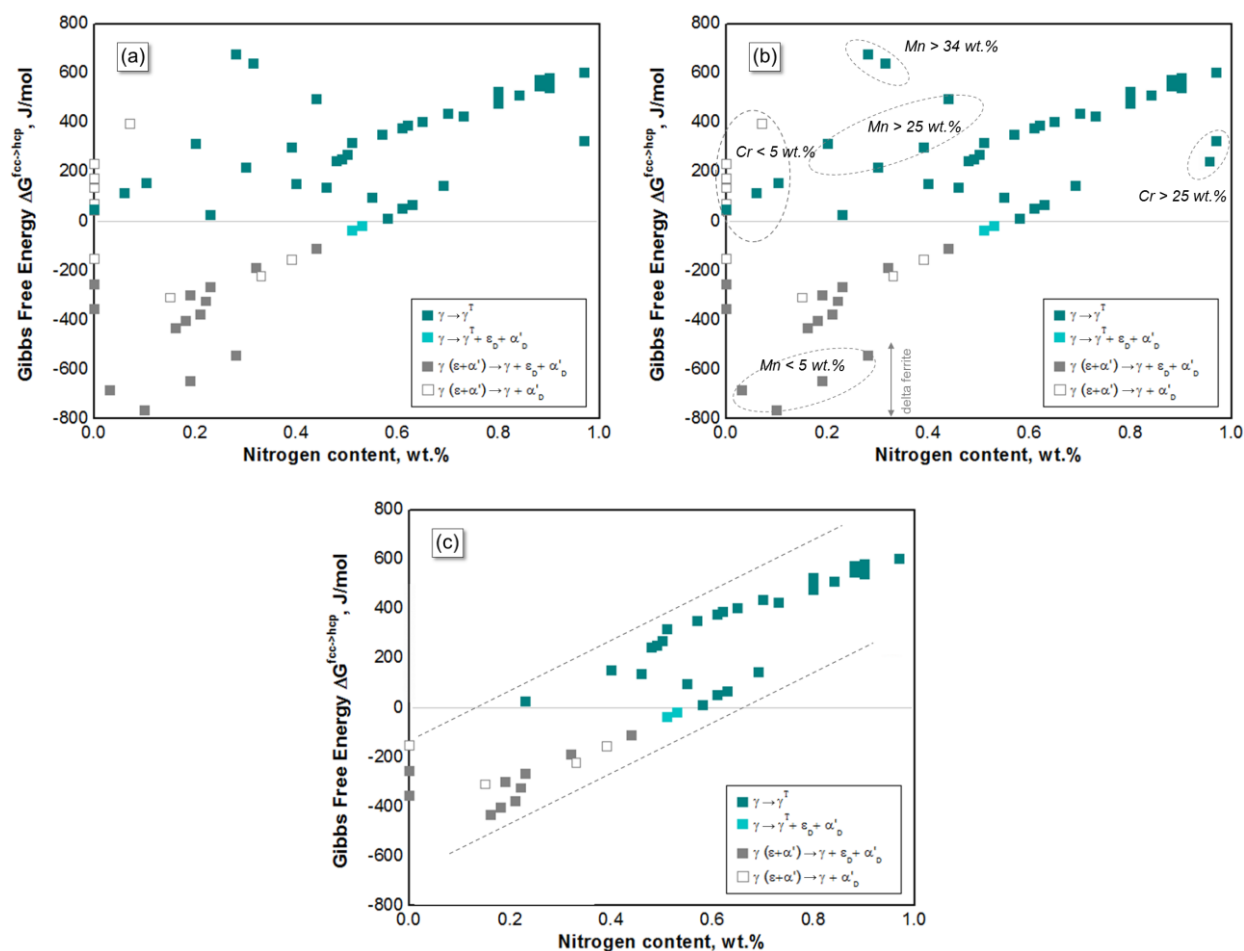

Fig. 4.1-4 Calculated effective Gibbs free energy, $\Delta G^{\gamma\rightarrow\varepsilon}$, as function of nitrogen content for the examined steels with the chemical compositions from Tab. 4.1-1 in the Fe-Cr-Mn-N system.

4.1.3 Thermodynamic modelling of SFE

According to Eq. (3.12) the SFE can be calculated after [113], where the interfacial energy, $\sigma^{\gamma/\varepsilon}$, is assumed as constant value for calculation of SFE_{linear}:

$$SFE_{linear} = 2\rho(\Delta G^{\gamma\rightarrow\varepsilon}) + 2\sigma^{\gamma/\varepsilon} \tag{4.1}$$

The effect of nitrogen on SFE in Fe-Cr-Mn alloys was considered in the SFE calculation using Eq. (4.1) by applying the two following main approaches:

(1) Using a constant interfacial energy, $\sigma^{\gamma/\varepsilon}$, where a segregation term $\Delta G^{\gamma\rightarrow\varepsilon}_{segr}$ is added to the Gibbs free energy, $\Delta G^{\gamma\rightarrow\varepsilon}$, as proposed by Ishida [79] and Yakubtsov et al. [23]:

$$SFE_{segr} = 2\rho\left(\Delta G^{\gamma\rightarrow\varepsilon} + \Delta G^{\gamma\rightarrow\varepsilon}_{segr}\right) + 2\sigma^{\gamma/\varepsilon} \tag{4.2}$$

(2) Assuming the interfacial energy as non-constant value, where $\sigma^{\gamma/\varepsilon}_{comp}$ is defined as a composition-dependent parameter:

$$SFE_{comp} = 2\rho\Delta G^{\gamma\rightarrow\varepsilon} + 2\sigma^{\gamma/\varepsilon}_{comp} \tag{4.3}$$

The molar surface density ρ was calculated after Allain et al. [156] with a geometrical-dependency expressed by the lattice parameter, a_γ, of austenite. For the nickel-free austenitic stainless steels, the following composition-dependent equation by Srinivas and Kutumbarao [157] was used to calculate a_γ as follows:

$$a_\gamma(nm)=0.3578+6\cdot10^{-5}x_{Cr}+9.5\cdot10^{-5}x_{Mn}+3.3\cdot10^{-3}x_C+2.9\cdot10^{-3}x_N \tag{4.4}$$

where x_i is the molar fraction of element i=Fe, Cr, Mn, N in the alloying system. As introduced by Ishida [79], the segregation term $\Delta G^{\gamma\rightarrow\varepsilon}_{segr}$ after Eq. (4.5) can be formulated as sum of the chemical free energy $\Delta G^{\gamma\rightarrow\varepsilon}_{chem}$ due to Suzuki segregation, Eq. (4.6), the surface free energy $\Delta G^{\gamma\rightarrow\varepsilon}_{surf}$ due to the difference in concentration of nitrogen between matrix and stacking faults, Eq. (4.7), and the elastic free energy $\Delta G^{\gamma\rightarrow\varepsilon}_{elast}$ which is related to the segregation of substitutional and interstitial elements that have different atomic sizes, estimated to be negligible [79]:

$$\Delta G^{\gamma\rightarrow\varepsilon}_{segr} = \Delta G^{\gamma\rightarrow\varepsilon}_{chem} + \Delta G^{\gamma\rightarrow\varepsilon}_{surf} + (\Delta G^{\gamma\rightarrow\varepsilon}_{elast}) \tag{4.5}$$

with

$$\Delta G^{\gamma\rightarrow\varepsilon}_{chem} = RT \sum x_N \ln\frac{x_{s(N)}}{x_N} \tag{4.6}$$

$$\Delta G^{\gamma\rightarrow\varepsilon}_{surf} = \frac{1}{4}\Lambda_N(x_{s(N)}-x_N)^2 \tag{4.7}$$

where

$$x_{s(N)}=\left[1+\frac{(1-x_N)}{x_N}\exp\left(\frac{-\Lambda_N}{RT}\right)\right]^{-1} \tag{4.8}$$

The parameter x_N and $x_{s(N)}$ represent the concentration of nitrogen in the bulk and at the stacking faults, respectively. Ishida [79] assumed the contribution of nitrogen segregation to stacking faults $\Delta G^{\gamma \to \varepsilon}_{segr}$ to be insignificant, while it was included in the model after Yakubtsov et al. [23], mainly considered in the $\Delta G^{\gamma \to \varepsilon}_{chem}$ and $\Delta G^{\gamma \to \varepsilon}_{surf}$ terms. Since the required interaction energies between nitrogen and stacking faults are not available from literature [23], the interaction values of nitrogen atoms with dislocations Λ_N were employed in the model. The interaction values Λ_N were taken from the experimental approximations by Gavrilljuk et al. [158] in the range of 0.13-0.52 wt.% nitrogen and extrapolated to 0-0.13 wt.% nitrogen after [23] as shown in **Fig. 4.1-5**. The calculated SFE_{linear}, Eq. (3.12), and SFE_{segr}, Eq. (4.2) are plotted in **Fig. 4.1-6**.
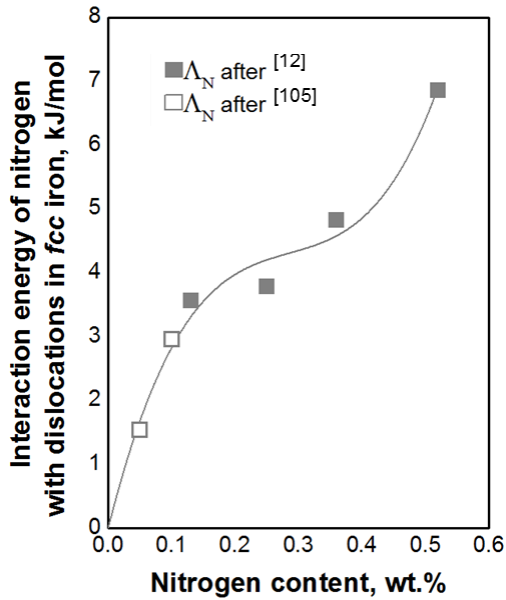
Fig. 4.1-5 Interaction energy of nitrogen with dislocations in *fcc* iron alloys [23][158] as function of nitrogen concentration.
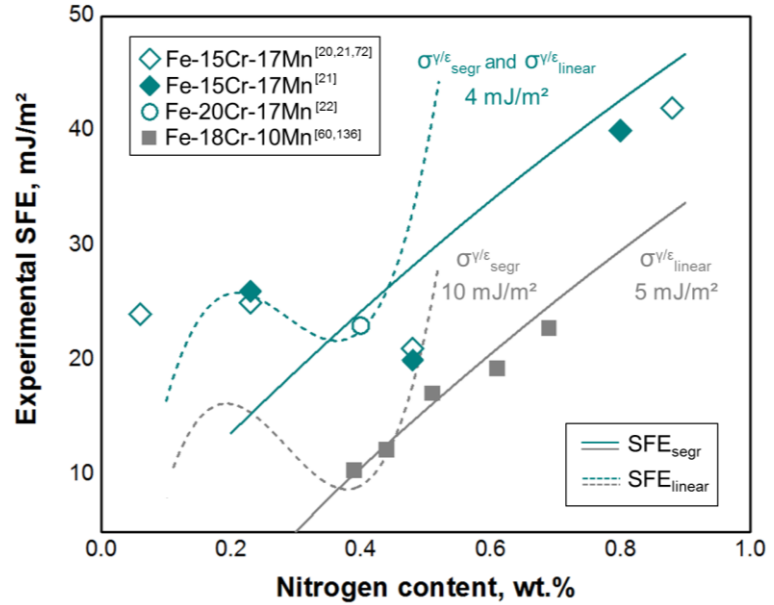
Fig. 4.1-6 Calculated SFEs using different approaches: SFE $_{linear}$ after Eq. (3.12) and SFE $_{segr}$ after Eq. (4.2) with adjusted $\sigma^{\gamma/\varepsilon}$ in comparison to experimental SFE values for Fe-15Cr-17Mn [20][21][72], Fe-20Cr-17Mn [22] and Fe-18Cr-10Mn [60][136].

The SFE model calculations are compared to experimentally measured SFE values in the Fe-15Cr-17Mn [20][21][72] and Fe-20Cr-17Mn [22] system. The Fe-18Cr-10Mn system investigated by Lee et al. [60][136] with 7 wt.% less manganese was used to represent the effect of manganese on SFE. In the lower range of nitrogen content, the calculated SFE_{segr} matches the experimentally SFE values, reproducing the drop of SFE with nitrogen in the Fe-(15-20)Cr-17Mn system. With increasing nitrogen contents above ~0.4 wt.%, the model deviates from the experimental results. The model calculation of SFE $_{linear}$ is applicable for nitrogen contents ≥0.4 wt.% in high and low-manganese systems, however the non-monotonous relation of SFE with increasing nitrogen is not reproduced. The interfacial energy term $\sigma^{\gamma/\varepsilon}$ was set as constant value for the calculation of SFE $_{linear}$ and SFE $_{segr}$. With decreasing manganese content the $\sigma^{\gamma/\varepsilon}$ was adjusted from $\sigma^{\gamma/\varepsilon} = 4$ mJ/m² for the Fe-15Cr-17Mn alloys to $\sigma^{\gamma/\varepsilon} = 5$-10 mJ/m² for the Fe-18Cr-10Mn alloys. It is assumed that the $\sigma^{\gamma/\varepsilon}$ is a function of chemical composition rather than a constant parameter in the SFE calculation. Published

experimental and calculated data about the dependency of $\sigma^{\gamma/\varepsilon}$ on the chemical composition in Fe-Cr-Mn-N systems are not available until now. To estimate $\sigma^{\gamma/\varepsilon}$ by Eq. (3.12), an experimental approximation after Olsen and Cohen [95] was adopted that indirectly calculates the $\sigma^{\gamma/\varepsilon}$ using the experimentally measured SFE values, extracted from the literature, together with the calculated $\Delta G^{\gamma \to \varepsilon}$, according to Chapter 0. In **Fig. 4.1-7a**, the parabolic fit to the experimental SFEs is shown. The fitting curve was adjusted according to the SFE of the Fe-(15-20)Cr-17Mn alloys and applied to the Fe-18Cr-10Mn alloying system. Although the chromium content of the Fe-20Cr-17Mn was much higher than in the Fe-15Cr-17Mn alloys with the same manganese content, the SFE value of this alloy matches the applied polynomial fit.
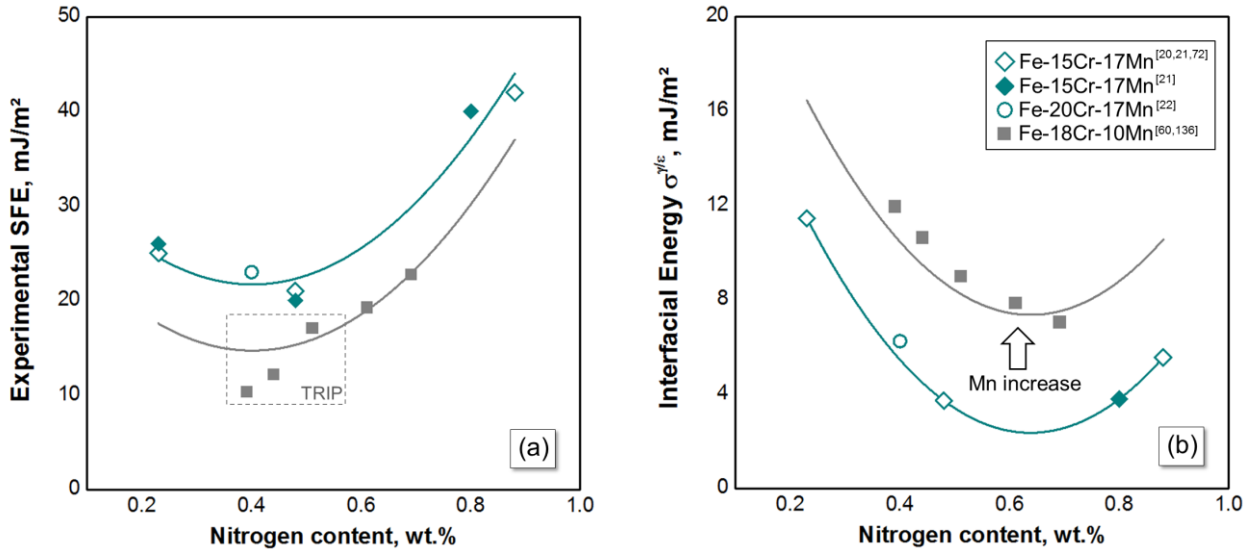
Fig. 4.1-7 Polynomial fit of (a) experimentally SFE values and (b) calculated interfacial energy, $\sigma^{\gamma/\varepsilon}$, in Fe-15Cr-17Mn [20][21][72], Fe-20Cr-17Mn [22] and Fe-18Cr-10Mn [60][136].

Based on the fitted SFE data, the applied $\sigma^{\gamma/\varepsilon}$ was defined as second order polynomial fit depending on nitrogen and manganese contents, shown in **Fig. 4.1-7b**, as follows:

$$\sigma^{\gamma/\varepsilon} = 54.6_w x_N^2 - 69.7_w x_N^2 + (36.5 - 0.7_w x_{Mn}) \tag{4.9}$$

where $_w x_i$ is the weight fraction of element i in the alloying system. The function defines a parabolic influence of nitrogen on $\sigma^{\gamma/\varepsilon}$, while the effect of manganese is reflected by a linear factor of 0.7. Due to the lack of experimental SFE data for Fe-Cr-Mn-N alloys with varying chromium content, the valuation on the effect of chromium on $\sigma^{\gamma/\varepsilon}$ was not possible. However, only minor deviation from the trend of SFE over nitrogen content for the Fe-20Cr-17Mn alloy in comparison to the Fe-15Cr-17Mn alloys is observed (**Fig. 4.1-7a**). In the current work, the effect of chromium on $\sigma^{\gamma/\varepsilon}$ was assumed to be negligible. The calculated $\sigma^{\gamma/\varepsilon}$ values are shown in **Fig. 4.1-8** plotted over (a) nitrogen and (b) manganese content in the Fe-Cr-Mn-N system. The predicted trend of $\sigma^{\gamma/\varepsilon}$ over manganese is compared to existing data in the literature for binary Fe-Mn. The effect of nitrogen on $\sigma^{\gamma/\varepsilon}$ is produced as a non-monotonous trend according to the applied polynomial fit of second order with a minimum at ~0.6 wt.%. The $\sigma^{\gamma/\varepsilon}$ was found to linear decrease with increasing manganese content within the present model. The obtained values of $\sigma^{\gamma/\varepsilon}$ by Cotes *et al.* [96] from the experimental SFE

data after Volosevich *et al.* [87] and Schumann [159] in low carbon binary Fe-Mn systems show a similar trend of decreasing $\sigma^{\gamma/\varepsilon}$ up to 25 wt.%. The data of [87] arise from the corresponding SFE values at room temperature; however, this trend is not corroborated with further experimental SFE measurements at this time. The parabolic trend of $\sigma^{\gamma/\varepsilon}$ over manganese observed for the Fe-Mn-3Al-3Si alloys [85] (**Fig. 4.1-8b**) is similar to the works by [87][96], although the experimental SFE values indicate a linear dependency of SFE as function of manganese [85]. The appearance of a minimum in the $\sigma^{\gamma/\varepsilon}$ curve over manganese is not reproduced with the present model.
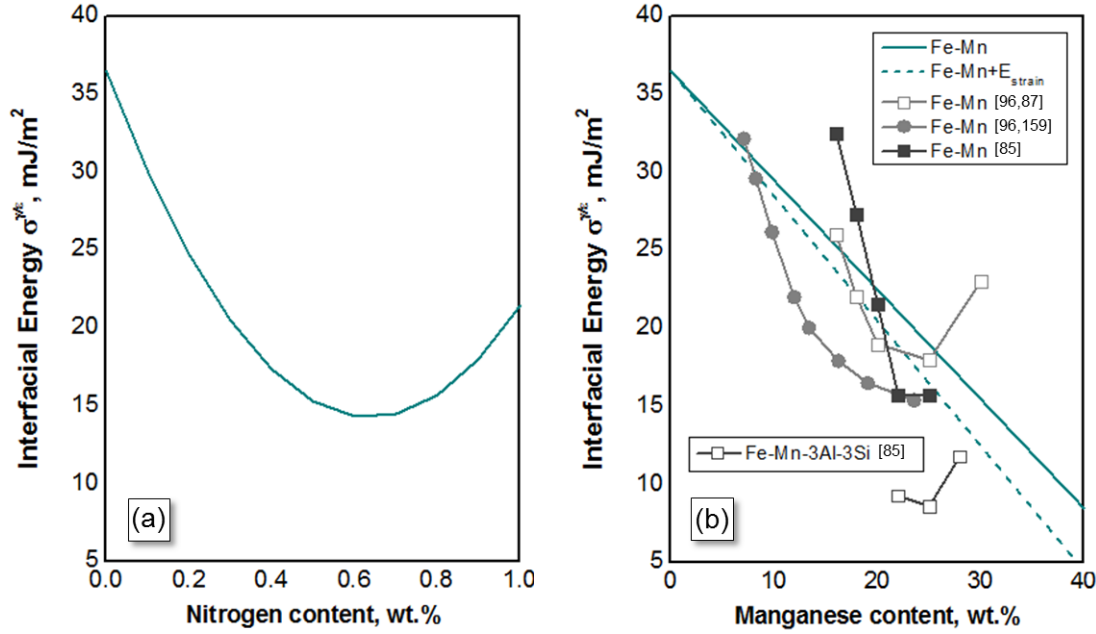
Fig. 4.1-8 Calculated interfacial energy, $\sigma^{\gamma/\varepsilon}$, of pure iron over (a) nitrogen and (b) manganese in comparison to various literature data.

The difference in the respective values obtained by Pierce *et al.* [85] and Cotes *et al.* [96] may be attributed to the term for the coherency strain energy, E_{strain} (Chapter 2.2.3), included in both model assessments, according to Eq. (4.10). The assessment after [96] indicates E_{strain} in the order of 40 J/mol and weakly dependent upon composition. The determination of E_{strain} by [85] reveals comparatively high values of E_{strain} ~90-107 J/mol for 16-25 wt.% manganese, which is reflected in the general higher $\sigma^{\gamma/\varepsilon}$ values.

$$SFE_{effective} = 2\rho(\Delta G^{\gamma\rightarrow\varepsilon} + E_{strain}) + 2\sigma^{\gamma/\varepsilon}_{comp} \tag{4.10}$$

In order to investigate the influence of coherency strain energy on the SFE, a constant E_{strain} with 40 J/mol after [95][96] was included to the model calculation of SFE_{comp}, and is further referred as $SFE_{effective}$. **Fig. 4.1-9** presents the calculated SFE_{comp} values relative to the experimentally measured SFE showing an excellent agreement, which supports the calculation of SFE with the polynomial description of $\sigma^{\gamma/\varepsilon}$ as function of nitrogen and manganese. Moreover the SFE calculation accurately predicts the *fcc* phase stability and the active deformation mechanism for a wide range of chemical compositions in the Fe-Cr-Mn-N system.
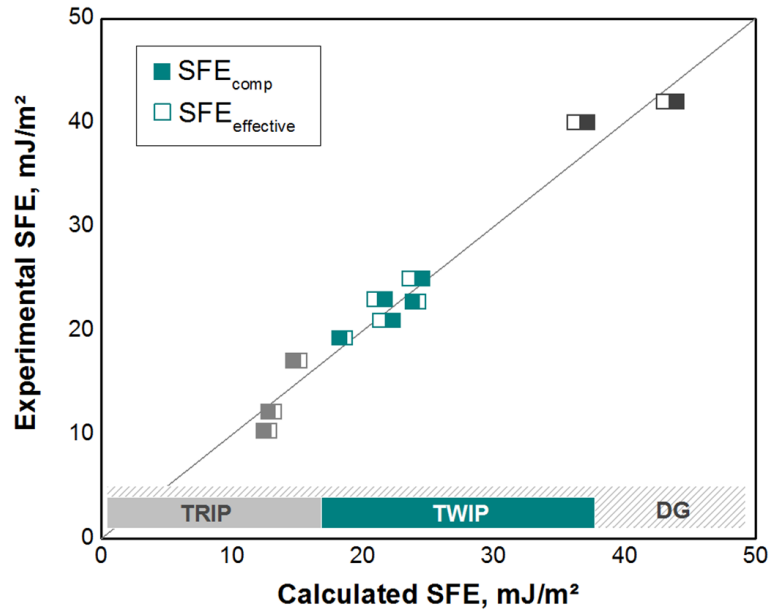
Fig. 4.1-9 Comparison of experimental and calculated SFE in the Fe-Cr-Mn-N system. The SFE$_{effective}$ values include E$_{strain}$ = 40 J/mol.

Fig. 4.1-10 Calculated effective Gibbs free energy, $\Delta G^{\gamma \to \varepsilon}$, versus SFE $_{comp}$ and SFE $_{effective}$ (includes E$_{strain}$ = 40 J/mol) for the examined steels with the chemical compositions from Tab. 4.1-1 in the Fe-Cr-Mn-N system.

The calculated SFE$_{effective}$ values exhibit minor derivation from the experimental SFE. From **Fig. 4.1-10** the difference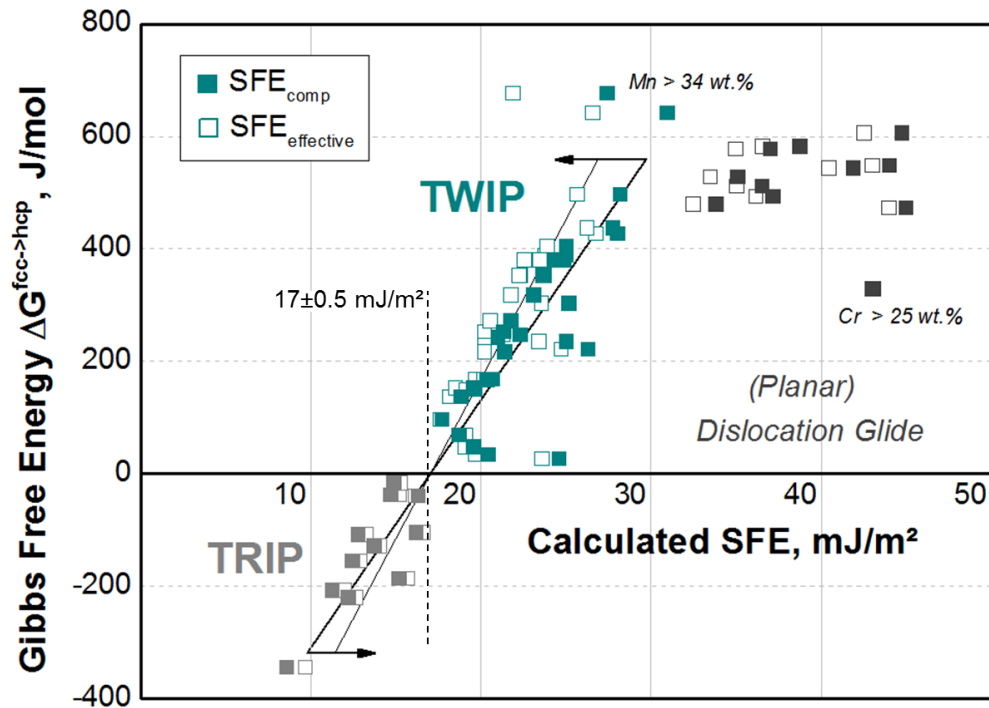 in SFE$_{comp}$ and SFE$_{effective}$ becomes more apparent. Using the model assessment of SFE$_{comp}$, steels with a positive calculated effective Gibbs free energy change, $\Delta G^{\gamma \rightarrow \varepsilon}$, are expected to have a SFE > 17±0.5 mJ/m² which was assigned for the activation of deformation induced twinning, and approves the mechanical stability of the γ-phase. For all steels where deformation induced ε- or α'-martensite formation was observed, the calculated $\Delta G^{\gamma \rightarrow \varepsilon}$ was found to be negative and the corresponding SFE values were lower than 17±0.5 mJ/m². Considering the coherency strain energy, E$_{strain}$, a shift in the calculated SFE$_{effective}$ relative to the SFE$_{comp}$ values is observed, that is more dominant in the TWIP region, than in the TRIP region, which might be related to a change in the description of the $\sigma^{\gamma/\varepsilon}$ over manganese. If E$_{strain}$ is considered, the linear factor in Eq. (4.9) that is related to the effect of manganese on $\sigma^{\gamma/\varepsilon}$ increases from 0.7 to 0.8, to reproduce the experimental data according to **Fig. 4.1-7a**. By that, the effect of manganese on $\sigma^{\gamma/\varepsilon}$ becomes more significant if E$_{strain}$ is included in the SFE model after Eq.(4.9). As the TRIP region is mainly accounted for alloys with low manganese contents (see <u>Tab. 4.1-1</u>), the influence of $\sigma^{\gamma/\varepsilon}$ variation on SFE is less distinct. For SFE values above 30-40 mJ/m² the occurrence of deformation twinning is likely to be suppressed in favor of pure DG. A strict division for the SFE values between the TWIP region and area of pure DG is not suggested as only few works in the literature (**Fig. 4.1-10** dark gray dots) reported the deformation mechanism to be fully controlled by dislocation glide without mechanical twinning to occur. The calculated SFE$_{comp}$ maps at 300 K for the Fe-Mn-N system with the constant chromium contents of 5 wt.% and 18 wt.% are presented in **Fig. 4.1-11a** and **Fig. 4.1-11b**, respectively. With increasing the manganese and nitrogen content, the SFE increases. At higher nitrogen contents the SFE exhibits a slight drop which is more pronounced at lower chromium contents, which can be explained due to the continuous decrease of $\sigma^{\gamma/\varepsilon}$ with increasing manganese content. This trend however, only occurs for very high SFE levels, where twinning plays a subordinate role as a deformation mechanism. Experimental data on the effect of manganese on SFE in this range of chemical compositions are not available.

(a)   (b)
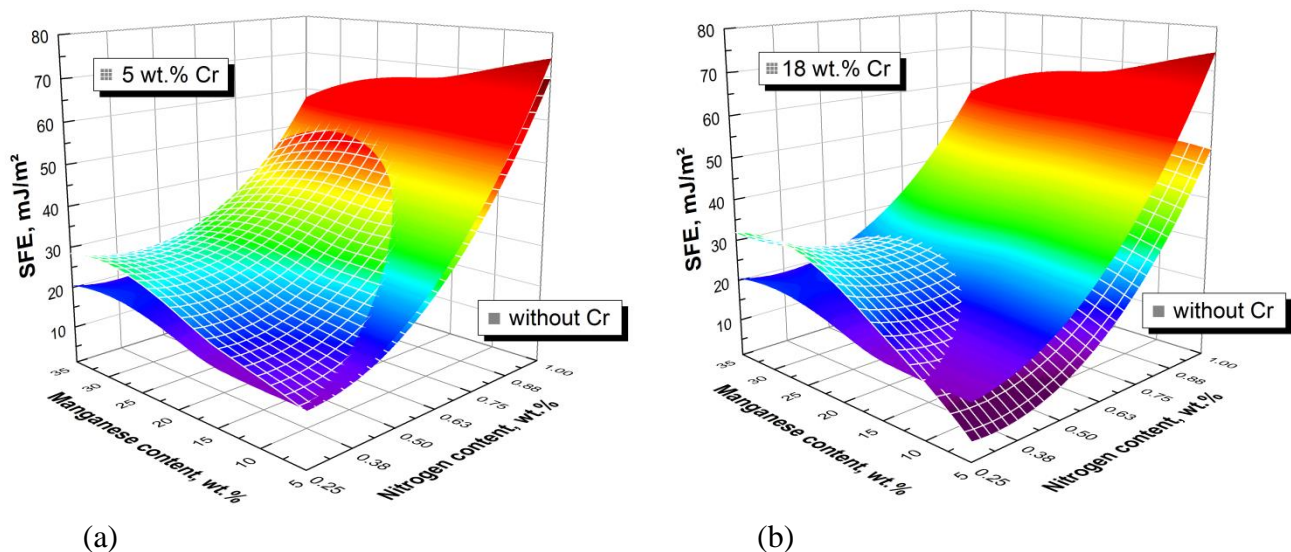
Fig. 4.1-11 Calculated SFE-maps of Fe-Mn-N alloys (full-colored maps) and Fe-Cr-Mn-N alloys (white meshed maps) with (a) 5 wt.% Cr and (b) 18 wt.% Cr.

4.2 Alloy design

4.2.1 Phase diagram

The phase equilibria in the Fe-Cr-Mn-N system were calculated using the Thermo-Calc software and the TCFE 6 database, according to Chapter 3.1.2. In **Fig. 4.2-1** the isoplethal phase diagram as function of temperature and nitrogen content, depending on variations in the alloying content of chromium and manganese, are shown. With respect to the process requirements for strip casting the phase diagram are analyzed in terms of: (1) the equilibrium nitrogen solubility in the melt at atmospheric pressure of 1 bar and (2) the liquid/austenite solidification region.
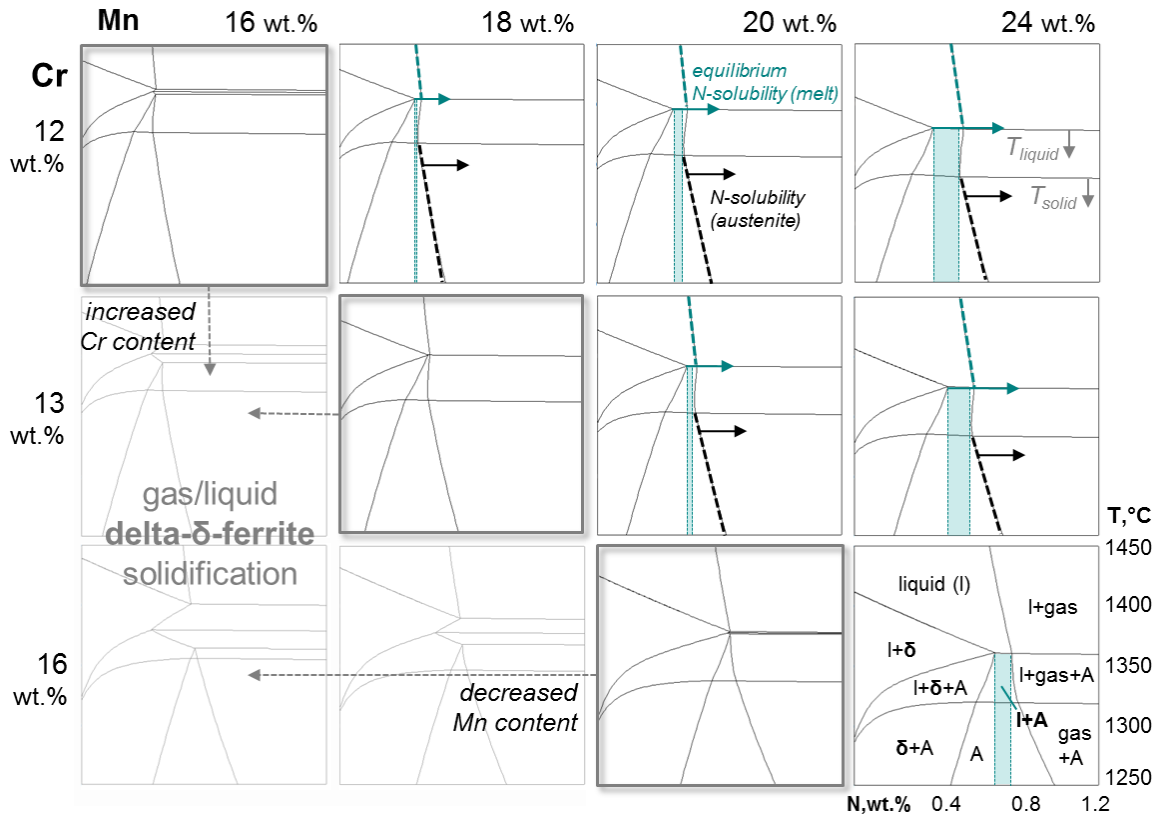
Fig. 4.2-1 Calculated phase diagram for various chemical compositions in the Fe-Cr-Mn-N system in dependence of temperature and nitrogen content.

The nitrogen solubility in the melt decreases rapidly with decreasing temperature, chromium and manganese content. The increasing effect of chromium and manganese content on the nitrogen solubility limits is related to the decrease in T_{liq}. In the low alloyed Fe-Cr-Mn-N systems the two main solidification regions liquid/δ-ferrite/austenite and liquid/gas/austenite are observed. The δ-ferrite solidification in iron alloys is associated with a wide solubility gap and a sudden drop of nitrogen solubility, leading to the formation of pores and outgassing of nitrogen [28], therefore needs to be avoided. The δ-ferrite solidification region is extended with increased chromium and decreased manganese contents, as can be seen in **Fig. 4.2-1**. By adjusting the chemical composition with respect to the chromium/manganese ratio, the δ-ferrite solidification can be suppressed and the

solidification occurs directly from liquid to austenite, through the liquid/austenite region. The temperature range of the liquid/austenite solidification is characterized by only slight solubility differences [30] and the dissolved nitrogen in the melt can be assumed to be almost completely transferred and dissolved in the austenite phase. With increase in chromium content from 12 wt.% up to 16 wt.% the liquid/austenite solidification region becomes restricted with respect to the range of nitrogen, and is shifted towards higher nitrogen contents. For high chromium contents >16 wt.% a minimum of 24 wt.% manganese needs to be alloyed to ensure a δ-ferrite-free solidification trough the liquid/austenite region.

Industrial requirements for automotive applications of the Fe-Cr-Mn-N alloy designs require a minimum chromium content of 13 wt.% to ensure a sufficient ability for nitrogen solubility in the melt and appropriate wet-corrosion resistance. In order to suppress the δ-ferrite solidification, the chromium content was set constant to 13 wt.%. The increase in nitrogen solubility and the stabilization of the liquid/austenite solidification region was achieved by adjusting the manganese content. In **Fig. 4.2-2** the calculated isoplethal phase diagram for the designed Fe-13Cr-Mn-N alloys with (a) 20 wt.%, (b) 22 wt.% and (c) 26 wt.% manganese as function of temperature and nitrogen content are shown. The nickel and carbon content were set to 0.5 wt.% and 0.1 wt.%, respectively. The liquid/austenite solidification region is highlighted in blue color.
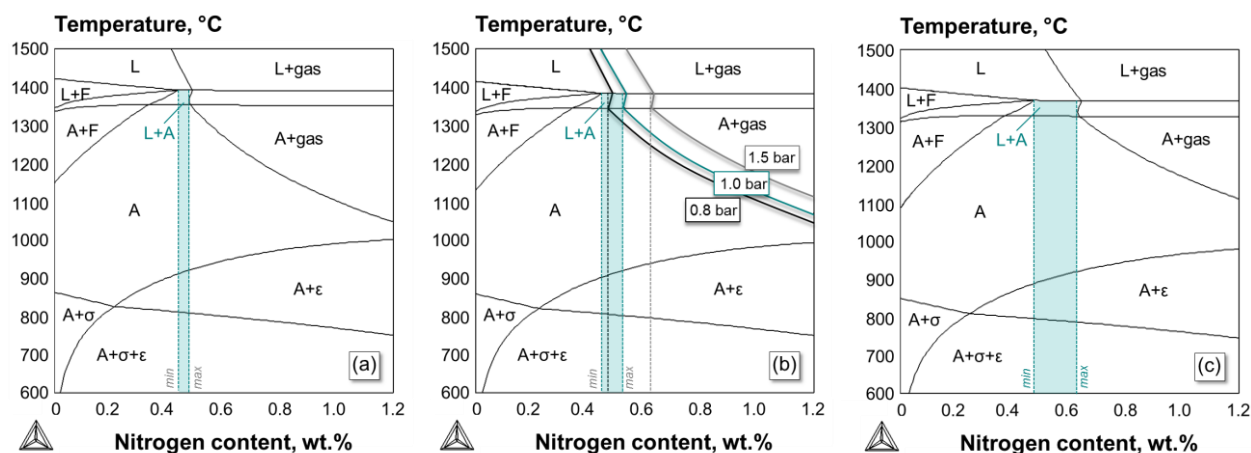
Fig. 4.2-2 Phase diagram for the alloy designs of (a) 13-20CrMn comp I, (b) 13-22CrMn comp II with respect to the solubility limits of nitrogen in the melt under gaseous nitrogen pressure of 0.8, 1.0, 1.5 bar and (c) 13-26CrMn comp III. The blue colored areas represent the nitrogen solubility limit (max/min) within the liquid/austenite solidification region.

With increasing manganese content from 20-26 wt.% the predicted liquid/austenite solidification region shifts to higher nitrogen contents and extends with respect to the nitrogen solubility limits (max/min). Comp III with 26 wt.% manganese reveals a wide liquid/austenite solidification area between 0.48-0.63 wt.%, offering best conditions in terms of technical feasibility for the strip-casting process. Based on the alloying concept of comp II an industrial strip-cast alloy was processed (comp IC). Due to the different process line, Chapter 3.2.1, variations in the nitrogen gas pressure during casting needs to be considered in the calculation of the phase diagram. **Fig. 4.2-2b** illustrates the nitrogen solubility limit within the liquid/austenite solidification region of comp II as function of pressure, extending to higher nitrogen contents with increase in pressure.

4.2.2 Solubility calculations

In order to develop the nitrogen solubility model after Sieverts for the quaternary Fe-Cr-Mn-N system, the first and second order interaction parameter e_N^{Mn} and r_N^{Mn} between Mn and N in Fe-Mn-N melts from various literatures have been evaluated (Tab. 4.2-1).

Tab. 4.2-1 First and second order interaction parameter e_N^{Mn} and r_N^{Mn}
between Mn and N in Fe-Mn-N melts from various literatures.

Reference		Interaction parameter		Interaction parameter at 1786 K	
		e_N^{Mn}	r_N^{Mn}	e_N^{Mn}	r_N^{Mn}
Satir91	[32][34]	-0.024	3.2E-5	-0.024	3.2E-5
Schür67	[117], Satir91 [32][34]	-0.020	3.2E-5	-0.020	3.2E-5
Rasev79	[160]	-0.023	7.5E-5	-0.023	7.5E-5
Grigor90	[161]	-73/T+0.022	0.8/T+3.8E-4	-0.019	6.8E-5
Gavr99	[50], Grigor90 [161]	-0.021	0.8/T+3.8E-4	-0.021	6.8E-5
Shin11	[162], Grigor90 [161]	-59.6/T+0.011	0.8/T+3.8E-4	-0.0224	6.8E-5
Christ14	[163]	-0.023	1.059E-5	-0.023	1.059E-5

The calculated nitrogen solubility at 1786 K is plotted over manganese content in **Fig. 4.2-3**, compared to experimental measured nitrogen solubility values by Christmann *et al.* [163] in Fe-Mn alloys. The equilibrium constant $\log K_N = (-850/T)-0.905$ evaluated for Fe-Cr-Mn-N alloys as function of temperature [116] was used (**Fig. 4.2-3a**). To calculate the nitrogen solubility for temperatures other than 1600°C, the temperature correction term $f_N^{(T)}$ according to Eq. (3.20) was applied to the model (**Fig. 4.2-3b**). For all calculations the nitrogen concentration in the melt increases with manganese content, which is in accordance to experimental results [163][162]. The interaction parameter of first order characterizes the slop of the curve, while the second order interaction parameter defines the deflection [50]. Using the interaction parameter proposed by
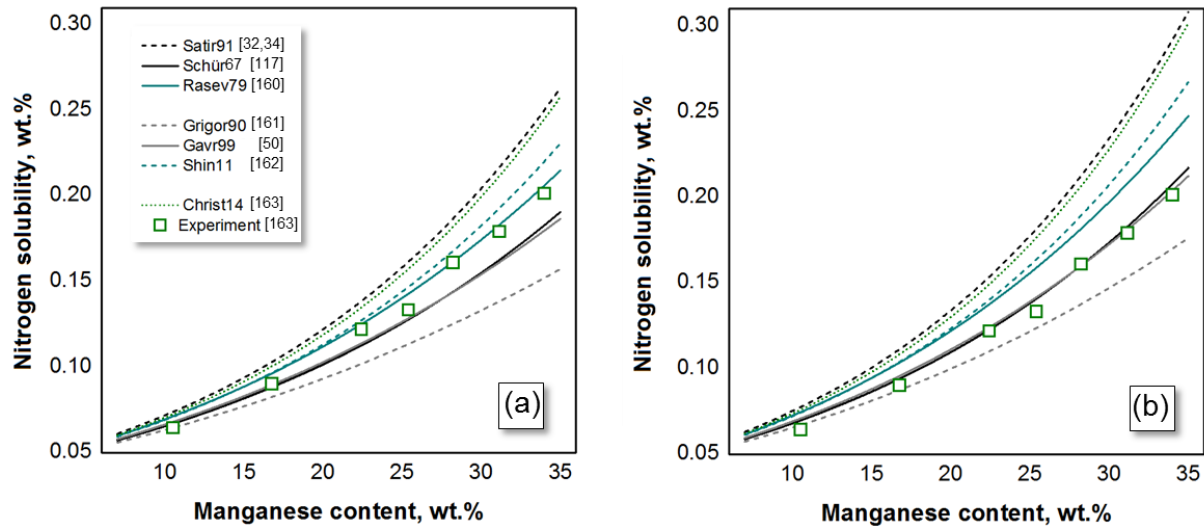

Fig. 4.2-3 Nitrogen solubility as function of manganese content calculated at 1786 K for different model parameter sets (1) without and (2) with taking the temperature correction term $f_N^{(T)}$ into account; compared to experimental measured nitrogen solubility in Fe-Mn alloys after [163].

Satir *et al.* [32][34] and Christmann *et al.* [163] the nitrogen solubility is overestimated, while applying the interaction parameter from Grigorenko and Pomarin [161] the calculated nitrogen solubility is lower than the experimental values, independent of $f_N^{(T)}$ consideration. According to Shin *et al.* [162] a temperature dependent interaction parameter $e_N^{Mn}(T)$ of first order needs to be taken into account in order to imply the temperature dependency between manganese and nitrogen in Fe-Mn-N melts. At 1786 K the value for the $e_N^{Mn}(T)$ parameter by Shin *et al.* [162] is determined as -0.0224 (Tab. 4.2-1). The resulting function of nitrogen solubility over manganese content shows close accordance with the experimental measured values (**Fig. 4.2-3a**). The parameter set by Rasev and Ivanov [160] shows best approximation with minor deviation from the experimental results, particularly at higher manganese contents. Regarding the temperature correction term $f_N^{(T)}$ mainly the slop of the curves increases, enhancing the nitrogen solubility at high manganese concentrations. As can be seen from **Fig. 4.2-3b**, applying the $f_N^{(T)}$ term to the model calculations by Shin *et al.* [162] and Rasev and Ivanov [160] the nitrogen solubility is overvalued, due to the enhanced slop of the plotted solubility line. Using $f_N^{(T)}$, the determined nitrogen solubility calculated after Schürmann and Kunze [117] and Gavriljuk and Berns [50] are in good agreement to the experimental results.

The parameter sets with the best accordance to the experimental results at 1786 K are furthermore used to evaluate the model to temperatures up to 1873 K, shown in **Fig. 4.2-4a-c**. The calculated values are validated with experimental nitrogen solubility in Fe-Mn alloys at 1786 K after [163] and at 1823 K and 1873 K after [162]. The interaction parameter set after Rasev and Ivanov [160] reveal the best accordance to the experimental values at high temperatures, particularly for increased manganese contents. Distinct deviation is observed for the calculation after [50]. At high manganese contents the slop of the curve is not predicted accurately, which results in the underestimation of the nitrogen solubility for temperatures other than 1786 K. The solubility calculation using the parameter sets by [117] and [162] reproduce quite reasonable results for the low-manganese regime, however at higher for higher manganese contents the accuracy of the model is lacking. On the basis of the presented results, the interaction parameter e_N^X and r_N^X of manganese and chromium with nitrogen after [160] are employed in the current work (Tab. 4.2-2). Secondary interaction parameter are accounted for chromium and manganese to consider the effect on N solubility for Cr > 2.5 wt.% and Mn, Ni > 5 wt.% [50]. Primary interaction parameter for nickel and carbon are taken from Satir-Kolorz *et al.* [33].

Tab. 4.2-2 First and second order interaction parameter e_N^X and r_N^X of Cr and Mn after [160], Ni and C after [33] for the dissolution of N in the Fe-Cr-Mn alloy melt.

X	Interaction parameter	
	e_N^X	r_N^X
Cr	-0.046	3.0E-4
Mn	-0.023	7.5E-5
Ni	0.011	-
C	0.118	-

Fig. 4.2-4d represents the estimated content of dissolved nitrogen in the melt for the Fe-13Cr-Mn pilot alloy designs of comp I-III. The temperature of the melting pool for the strip-casting process was set to ~1823 K±50 K (compare Chapter 3.2.1), taking the effect of chemical composition on T_{liqu} into account, as T_{liqu} decreases with increasing manganese content (Chapter 4.2.1).
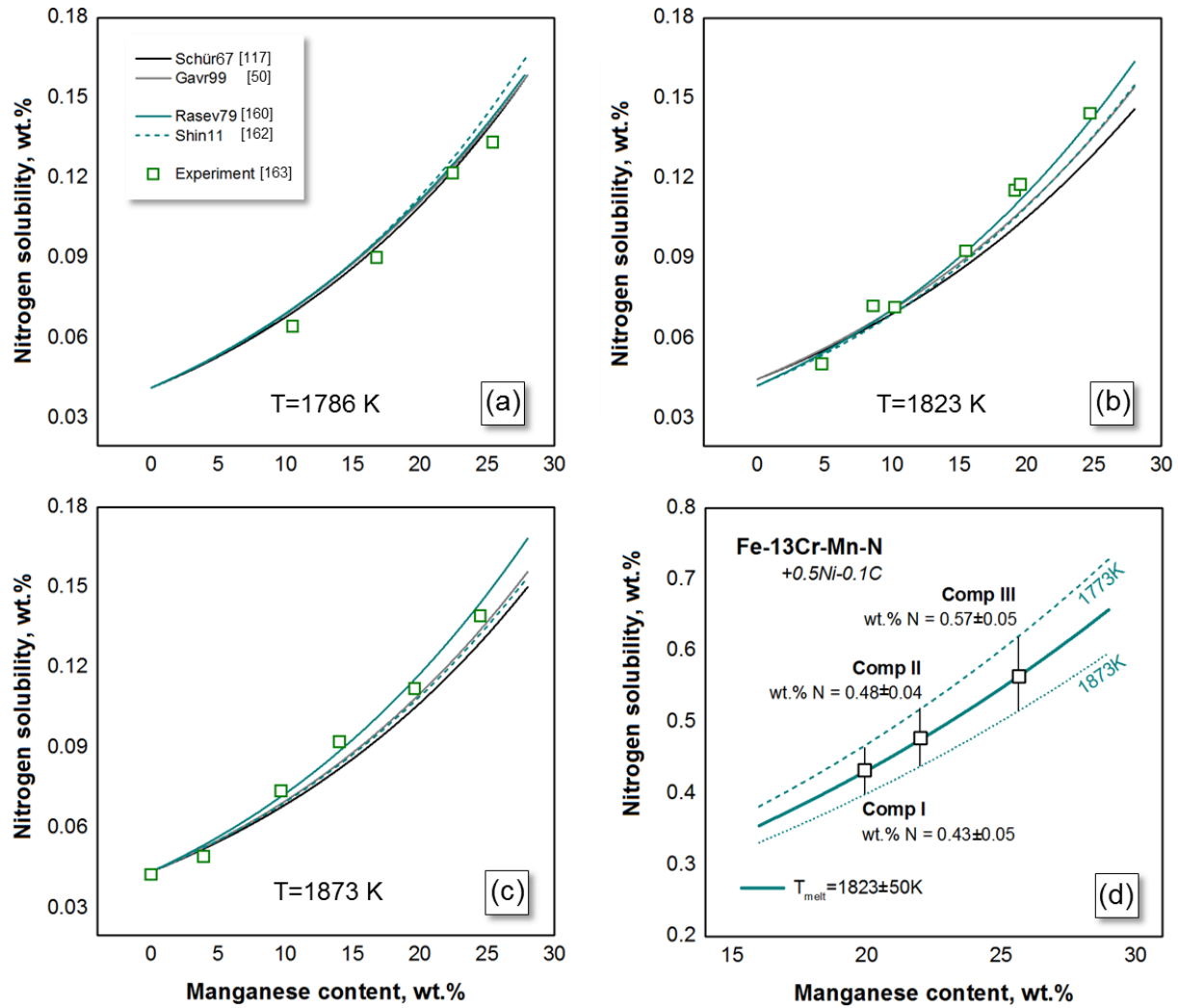
Fig. 4.2-4 Nitrogen solubility as function of manganese content for different temperatures and interaction parameter sets compared to experimental measured nitrogen solubility in Fe-Mn alloys after (a) [163] and (b,c) [162]. Calculated nitrogen solubility for the Fe-13Cr-Mn-N pilot alloy designs of comp I-III after [160] at 1823±50K (d).

Based on the presented results for the prediction of the liquid/austenite solidification and calculation of the nitrogen solubility in the melt, three pilot alloys designs are proposed, processed via strip-casting and further analyzed with respect to the microstructure and mechanical behavior.

4.2.3 Strip-cast alloy design

4.2.3.1 Laboratory strip-cast alloys

The target chemical compositions were designed using CALPHAD method and solubility calculations, described in the sections before. The nominal compositions of the melt and the as-cast strip material of the laboratory strip-cast pilot alloys (comp I-III) are listed in Tab. 4.2-3.

Tab. 4.2-3 Chemical compositions of the melt and as-cast strip material of the investigated pilot alloys. Recrystallization annealing conditions for the cold rolled strip material.

Composition		Chemical composition, wt.%					Heat Treatment**	SFE$_{calc}$
		Cr	Mn	Ni	C	N	(water quenched)	mJ/m²
I	**target**	**13.0**	**20.0**	**0.50**	**0.10**	**0.43 ±0.05**		
	melt	12.8	19.2	0.56	0.09	0.43		
	as-cast*	12.7	19.2	0.55	0.09	0.40	1150°C for 5 min	24.4
II	**target**	**13.0**	**22.0**	**0.50**	**0.10**	**0.48 ±0.04**		
	melt	13.0	21.4	0.59	0.10	0.47		
	as-cast*	13.1	20.9	0.60	0.10	0.44	1150°C for 10 min	25.9
III	**target**	**13.0**	**26.0**	**0.50**	**0.10**	**0.57 ±0.05**		
	melt	12.9	25.4	0.53	0.11	0.62		
	as-cast*	13.0	25.3	0.53	0.10	0.61	1150°C for 30 min	30.9

*As-cast strip material, ** Recrystallization annealing.*

The nominal compositions of the melt and as-cast strip material meet the target chemical compositions with only minor differences. The determined nitrogen content in the melt and the as-cast strip material is in agreement to the predicted nitrogen solubility values. For the high-alloyed comp III the calculated nitrogen are slightly underestimated with the applied model, though within the upper range of validity. The obtained manganese contents are slightly lower than the target value that is due to the oxidation of manganese during the melting process as the melting furnace of the laboratory strip-cast is render inert by argon but open to atmosphere. The recrystallization temperature of 1150°C was defined after annealing of the cold-rolled samples at various temperatures from 1050°C-1250°C for 5 min up to 60 min. With increase in alloying content the recrystallization time is extended to 30 min for comp III to assure a dendritic-free microstructure. The SFE was calculated between 24.4mJ/m² and 30.9 mJ/m² for comp I and comp III, respectively, which implies that the designed alloying concepts are TWIP materials.

4.2.3.2 Industrial strip-cast alloy

The industrial strip-cast alloy was produced based on the alloying concept of comp II. The nominal composition is listed in Tab. 4.2-4. The IC alloy is further referred as comp IC. The continuous recrystallization annealing after cold-rolling was performed at 1150°C for 2-5 min, while the strip-velocity was increased with length.

Tab. 4.2-4 Chemical composition and recrystallization annealing conditions after cold rolling of the investigated industrial steel grade.

Composition		Chemical composition, wt.%					Heat Treatment**	SFE$_{calc}$
		Cr	Mn	Ni	C	N	(water quenched)	mJ/m²
IC	**target**	**13.0**	**22.0**	**0.50**	**0.10**	**0.48 ±0.04**		
	melt	13.7	23.1	0.32	0.09	0.42		
	as-cast*	13.8	23.2	0.30	0.08	0.41	1150°C for 2-5 min	27.4

*As-cast strip material. ** Recrystallization annealing.*

The melting process of comp IC was performed within a converter, separately of the strip-cast line. The melt was transported in a ladle to the strip-cast plant without atmospheric control, which may lead to variations in the melting pressure, according to **Fig. 4.2-2b**. The manganese content was adjusted to 23 wt.% to increase the solute nitrogen in the melt.

4.3 Microstructure characterization

4.3.1 Laboratory strip-cast alloys

4.3.1.1 As-cast microstructure characterization

The observed as-cast microstructure is characterized by large blocks of austenitic dendrites in the columnar zone of the upper and lower strip shell. Equiaxed grains occur preferentially in the center line of the sheet where the two strips shells consolidate (**Fig. 4.3-1**). The central equiaxed zone increases with strip length and alloying content, due to a decrease in cooling rate over strip length, and reduction of thermal conductivity with higher alloying content [164], respectively.
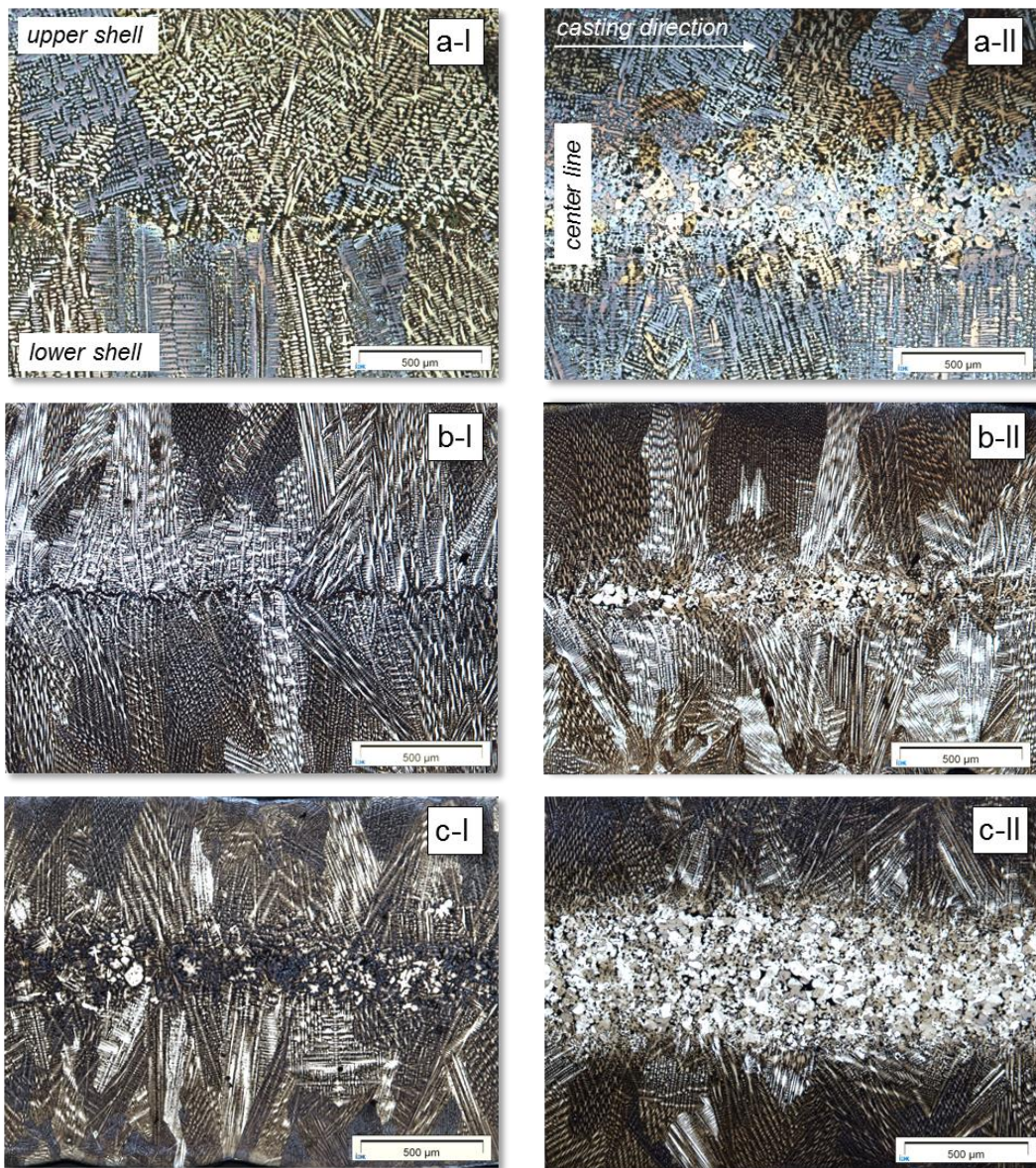

Fig. 4.3-1 As-cast microstructure at begin (I) and end (II) of the strip
for (a) comp I, (b) comp II and (c) comp III.

The secondary dendrite arm spacing, λ_2, was determined with 7.4±0.1 µm, 8.1±1.1 µm and 6.5±0.4 µm for comp I, II and III, respectively (Tab. 4.4-1), which is comparable to other strip-cast high-manganese steels [165]. The effect of the cast-microstructure, in particular the influence of λ_2, on the mechanical properties will be discussed in Chapter 4.4.1. **Fig. 4.3-2** shows the EPMA line profile of manganese, chromium and nitrogen, representative for comp II.
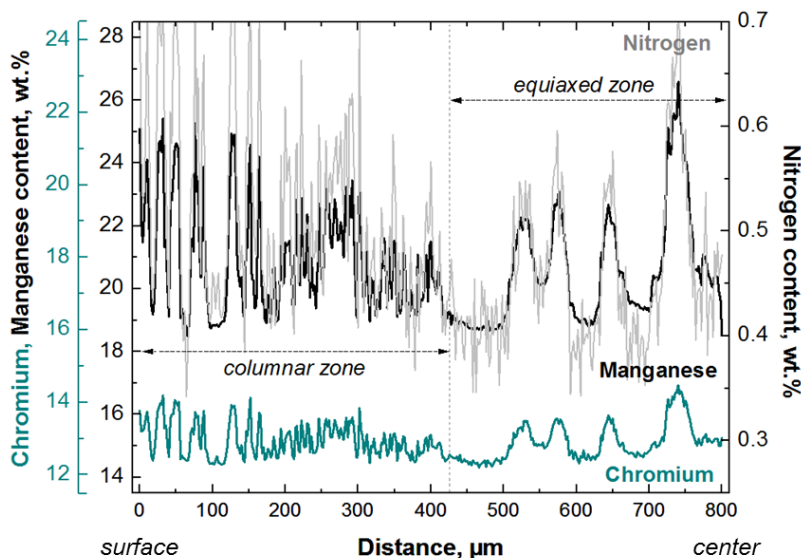

Fig. 4.3-2 EPMA line profile of the element distribution in the as-cast strip of comp II.

The dendritic microstructure in the columnar zone of the strip surface is characterized by significant microsegregations with experimental standard deviation in the manganese content of 21.0±1.7 wt.% and 0.5±0.09 wt.% nitrogen at a wavelength of approximately 4µm. The globular zone of equiaxed austenitic grains in the middle of the strip corresponds to an area of macrosegregation with increased wavelength of ~50-100 µm and slightly reduced content in manganese 20.5±1.7 wt.% and nitrogen 0.44±0.07 wt.%, which is in accordance to studies on high-manganese Fe-Mn-C strip-cast alloys [165]. The chromium content appears to be constant in the dendritic and globular zone with 13.0±0.5 wt.% and 12.9±0.5 wt.%, respectively. It is further observed that nitrogen, similar to manganese and chromium segregates in the interdendritic regions, while iron is depleted, which is in accordance to [166]. Diffusion calculations of the solidification in Fe-Cr-Mn-CN alloys by Roncery *et al.* [7], revealing the tendency for substitutional interstitial decomposition. Nitrogen exhibits high affinity to chromium and manganese rather than iron, which is due to the decreased chemical potential of nitrogen in iron [50]. As a result, nitrogen migrates toward areas of high manganese and chromium contents, which is confirmed by the matching EPMA line profiles in **Fig. 4.3-2**. The maximum deviation of the local chemical composition with 12-14wt.% chromium, 19-25wt.% manganese and 0.35-0.7 wt.% nitrogen results in a local change in SFE from 24-34 mJ/m², which is still in the TWIP range for comp II. After cold-rolling the strip material was recrystallized, resulting in a homogeneous dendrite free microstructure with an average grain size of ~46-50 µm (**Fig. 4.3-6a** and **Fig. 4.3-7a**). The cold-rolled recrystallized state is further referred as cold-rolled/RX. XRD measurements of inclusions in comp III revealed the appearance of fine distributed manganese sulfides of ~ 1 µm in size, derived from the melting process.

4.3.1.2   Deformation microstructure characterization

The microstructure phase stability of comp I-III was determined by X-ray diffraction analysis, shown in **Fig. 4.3-3** for comp I+III. Only *fcc*-austenite diffraction peaks are identified, indicating a fully austenitic microstructure of the as-cast strip and cold-rolled/RX deformed material without traces of δ-ferrite or deformation induced *hcp-/bct*-martensite to occur.
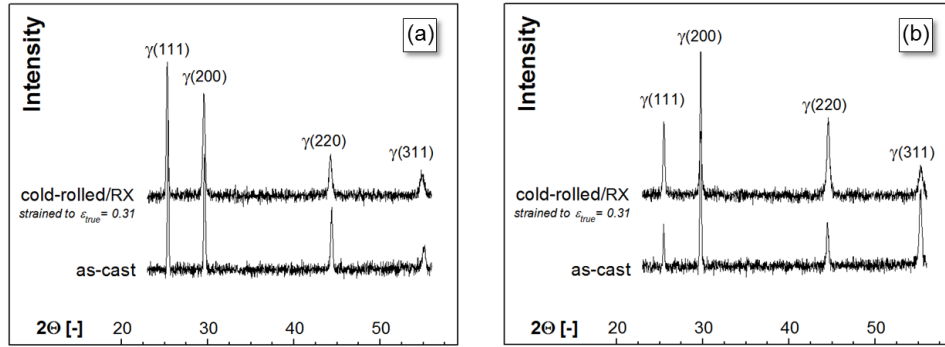
Fig. 4.3-3 1 X-ray diffractograms of the as-cast strip and deformed cold-rolled/RX samples strained to ε_{true} =0.31 at 300K of (a) comp I and (b) comp III.

Interrupted tensile tests of the as-cast and cold-rolled/RX strip material were performed to define the microstructure evolution as function of strain, in order to describe the work hardening behavior. In **Fig. 4.3-4** the *as-cast* microstructure of comp II at different tensile strain is shown.
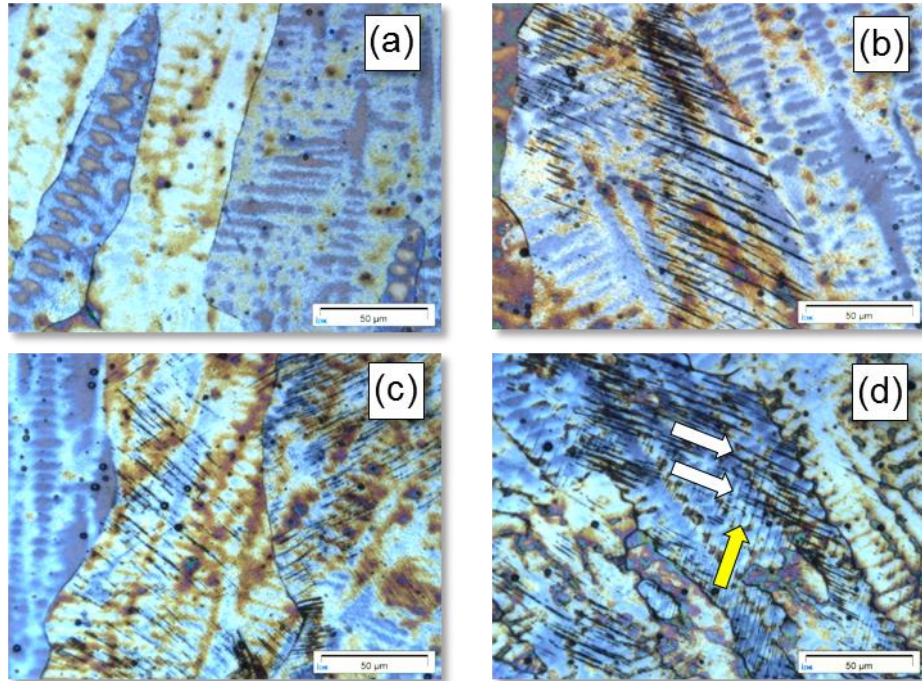
Fig. 4.3-4 Optical microscopy of the as-cast strip of comp II at different tensile strain of (a) 0.04, (b) 0.14, (c) 0.21 and (d) after fracture (cross-section).

Dark parallel lines could be observed in some grains at logarithmic strain of ε=0.14, indicating deformation markings, similar to observation by [61] in the Fe-14Cr-20Mn-0.3N alloy (**Fig. 4.3-4b**). With increase in tensile strain more grains reveal deformation markings, mainly confined to one preferred crystallographic orientation for strain up to ε=0.21. In the fracture sample, deformation markings in at least two directions could be observed (indicated by white and yellow arrows in **Fig. 4.3-4c**). The EBSD analysis was used to determine the interface character and crystallographic texture of the deformation microstructure. **Fig. 4.3-5** shows the inverse pole figure (IPF) and the image quality (IQ) maps with respect to the tensile axis of the fractured samples for the as-cast strip material of comp II. The observed deformation markings via optical microscopy are indexed as ∑3 twin boundaries (**Fig. 4.3-5a** blue colored) revealing intense mechanical twinning. The activation of two non-coplanar twin systems (e.g., an example is indicated by white and yellow arrows in **Fig. 4.3-5a**) is observed in a significant amount of grains in the fractured samples. Some grains exhibit twinning in one preferred twin system, which is assumed to primary twinning initiated in the lower stress regime at around ε=0.14. Most grains reveal orientation along the <111>//TA direction and, to a lesser extent, the <001>//TA direction [167][168]. In accordance with Schmid's, law grains with an <111>//TA orientation exhibit significantly more mechanical twins. With increased twin density, sub-boundaries developed within the grains that delimit different twin bundles, according to Barbier *et al.* [12]. As indicated by white arrows in **Fig. 4.3-5b**, these sub-grains show orientation in <001>//TA direction.
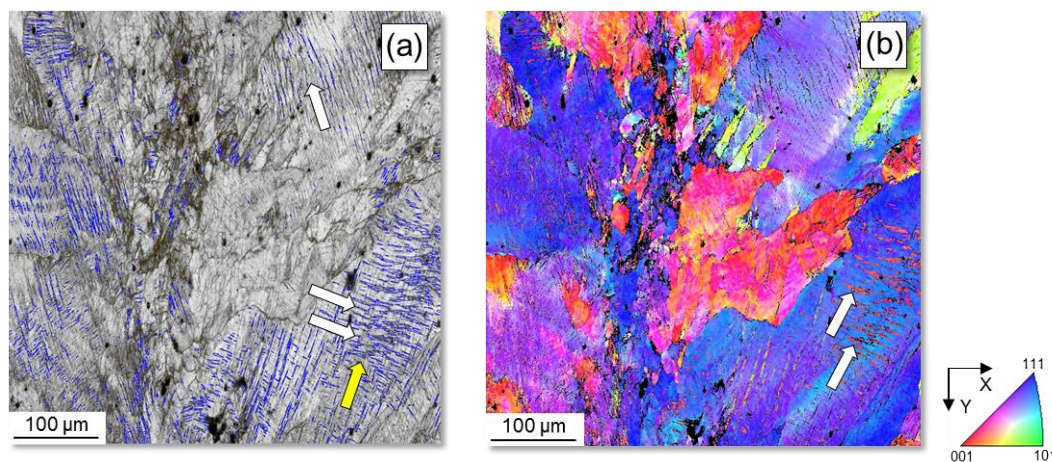
Fig. 4.3-5 (a) IQ and (b) IPF map of the *fcc* phase (blue-colored marks indicate ∑3 twin boundaries) of the as-cast strip material of comp II showing the fractured sample at RT.

One interesting result from the deformation microstructure analysis of the as-cast materials is referred to the twin evolution within the austenitic dendrites. It appears that the twins penetrate the dendrites regardless of the micro-segregation (**Fig. 4.3-4**). From **Fig. 4.3-4b** it is assumed that the deformation twins originate at the grain boundaries (**Fig. 4.3-4b)** and growth further through the austenitic dendrites until the twins reach the next grain boundary. The local change in chemical composition, which influences the local SFE to vary between 24-34 mJ/m² for comp II, seems not to affect the deformation twin growth as long as the SFE value is in the range, where TWIP is the preferred deformation mechanism.

The *cold-rolled/RX* microstructure of comp II at different tensile strain is shown in **Fig. 4.3-6** and **Fig. 4.3-7**, analyzed with optical microscopy and EBSD, respectively. Numerous annealing twins are observed in the as-received microstructure of the cold-rolled/RX material, which is possibly due to a low stacking fault energy [169] related to the enhanced Mn and N alloying [130][170]. Slip traces are visible in a few grains and within annealing twins (**Fig. 4.3-6a** white arrows), which indicates a strong orientation relation of the slip behavior in single grains relative to the tensile axis.
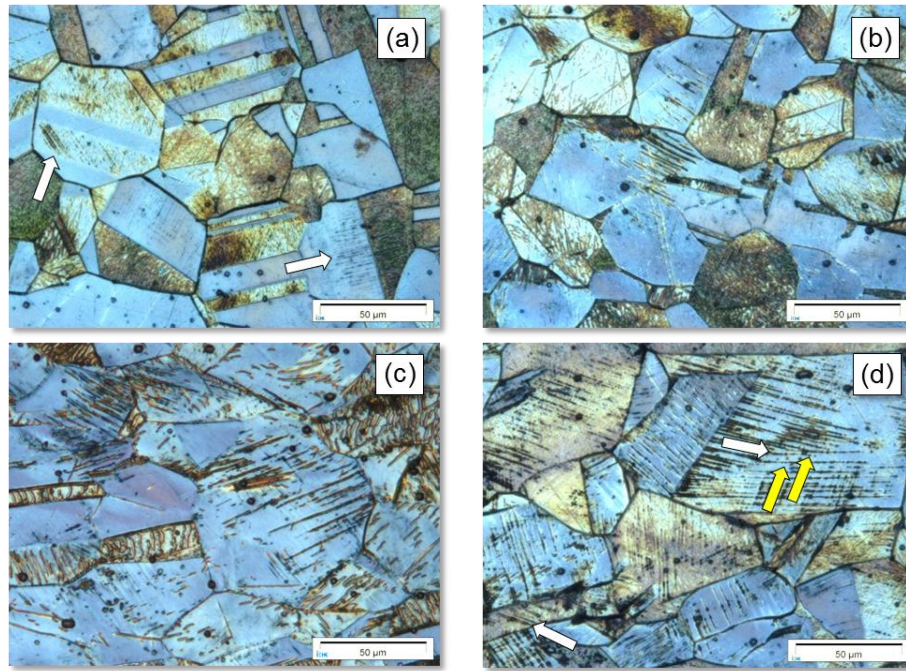
Fig. 4.3-6 Optical microscopy of cold-rolled/RX strip of comp II at different tensile strain of (a) 0.04, (b) 0.14, (c) 0.31 and (d) after fracture (cross-section).
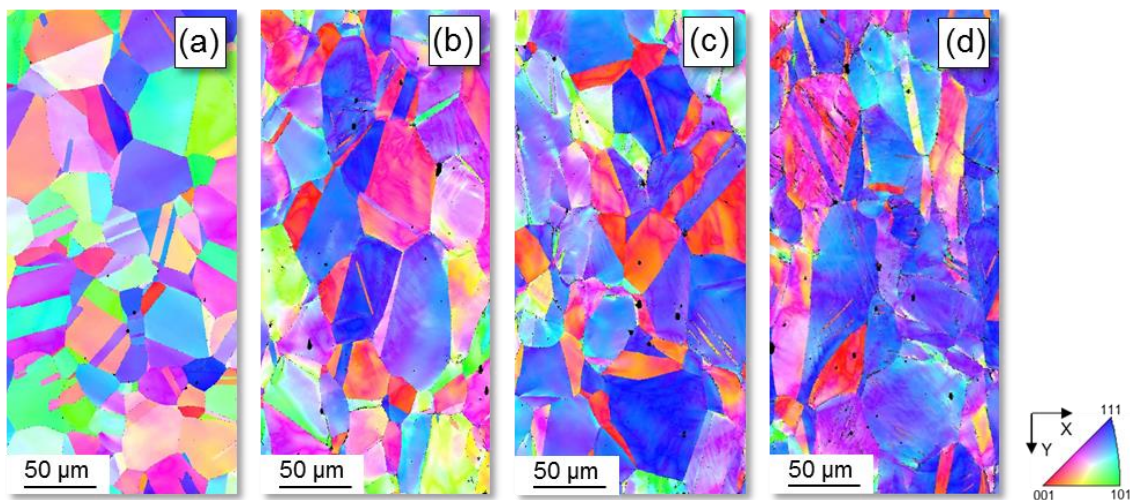
Fig. 4.3-7 (a) IPF maps (*fcc* phase) of the cold-rolled/RX strip material of comp II at different tensile strain of (a) 0.04, (b) 0.21, (c) 0.31 and (d) after fracture (longitudinal section).

Referring to [130], the deformation structures are blocked by the annealing twin boundaries (**Fig. 4.3-6a**), which are identified as coherent boundaries. At strain of 0.14 primary twinning is observed. With increasing the applied strain until fracture the amount of deformation structures increases. The observed mechanical twinning is mainly confined to one preferred twin system at strain of 0.31. As can be seen from the IPF maps in **Fig. 4.3-7**, with increasing strain, more grains show orientation between the <001>//TA and <111>//TA direction, characteristic for grains with a well-developed twin substructure of one active twinning system [13]. Analog to the as-cast fracture sample (**Fig. 4.3-5a**), the activation of two non-coplanar twin systems (indicated by white and yellow arrows in **Fig. 4.3-6d**) is identified in a significant amount of grains in the cold-rolled/RX material. The deformation microstructure evolution as function of applied tensile strain of comp II appeared to be comparable to that of comp I due to the similar chemical composition; in the as-cast and cold-rolled/RX condition (**Fig. 4.3-8a**). The fracture sample of comp II is characterized by intense mechanical twinning and the occurrence of two active twin systems, similar to comp I.
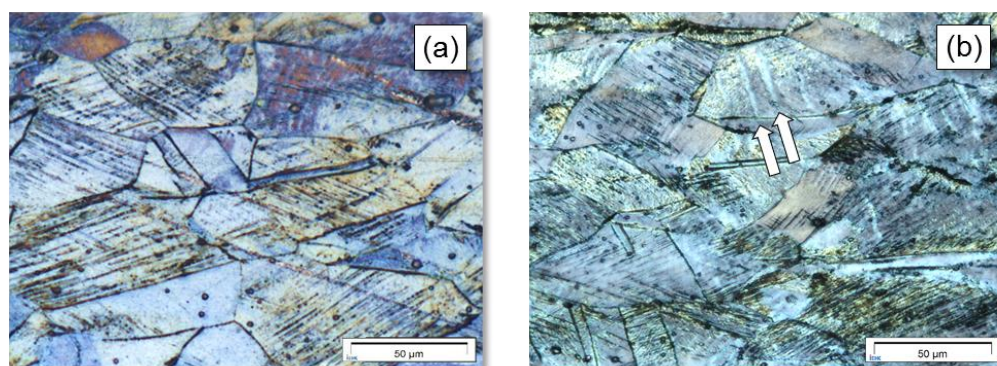
Fig. 4.3-8 Optical microscopy of tensile strained samples (after fractured) of the cold-rolled/RX strip material from (a) comp II and (b) comp III (cross-section).

With increasing the SFE to 31 mJ/m² by enhancing the alloying content of manganese and nitrogen in comp III, the onset of deformation twinning is shifted to higher strain levels. Deformation twinning is shown to originate prevalently in one twin system (**Fig. 4.3-8b**). The appearance of distinct slip traces (marked by white arrows in **Fig. 4.3-8b**) indicates pronounced dislocation slip, which is attributed to the high SFE.

4.3.2 Industrial strip-cast alloy

4.3.2.1 As-cast microstructure characterization

The as-cast microstructure of the industrial produced alloy of comp IC as obtained after in-line hot rolling is shown in **Fig. 4.3-9** at begin and end of the strip. Large blocks of austenitic dendrites are observed in the columnar zone of the upper and lower strip shell. Equiaxed grains occur in the center line. The microstructure exhibits distinct shape disorientation with grains elongated in rolling direction. Recrystallization is not observed. Variations in the as-cast microstructure at begin and end of the strip is not observed, indicating a continuous steady strip-casting process.

The recrystallization treatment after cold-rolling of the as-cast material was conducted in a continuous annealing line at 1150°C. The cold-rolled/RX microstructure is shown in **Fig. 4.3-9**.
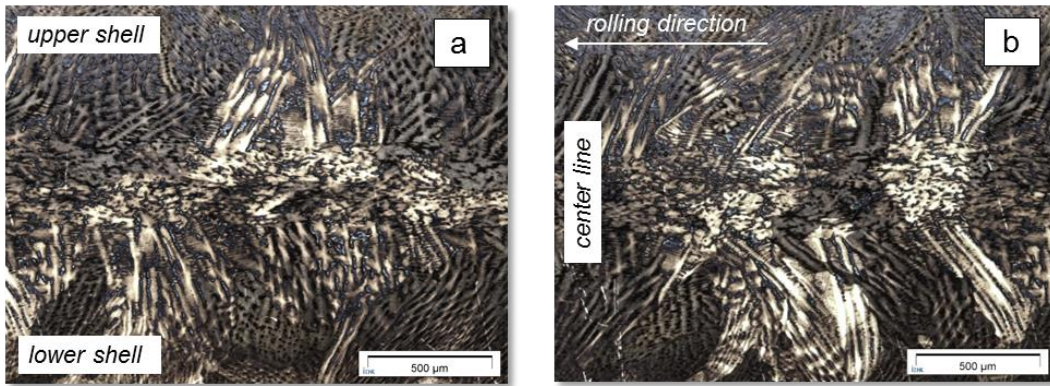
Fig. 4.3-9 Microstructure of the as-cast/hot-rolled material
at the (a) begin and (b) end of the strip of comp IC.

The microstructure of the cold-rolled/RX sheet of comp IC consists of refined globulitic grains with a mean diameter of ~20 µm and 14 µm, which is attributed to variations in the length of the recrystallization time from 2 min to 5 min, at begin (**Fig. 4.3-9a**) and end (**Fig. 4.3-9b**) of the strip, respectively. Despite recrystallization to occur, the as-cast dendritic microstructure is still present in the cold-rolled/RX sheet material (**Fig. 4.3-9b-II**). The shape of the grains indicate no disorientation related to the hot- or cold-rolling in the cold-rolled/RX microstructure.
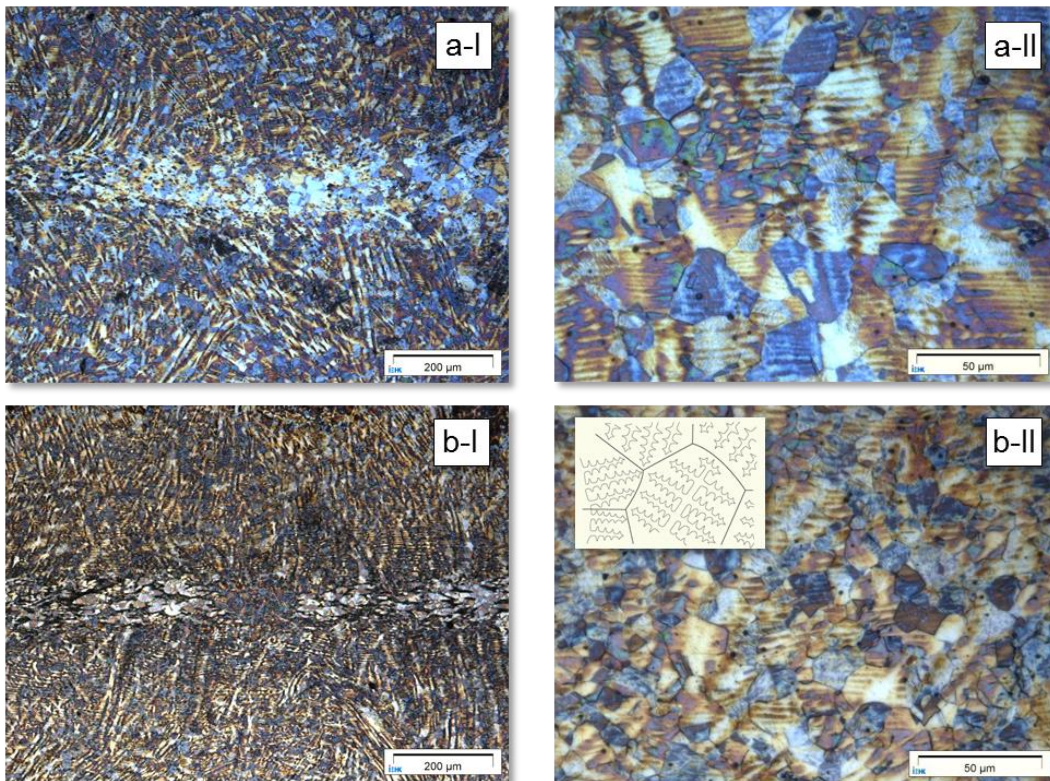
Fig. 4.3-10 Microstructure of the cold-rolled/RX strip material after recrystallization
at 1150°C for (a) 5 min and (b) 2 min of comp IC.

4.3.2.2 *Deformation microstructure characterization as function of temperature*

The deformation microstructure of the cold-rolled/RX strip material of comp IC is presented in **Fig. 4.3-11** as a function of temperature (fractured samples). Between -40°C and 45°C the highest concentration of deformation markings/structures is observed (**Fig. 4.3-11c+d**). The deformation twin fraction is lower in the sample deformed to failure at -40°C than at 45°C. Decrease in the test temperature below -40°C results in further reduction of deformation twins. Minor traces of indexed ε(*hcp*) martensite are observed at -100°C and -150°C (**Fig. 4.3-11a+b**, white arrows), mainly initiated at grain boundary triple points. Increasing the deformation temperature above 45°C results in less mechanical twining (**Fig. 4.3-11e**). At 250°C only minor mechanical twinning is observed, while some grains exhibit intense slip markings (**Fig. 4.3-11f**), indicating that at high temperatures mechanical twinning becomes progressively suppressed in favor of pure dislocation glide.
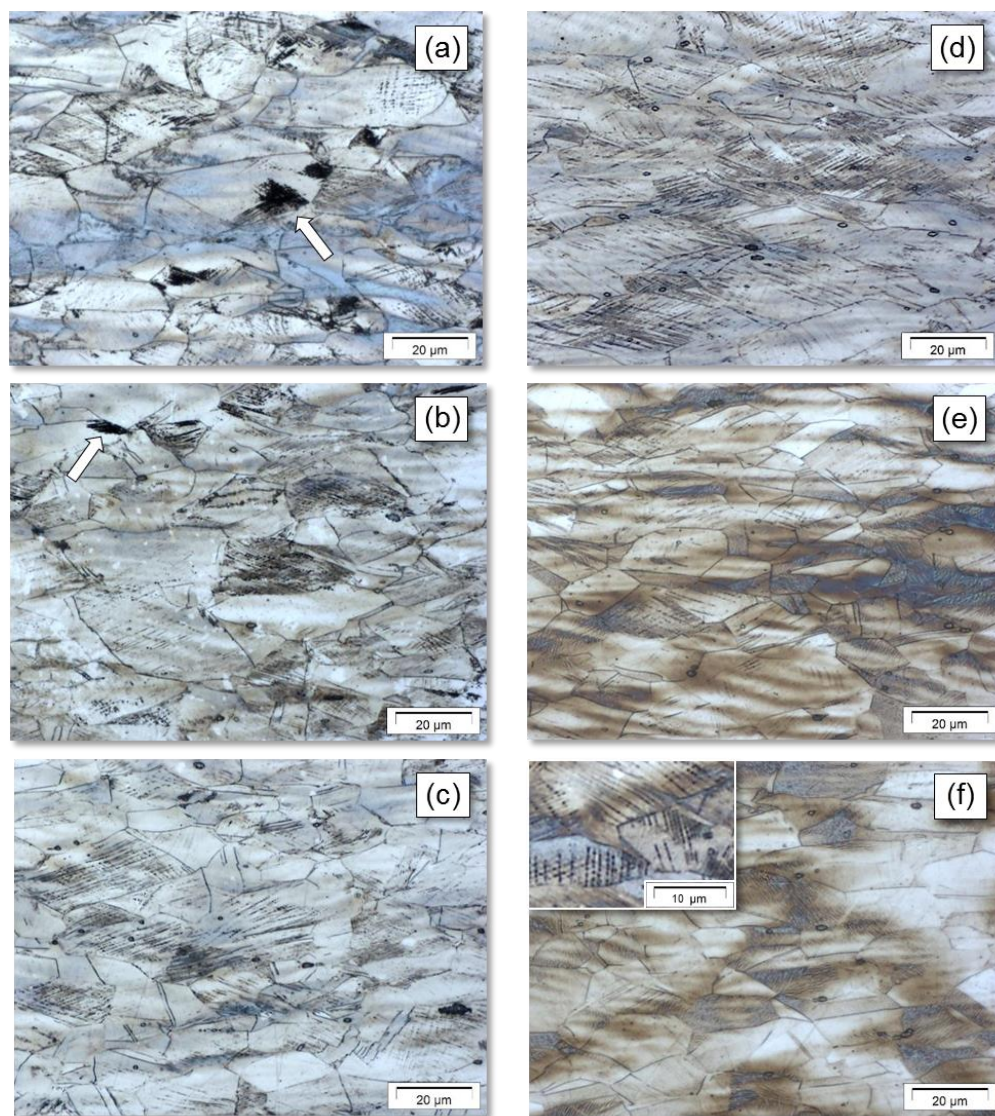
Fig. 4.3-11 Optical microscopy of the cold-rolled/RX strip of comp IC deformed at
(a) -150°C, (b) -100°C, (c) -40°C, (d) 45°C, (e) 100°C and (f) 250°C; fractured samples.

4.4 Mechanical properties and flow behavior

4.4.1 Laboratory strip-cast alloys

The mechanical properties of the as-cast and cold-rolled/RX strip material of comp I-III in comparison to conventional nickel-containing stainless steel grades are listed in Tab. 4.4-1. In the corresponding stress-strain curves and the strain hardening rates (SHR) obtained by uniaxial tensile testing are plotted in **Fig. 4.4-1**. Despite different alloying contents, only minor variations in the mechanical properties are observed between comp I-III in the as-cast condition.

Tab. 4.4-1 Mechanical properties and the secondary dendrite arm spacing, λ_2,
of the as-cast and cold-rolled/RX strip material of comp I-III.

Composition		Mechanical properties				
		YS*	UTS	UE	TE**	λ_2
	Condition	[MPa]	[MPa]	[%]	[%]	µm
I	*as-cast*	420	710	37	38	7.4±0.1
	cold-rolled/RX	540	910	50	53	
II	*as-cast*	410	680	27	28	8.1±1.1
	cold-rolled/RX	550	900	43	45	
III	*as-cast*	475	720	27	28	6.5±0.4
	cold-rolled/RX	660	1050	45	47	

* YS at 0.2% strain, ** A_{50} samples DIN 50114

Comp I+II show quite similar mechanical properties with YS of ~410 MPa and 420 MPa and UTS of 710 MPa and 680 MPa in the as-cast condition, respectively. Due to its enhanced nitrogen content of 0.61 wt.%, comp III exhibits higher YS of 475 MPa with UTS of 720 MPa. The total elongation of the strip material of comp I was measured with 38% and comp II+III with 28%. The effect of the cast-microstructure and, particularly, the influence of the secondary dendrite arm spacing λ_2 on mechanical properties have been investigated in various studies. It was found that UTS and total
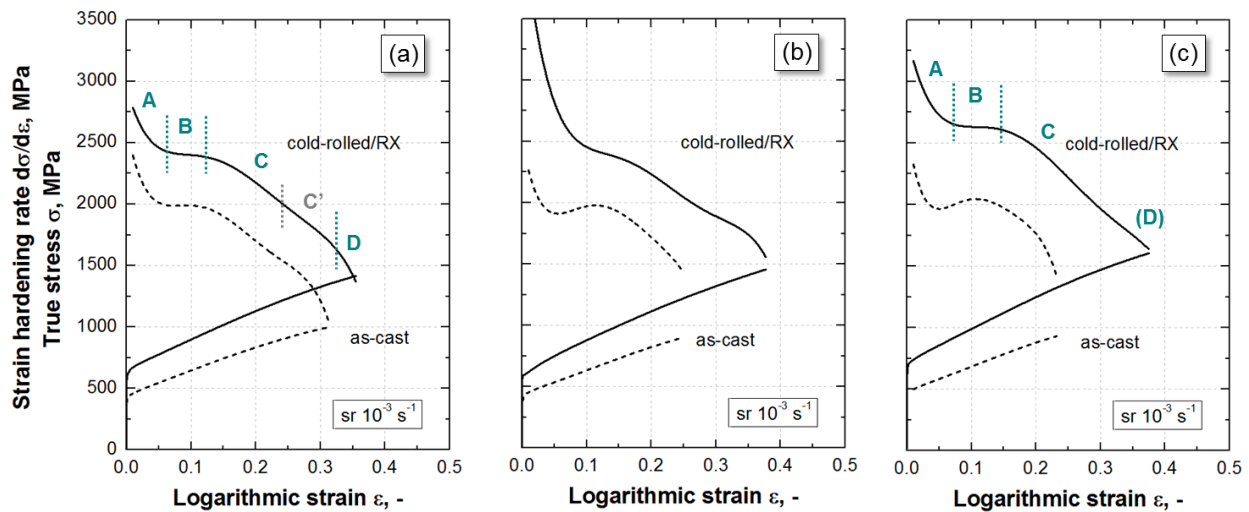
Fig. 4.4-1 True stress and strain-hardening rate vs logarithmic strain
of the as-cast and cold-rolled/RX strip of (a) comp I, (b) comp II and (c) comp III.

elongation decrease with increasing dendritic arm spacing [171], which correlates with the results for comp I-III in the current work. The low total elongation of comp III can be explained by a high amount of detected manganese-sulphides, derived from the melting process (Chapter 4.3.1.1). In the cold-rolled/RX condition the YS and UTS of comp I+II increases up to 550 MPa and 910 MPa, respectively. The YS of comp III reached ~660 MPa that is above the minimum YS of 600 MPa for automotive requirements. Stress-strain curves and the strain hardening rates, SHR (dσ/dε), for the as-cast and cold-rolled/RX strip material of comp I-III are plotted in **Fig. 4.4-1**. The SHR indicates four SH stages A-D. At around 0.05-0.1 logarithmic strain (SH stage B) the stress-strain curves feature revealing a plateau like trend. At this strain level secondary SH effects may occur, leading to the deviation from the ideal linear behavior of the flow curves [13]. The SHRs reveal a minimum at intermediate strain ~0.05 for the as-cast material that is shifted to high strain of ~0.1 for the cold-rolled/RX strip material. This stage is followed by a high SHR at higher deformations, which is more pronounced in the as-cast condition. The SHR remains nearly constant around 2000 MPa to 2500 MPa for the as-cast and cold-rolled/RX condition, respectively. Finally, the SHR rapidly drops until fracture in SH stage D, which is not clearly defined for the high alloyed comp III.

4.4.2 Industrial strip-cast alloy

The mechanical properties of the as-cast/hot-rolled and cold-rolled/RX strip material of the industrial produced comp IC are listed in Tab. 4.4-2. The mechanical properties are further determined in 0°, 45° and 90° to rolling direction (A_{30} samples) to investigate the anisotropy of the sheet material (**Fig. 4.4-2a**+**b**). Stress-strain curves and the strain hardening rates, SHR (dσ/dε), for the as-cast/hot-rolled and cold-rolled/RX (A_{50} samples) comp IC are plotted in **Fig. 4.4-2c**.

Tab. 4.4-2 Mechanical properties of the as-cast/hot-rolled and cold-rolled/RX strip material of comp IC.

Composition			Mechanical properties			
			YS^*	UTS	UE	TE^{**}
	Condition		[MPa]	[MPa]	[%]	[%]
IC	*as-cast/hot-rolled*		750	900	24	33
	cold-rolled/RX	B	510	830	46	55
		E	540	860	44	52

* YS at 0.2% strain, ** A_{50} samples DIN 50114, B/E...begin/end of strip

Comp IC reveals high YS of 750 MPa and UTS of 900 MPa in the as-cast condition, which can be explained by the induced deformation due to the inline hot-rolling step that is also reflected in the low total elongation of 33%. The mechanical properties of the strip in the cold-rolled/RX condition vary with strip length, mainly attributed to the different grain size of the RX microstructure. With strip length the grain size was determined to decrease from 20 µm to 14 µm (Chapter 4.3.2.1), resulting in increased YS, UTS and strain hardening ability (**Fig. 4.4-2c)** at the end of the strip compared to strip begin. In the as-cast/hot-rolled condition the flow and strain-hardening behavior of the strip material differs with respect to the hot-rolling direction (RD) **Fig. 4.4-2a** (values listed in Tab. 4.4-3 in Chapter 7, Appendix). The SH potential and the tensile strength decrease at 45° and 90° to RD. The cold-rolled/RX strip material reveals almost isotropic flow and strain hardening behavior (**Fig. 4.4-2b**), although after recrystallization, the cold-rolled strip shows arrears of the as-cast dendritic microstructure. It is assumed that the microsegregations within the recrystallized microstructure not affect the isotropic material behavior of the investigated strip material.
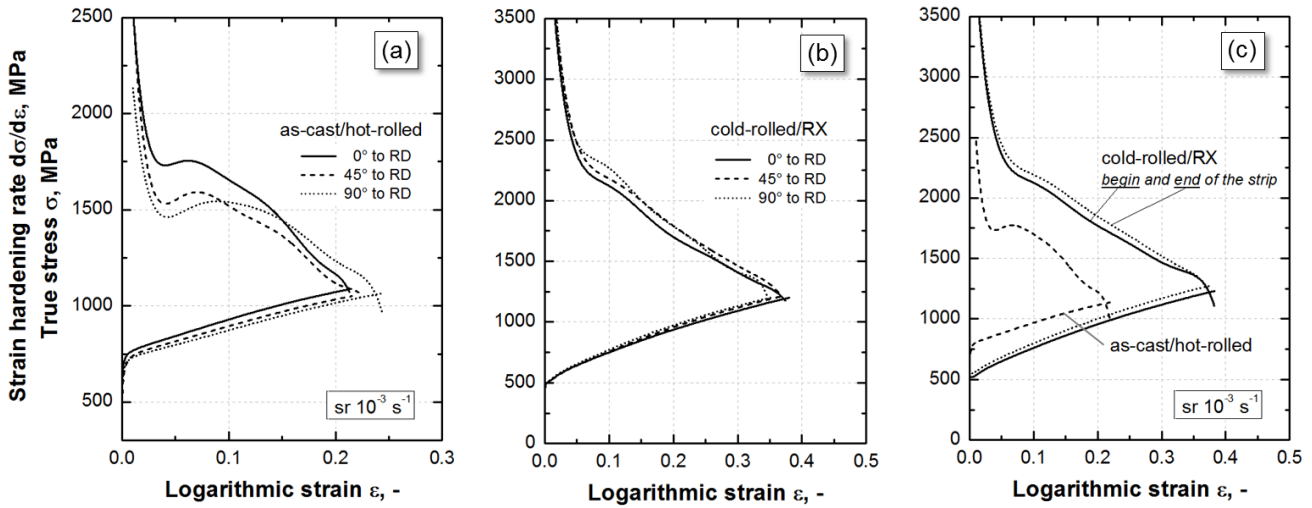
Fig. 4.4-2 True stress and strain-hardening rate vs logarithmic strain
of the (a,c) as-cast/hot-rolled and (b,c) cold-rolled/RX strip of comp IC.

Stress-strain curves and the strain hardening rates as function of deformation temperature are plotted in **Fig. 4.4-3**, for the cold-rolled/RX strip material of comp IC. Within the tested temperature range, between -150°C up to 250°C, the shape of the flow curves exhibit a parabolic trend with pronounced multistage character (indicated by different SH stages, see **Fig. 4.4-1**). The SHRs show a general drop down behavior. The slope of the SHR curves increases with temperature, more distinct at higher temperatures. Between -150°C and 45°C the SHR remains nearly identically. At temperatures of 100°C and above, a marked inflection in the SHR occurs at ~0.1 logarithmic strain that is only slightly observed in the lower temperature SHRs. Furthermore, a second inflection occurs around ~0.3 and 0.35 logarithmic strain, and the strain at which the 2nd inflection occurs increases with temperature. The SHR behavior appears to be similar to that of comp II (**Fig. 4.4-1b**).
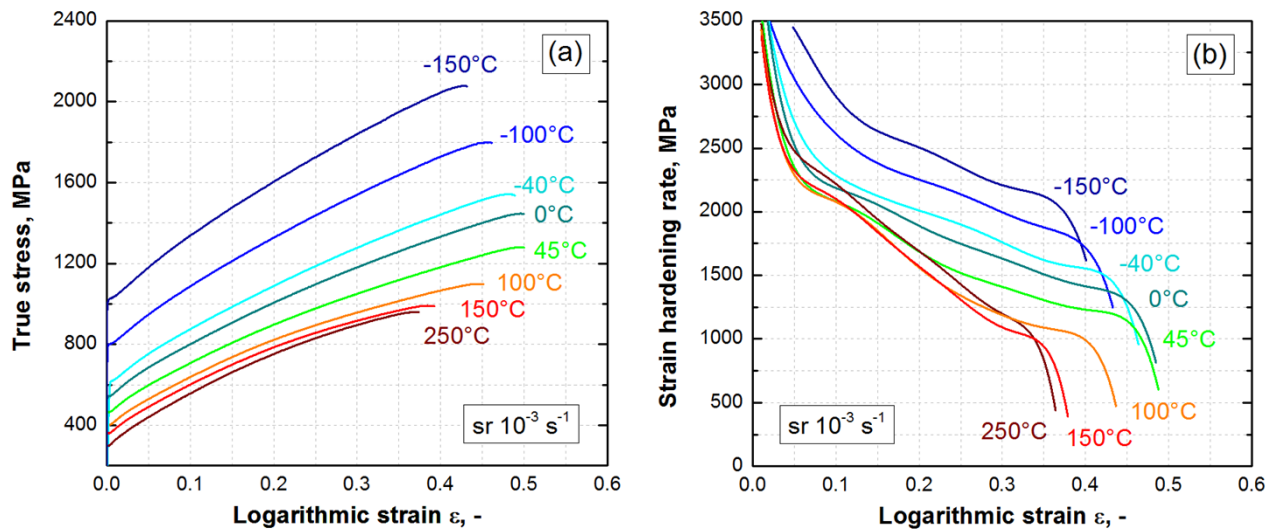
Fig. 4.4-3 True stress (a) and strain-hardening rate (b) vs logarithmic strain over
temperatures from -150 °C to 250 °C for the cold-rolled/RX strip of comp IC.

The mechanical properties are plotted as a function of temperature in **Fig. 4.4-4**. The yield strength (YS) and ultimate tensile strength (UTS) decrease with increasing temperature more severely in the low temperature regime, than at higher temperatures (>45-100°C), which may indicate a change in the active deformation mechanism [228][232]. The yield to tensile ratio (YS/UTS) decreases with increasing temperature. At 250°C the YS/UTS shows distinct drop. The maximum total elongation (TE) of ~68% occurs around room temperature (~25°C). In the temperature range from -100 to 100°C the uniform elongation is relatively constant, ranging from 63 to 68%. At high temperatures of 150°C and above, a loss of ductility to 48-50% is observed. A maximum uniform elongation (UE) of approximately 52% occurs between 0 and 45°C and decreases to about 40% with increasing temperature to 250°C. Within the tested temperature range the material reveals high post-uniform elongation from 7-16%, which indicates a high capacity of plastic deformation after uniform elongation, even at low temperatures up to -150°C.
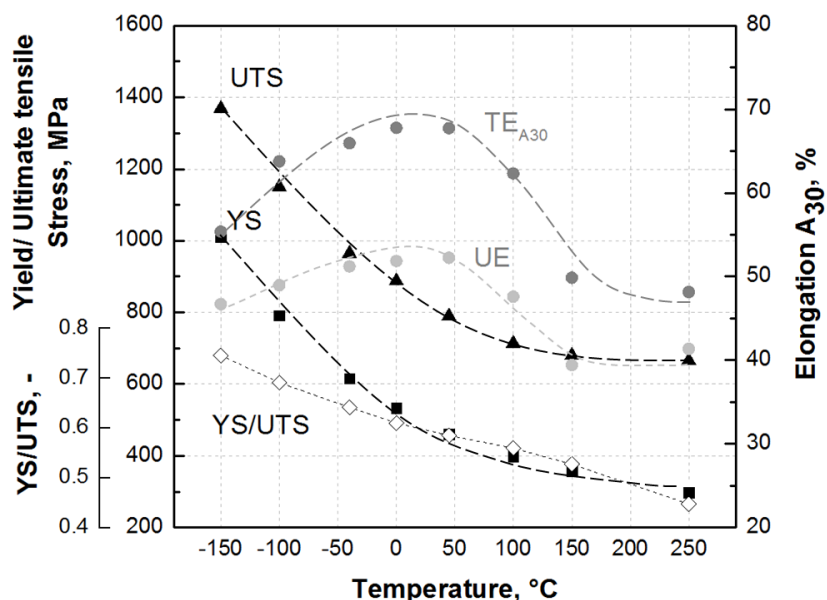
Fig. 4.4-4 Variation of tensile strength, elongation and yield to tensile ratio (YS/UTS) over temperature of comp IC.

5   Discussion

5.1   Stacking fault energy calculation of Fe-Cr-Mn-N alloys

In this section the developed model for SFE calculation in the Fe-Cr-Mn-N system will be discussed. The employed thermodynamic model for the calculation of the Gibbs free energy change, $\Delta G^{\gamma \to \varepsilon}$, described in Chapter 4.1.2, will be analyzed regarding the selected type of model, to be subregular or sublattice, at first. The re-evaluation of the thermodynamic dataset for the applied sublattice model will be evaluated, taking the composition-dependency of the driving force for the $\gamma \to \varepsilon$ phase transformation into account.

The discussion on the SFE calculation will be focused on the effect of nitrogen on SFE in the Fe-Cr-Mn-N system and how to implement the experimental findings of a non-monotonous SFE over nitrogen content into the thermodynamic SFE model. The two common methods for the SFE calculations in the Fe-Cr-Mn-N system using (1) a constant interfacial energy $\sigma^{\gamma/\varepsilon}$ and (2) including a segregation term to the $\Delta G^{\gamma \to \varepsilon}$ will be evaluated. To reproduce the effect of nitrogen on SFE over a wide range of chemical composition a composition-dependent description of the interfacial energy is proposed that successfully assigns the deformation mechanisms in austenitic stainless Fe-Cr-Mn-N steels as function of nitrogen content. Besides, the effect of temperature on SFE and the contribution of coherency strain energy to the SFE will be discussed.

5.1.1   Thermodynamic model for the calculation of $\Delta G^{\gamma \to \varepsilon}$

In order to estimate the SFE in austenitic stainless steels with different chemical compositions, various methods using computational thermodynamics assessments [20][23][79][80][81]; most latest works by Curtze *et al.* [100] and Roncery *et al.* [7][101]; quantum mechanical first-principle approaches [62][77][78], and empirical equations - as recently proposed by Lee *et al.* [60] for the Fe-Cr-Mn-CN system - based on experimental analysis after [82][83][84][85] have been investigated; in detail presented in Chapter 2.2. Using thermodynamics based models the SFE can be correlated to the microstructural phase stability and deformation mechanisms that define the active mode of the materials plasticity. A widely used approach to calculate an ideal SFE was proposed by Olsen and Cohen [95]. According to Eq. (3.12), the stacking fault is defined as ε(*hcp*) closed packed crystalline structure with a thickness of two atomic layers within the γ(*fcc*) matrix; thermodynamically described as the change of the molar Gibbs free energy $\Delta G^{\gamma \to \varepsilon}$ due to the $\gamma \to \varepsilon$ phase transformation, implying the interfacial energy $\sigma^{\gamma/\varepsilon}$ of the γ/ε interface that varies among different alloying systems between 5 and 27 mJ/m^2 [115][118]. In several works on the SFE calculation in the Fe-Mn-C system [19][59][118][156] and also on austenitic stainless steels [100], the applied thermodynamic model for the calculation of an effective Gibbs free energy of the $\gamma \to \varepsilon$ phase transformation, $\Delta G^{\gamma \to \varepsilon}$, has been defined as a subregular solid solution model with ideal entropy of mixing which assumes the elements of a system to be in a random mixing. In this model, the interstitial elements like carbon or nitrogen are considered in a substitutional solution without taking vacancies into account. As a consequence the effect of interstitial elements in the SFE calculation is described insufficient with respect to the mechanical phase stability, as illustrated in **Fig. 5.1-1** for the Fe-Mn-C system. The employed interaction parameter, $\Omega^{\varepsilon \to \gamma}$, for the calculation of the excess Gibbs free energy in the subregular model considers only the second order, binary interactions for each pair of system constituents multiplied with the relevant molar fractions. The importance of the interaction between the alloying elements in quaternary Fe-Cr-Ni-X alloys (where X = Mn, Cu, Nb) was intensively

discussed in the work by Lu *et al.* [102] using the quantum mechanical first principle method. It was found that due to the interaction of the alloying elements, the effect of each single element on the SFE can change dramatically and therefore need to be taken into account for SFE calculations using computational thermodynamics. Particularly in higher ordered systems with more than two components, applying the subregular solid solution model for the calculation of $\Delta G^{\gamma \rightarrow \varepsilon}$ can be seen as an oversimplification.
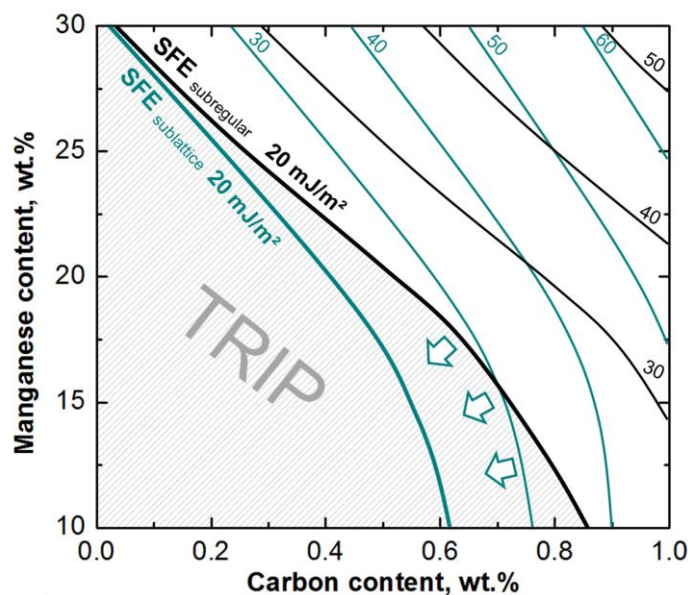
Fig. 5.1-1 Thermodynamics-based SFE mechanism map calculated according to Saeed-Akbari et *al.* [19] using the subregular model (black lines) and Djurovic et *al.* [98] using the sublattice model (blue lines) for the Fe-Mn-C system.

Hence in most CALPHAD works, a general accepted thermodynamic model that accounts the real crystalline structure is used. In the so called *sublattice model*, elements that are sufficiently different can occupy different sublattices and vacancies are treated as separate elements in the interstitial sublattice while random mixing in each sublattice is assumed [172]. The application of the sublattice model for the SFE calculation according to Eq. (3.12) is known from the works by Ferreira and Müllner [81] in the Fe-Cr-Ni system, Roncery *et al.* [7][101] for Fe-Cr-Mn-N alloys using Thermo-Calc software, Nakano and Jacques [112][115] in the Fe-Mn-C system and applied in the recent work by Pierce *et al.* [85] for Fe-Mn-(Al-Si) alloys. Above all, the Fe-Mn-C austenitic steels are one of the currently well-established austenitic high-Mn systems [173]. Besides the SFE calculations after Saeed-Akbari *et al.* [19] using the subregular model, the latest improvement of the thermodynamic parameter employing the sublattice model was proposed by Djurovic *et al.* [98] in these system. As can be seen from the corresponding SFE mechanism map in **Fig. 5.1-1,** the effect of the interstitial element carbon on the SFE and by that on the austenite phase stability strongly depends on the applied subregular or sublattice model. Using the subregular model, the effect of carbon on the *fcc* phase stability is highly underestimated in the intermediate range of manganese content. This is of main interest as in high alloyed systems the manganese content is generally reduced, which is also the case for the newly designed medium manganese steels [174].

To consider the effect of higher order interactions and the interstitial solid solution of nitrogen on the thermal and mechanical phase stability, the sublattice model is applied for the $\Delta G^{\gamma \rightarrow \varepsilon}$ calculation in the current work, rather than the simplified subregular model. In the early 90s Qui [106] adopted the sublattice model to the quaternary Fe-Cr-Mn-N system to predict the thermodynamic phase stabilities and phase-relations as function of nitrogen content. Since then no further adjustment of the model was done, even though different combinations of thermodynamic parameter and there interpretation can be found in literature. Hence, the sublattice model using the dataset after Qui [106] is re-evaluated for the Fe-Cr-Mn-N system in this work. The $\Delta G^{\gamma \rightarrow \varepsilon}$ calculation after [106] reveals a highly overestimated *fcc* phase stability particularly in low-manganese alloys. The interaction parameter between chromium and nitrogen, $L^{(fcc)}_{Cr,Fe:N}$ and $L^{(fcc)}_{Cr,Fe:N,Va}$, are adjusted to reproduce the experimental observations with respect to the *hcp* phase stability in the Fe-18Cr10Mn-N alloying system [60][73][136][138] (Chapter 4.1.2.1). The $L^{(fcc)}_{Cr,Fe:N}$ is set equal to the $L^{(hcp)}_{Cr,Fe:N}$ interaction parameter for the *hcp* phase. While the $L^{(fcc)}_{Cr,Fe:N,Va}$ is approximated to be zero. According to the employed model, manganese and nitrogen both stabilize the *fcc* phase, which in in accordance to [107][152][175]. Adding chromium to the system results in the stabilization of the *fcc* phase at low nitrogen contents [64][65], while at higher nitrogen contents, the *hcp* phase becomes more favorable. This result can be explained by the thermodynamic description of the *hcp* phase as Cr_2N nitride. The developed thermodynamic model accurately defines the upper limit of *hcp* martensite formation, across a broad range of chemical compositions (Tab. 4.1-1). However, the prediction of the available microstructural phases in the non-deformed as-received state - to be fully austenitic or partially martensitic (thermal ε- and/or α'-martensite) - is not possible since the composition-dependency of the driving force for the $\gamma \rightarrow \varepsilon$ transformation is still not clearly described in the literature. Recently Djurovic *et al.* [98] suggest an increasing effect of carbon on the driving force in Fe-Mn alloys. Lee *et al.* [176] reported an increasing driving force for $\gamma \rightarrow \varepsilon$ martensitic transformation in Fe-(14-26 wt.%)Mn alloys with increasing manganese content. While the experimental measurements of A_s and M_s-temperatures in Fe-Mn by Cotes *et al.* [96] showed no dependency of the driving force on manganese content, which is consistent with Ishida [178]. In earlier works, the driving force for $\gamma \rightarrow \varepsilon$ transformation was also found to be decreasing with the manganese content [177].

Further research is required to use the appropriate thermodynamic models and parameters as strong tools to predict and to verify the role of different alloying elements in highly alloyed systems with respect to the phase stabilities and deformation response. Defining the composition-dependency of the driving force for the $\gamma \rightarrow \varepsilon$ transformation in high-manganese austenitic steels is necessary. Particularly in higher order systems, the shortage of current thermodynamic datasets may lead to certain inconsistencies in the prediction of thermodynamic phase stabilities and the available microstructural phases before plastic deformation in more dilute solutions. As an example, in most of the reviewed steels in the current work with nitrogen contents lower than 0.1 wt.%, the Gibbs free energy, $\Delta G^{\gamma \rightarrow \varepsilon}$, was positive, which means that thermodynamically, the formation of ε-martensite was impossible, even though ε_D- or α'_D-martensite were observed in the microstructure after deformation.

5.1.2 SFE as function of chemical composition

Nitrogen is known to be a strong austenite stabilizer and suppresses the formation of α'- or ε-martensite in Fe-Cr-Mn alloys [60]. Using the developed Gibbs free energy model, the $\Delta G^{\gamma \rightarrow \varepsilon}$ increases with increase in nitrogen, as described in the section before. According to Eq. (4.1), the

SFE$_{linear}$ can be assumed to linear increase with alloying nitrogen to the system, if the interfacial energy is set as constant. However, applying this approach for the SFE calculation contradicts the experimental findings (Chapter 4.1.3, **Fig. 4.1-6**). The effect of nitrogen on SFE in in austenitic stainless steels has been extensively discussed in the literature. In **Figure 2.2-2** the dependence of SFE on the nitrogen content in different alloying systems is shown. It has been reported that nitrogen increases or decreases the SFE in various Fe-Cr-Mn and Fe-Cr-Ni steels. While a non-monotonous behavior of SFE as function of nitrogen content was described for Fe-Cr-(Ni)-Mn and Fe-Cr-Mn-C alloys with increasing carbon content up to 0.4 wt.% [60][73][76]]. Due to the inconsistent experimental results on the effect of nitrogen on SFE, no general accepted method exists for the SFE calculation in the Fe-Cr-Mn-N system that can be applied to a wide range of chemical compositions. Besides different types of models that are used, one main reason is the lack of experimental measured SFE values. Furthermore, the determined SFE values in the respective studies refer to either different domains of nitrogen contents or different alloying systems, which results in inconsistent conclusions about the effect of nitrogen on SFE. According to Gavriljuk *et al* [21] and Petrov [20][72] the effect of nitrogen in Fe-Cr-Mn alloys is not comparable with that of Fe-Cr-Ni systems due to the differences in the free electron state resulting from the Ni-N and Mn-N interactions. After Lee [179], the substitution of nickel by manganese has a major influence on the activity of chromium in austenitic stainless steels that affects not only the SFE but also the mechanical properties. The referred SFE values for the Fe-15Cr-17Mn alloying system by [20][72] with nitrogen contents between 0.06-0.88 wt.% are the only available experimentally measured values in nickel-free stainless steels with single austenitic phase microstructure that cover a wide range of nitrogen content. The reported non-monotonous SFE over nitrogen is explained by different theories. Segregation effects of nitrogen to dislocations and stacking faults [72][74], interactions of Cr-N SRO with dislocations [180][181] and the local electron density are reported to affect the SFE [48]. According to Gavriljuk *et al.* [47][48][182], the density of states at the Fermi level was defined inversely proportional to the SFE in Fe-Cr-Mn alloys [48]. In the vicinity of the nitrogen atoms, the concentration of s-electrons in *fcc* iron increases [48][182]. With increasing nitrogen content the SFE decreases as the density of states is enhanced. Due to the increased conduction electrons around the nitrogen atoms, nitrogen atoms carry an effective negative electric charge, whereas the cores of screw dislocations reveal shortage of electrons, which results in intense dislocation interactions. After [49], the interaction between nitrogen atoms and dislocations in *fcc* solid solution has both an elastic nature and a chemical nature, which is connected presumably with the formation of Suzuki atmospheres on packing defects and explains the more effective blocking of complete/or partial dislocations leading to increased SF widths. In dilute solutions, interstitial nitrogen atoms segregate to dislocations and stacking faults, decreasing the SFE [20][72]. At higher nitrogen contents, the SFE increases as the local segregation of nitrogen atoms becomes less effective [75]. In that regards, the dependency of SFE on the nitrogen content has been reported to be strongly affected by the competition between the average nitrogen concentration in the bulk and the possible amount of the segregated interstitials to the stacking faults. From the experimental point of view, it was proposed by Kim *et al.* [181] that the observed anomalously SF width for SFE may relate to the point-defect reorientation within the SFs [183], which is later also discussed with respect to the flow behavior (Chapter 5.2.1). This would assume a direct effect of point-defect complexes (Cr-N SRO) on SFE, after Fisher [180]. However, the widening of SFs by SRO reorientation occurs during deformation, where the dislocations are in a dynamic state. If the deformation load is removed, the dislocation tends to its equilibrium state. Therefore the detected SF width by TEM is likely not as result of the

SF-SRO interaction. Thermodynamic investigations by Li *et al.* [17] indicate that additional to the stabilization of the γ-phase by nitrogen, the Cr-N SRO increase the energy barrier for the γ->ε phase transition affecting the SFE. Still, more investigations are required that include the Cr-N SRO phenomena and the role of nitrogen segregation in the discussion about the SFE evaluation and interfacial energy as function of chemical composition in the Fe-Cr-Mn-N system.

Using the general approach from Eq. (3.12) to calculate an ideal SFE_{linear} the interfacial energy, $\sigma^{\gamma/\varepsilon}$, is set as a constant value giving a linear relationship between the $\Delta G^{\gamma \to \varepsilon}$ and SFE. According to Saeed-Akbari *et al.* [114] the $\sigma^{\gamma/\varepsilon}$ varies depending on different systems and studies between 5-27 mJ/m² mainly for Fe-Mn-(Al,Si)-C. For the SFE calculations in the Fe-Cr-Mn-CN system Roncery *et al.* [7] used the $\sigma^{\gamma/\varepsilon}=5$ mJ/m², which is adopted in the current work for the SFE calculation of the Fe-18Cr-10Mn alloys. While $\sigma^{\gamma/\varepsilon}=4$ mJ/m² is used to calculate the SFE in the Fe-(15-20)Cr-17Mn system. The determined SFE_{linear} values as function of nitrogen content are shown in **Fig. 4.1-6**. In comparison with the experimentally measured SFE in the Fe-15Cr-17Mn [20][21][72] and Fe-20Cr-17Mn [22] systems, the SFElinear is not representing the non-monotonous trend of SFE versus nitrogen content. Proposed by Ishida [79] and Yakubtsov *et al.* [23] a segregation term is added to the SFE calculation according to Eq. (4.2) and (4.5). In the lower range of nitrogen content, the calculated SFE_{segr} matches the experimentally SFE values, reproducing the drop of SFE due to nitrogen segregation (see **Fig. 4.1-6**). However, with increasing nitrogen contents above ~0.4 wt.%, the model deviates from the experimental results. The reason might be explained by the applied interaction energies, Λ_N, that are limited to 0.52 wt.% nitrogen content and the experimental SFE higher nitrogen contents is not properly determined (**Fig. 4.1-5**). On the other hand, the model was capable of predicting the SFE in Fe-Cr-Ni alloys [23], which is however not comparable with the Fe-Cr-Mn system, as the interaction between nitrogen and substitutional elements changes depending in the available elements as nickel or manganese [21][179][184].

In this work, a composition depend $\sigma^{\gamma/\varepsilon}$ term as function of nitrogen and manganese is introduced, Eq. (4.9). The developed model indicates a linear relation of $\sigma^{\gamma/\varepsilon}$ as function of manganese, while a non-monotonic effect of nitrogen on $\sigma^{\gamma/\varepsilon}$ is defined, reflecting the influence of nitrogen segregation on SFE. Using a modified embedded-atom method, Kim *et al.* [137] explain the drop in the $\sigma^{\gamma/\varepsilon}$ curve as the result of manganese segregation to the stacking faults in Fe-(10-20 wt.%)Mn alloys. The segregation of manganese to twin boundaries in the Fe-28Mn-0.3C steel was recently investigated using atom probe tomography [185]. According to Herbig *et al.* [185] no evidence for the segregation of manganese (or carbon) at deformation twin boundaries were found; which is attributed to the lack of diffusivity of the solutes at room temperature. Therefore, the non-monotonic behavior of $\sigma^{\gamma/\varepsilon}$ as function of manganese in binary Fe-Mn alloys is probably a result of the applied thermodynamic model for the calculation of $\Delta G^{\gamma \to \varepsilon}$ within the SFE model, which is in accordance to Pierce *et al.* [85]; but can be also related to the experimental observed SFE values, used to obtain a composition dependent $\sigma^{\gamma/\varepsilon}$. The effect of chromium on interfacial energy is not yet clearly described due to the lack of experimental data. Nevertheless, since chromium exhibits strong interaction with nitrogen leading to the occurrence of Cr-N short range ordering, the future works must include this element in the model development. It can be assumed that due to the formation of Cr-N SRO, the segregation effect of nitrogen is influenced, in a way that as more nitrogen atoms are bonded in the short range ordered zones as less "free" nitrogen atoms are left to segregate to SFs, that will influence the SFE. Besides, the random distribution of chromium in the lattice that was previously reported not to be affected by nitrogen in the iron-matrix [16], as well as the interaction of chromium

with other substitutional elements like manganese, may have a major impact on $\sigma^{\gamma/\varepsilon}$. In addition, the ongoing *ab-initio* calculations could be used to support the understanding of the composition-dependency of the interfacial energy in various systems.

The developed SFE model successfully assigns the activation of deformation induced twinning in Fe-Cr-Mn-N stainless steels. The transition between the activation of TRIP and TWIP mechanism is defined at 17±0.5 mJ/m², which is similar to 18 mJ/m² after Allain *et al.* [156] in Fe-22Mn-0.6C and 15 mJ/m² by Rémy [118] in Fe-5Cr-20Mn-0.5C steels. The influence of Cr on the SFE is small, and typically within +/- 1 mJ m^{-2} per wt.% depending on alloy composition, which is in accordance to experimental [25] and empirical SFE investigations of austenitic steels [2]. At lower contents, chromium increases the SFE while at higher chromium contents the SFE decreases, which is in agreement with experimental results in Fe-18Mn-5.6Cr-0.25C [65] for Cr < 10 wt.% and in Fe-Cr-Ni [80] alloys. Nevertheless, there are diverse discussions in the literature concerning the effect of chromium on SFE. According to Ferreira and Müller [81] the SFE faces a minimum with increasing chromium in the Fe-Ni system, which confirms other studies in the same system by Rhode and Thompson [186] with the minimum to occur at 20 wt.% chromium. Other results describe a decreasing effect of chromium (up to 10 wt.%) on SFE in Fe-22Mn-0.6C [59] or Fe-Cr-Ni [77][187]. Dai *et al.* [82] reported that the addition of chromium (or manganese) in small amounts will raise the SFE in carbon steels. Further research is required to confirm any of the latest results regarding the effect of chromium on SFE, especially with a focus on different alloying systems. After Lee [179] the chromium activity in austenitic stainless steels is reduced by manganese comparing to nickel containing alloys, which influences the SFE in these systems. At the moment the model validity can be set to the following range of chemical compositions: nitrogen 0.23-1.0 wt.%, chromium 0-25 wt.%, and manganese 5-30 wt.%. It is noted that the developed SFE model including a composition dependent description of the interfacial energy term very well predicts the SFE for the Fe-Cr-Mn-N system in the given range of validity. However, a direct application is restricted in terms of other systems. From the theoretical results, using quantum mechanical first principles methods, [77] identified the three fundamental terms: the electronic, volume and magnetic contribution, to affect the SFE. The balance between these terms strongly dependents on differences in the alloying system, as the same alloying element can cause totally opposite changes in the SFE of alloys with different host composition.

In order to investigate the influence of the coherency strain energy E_{strain} on the SFE, a constant E_{strain} = 40 J/mol after [95][96] was included to the model calculation, Eq. (4.10). After [95] the coherency strain energy contribution to the fault energy arises from the additional strains which are necessary to complete the *fcc* to *hcp* transformation. The strain energy contribution is considered as the sum of a dilatational or volume contribution and the shear contribution from the partial dislocations [96]. Considering the coherency strain energy, E_{strain}, a shift in the calculated SFE$_{effective}$ relative to the SFE$_{comp}$ values is observed, that is more dominant in the TWIP region, than in the TRIP region (**Fig. 4.3-10**). This result is explained by the change in the description of the $\sigma^{\gamma/\varepsilon}_{comp}$ over manganese from 0.7 to 0.8 in Eq. (4.9), as can be seen from **Fig. 4.1-8b**. The effect of manganese on $\sigma^{\gamma/\varepsilon}_{comp}$ becomes more significant if E_{strain} is considered. These findings are in agreement to [95]. After Olsen and Cohen [95], $\Delta G^{\gamma \rightarrow \varepsilon}$ and E_{strain} refer to the bulk properties and are independent of the stacking fault size. Thus, all differences between the bulk and stacking fault properties are included in the surface energy. After Cotes *et al.* [96], E_{strain} is weakly dependent upon composition, for Fe-Mn alloys with up to 28 wt.% manganese. In the latest work by Pierce *et al.* [85], $2\rho E_{strain}$ was found to increases

from 5.4 mJ/m² to 6.4 mJ/m² with increase in manganese from 15-25wt.% in Fe-Mn alloys; more distinct from 1.4-3.6 mJ/m² in Fe-Mn-3Al-3Si alloys with manganese increase from 22-28 wt.%. Assuming a constant coherency strain energy is therefore an oversimplification and the effect of chemical composition in Fe-Cr-Mn-N alloys needs to be taken into account. The coherency strain energy, and especially the shear contribution, is assumed to further play a major role in the validation of SFE model calculations with experimental measured SFE values. Recent analysis of the impact of nanodiffusion on the SFE in Fe-Mn-C alloys combining *ab initio* calculations with *in situ* transmission electron microscopy analysis have been shown, that the measured SFE by TEM is strongly dependent on the applied experimental conditions [26]. The temperature induced outward diffusion (depletion) of carbon from the SFs during measurement is discussed to cause the change in SFE, but may also attribute a change in the interfacial energy.

In the last years particular interest evolves about carbon alloyed Fe-Cr-Mn-CN alloys [7][48][73] [135][188], that exhibit an exceptional combination of strength and ductility and show great promise for structural applications, due to the synergistic effect of C+N alloying [76]. The development of carbon-nitrogen di-interstitial [189] thermodynamic model combining the Fe-Cr-Mn-N and Fe-Cr-Mn-C systems is proposed as one aim of future research [73]. The basic approach will be to use the reported assessment of the Fe-C-N system by Herzmann [190] and Du and Hillert [191] which was later re-evaluated by Du [192], where the carbon-nitrogen interaction are considered in the ternary parameter $L^{\Phi}_{Fe:C,N}$ for the *hcp* and *fcc* phases. The thermodynamic description of the *hcp* phase depending on carbon and nitrogen has to be validated delicately, since the solubility of each interstitial element in the *hcp* phase is essentially different [193]. For the development of a thermodynamic based SFE model for the Fe-Cr-Mn-CN system the effect of di-interstitial carbon and nitrogen alloying on the $\sigma^{\gamma/\varepsilon}$ and E_{strain} is of mayor importance. Lee *et al.* [73] proposed an empirical relation of SFE depending on C+N content and C/N ratio. It is revealed that the relative increase in SFE due to addition of C is larger than compared to N, while referring to a study by Reed and Austin [194]. However, further research is required to understand the metal physics phenomena that define the linear increase of SFE in Fe-Cr-Mn alloys with carbon and nitrogen alloying, although the effect of alloying with only nitrogen is non-monotonous.

5.1.3   Effect of temperature on SFE

The SFE is strongly influenced by temperature [85]. The SFE increases with temperature causing a change in the active deformation mechanisms from: 1) dislocation glide and $\varepsilon_D(hcp)$ martensite to 2) dislocation glide and mechanical twinning to 3) pure dislocation glide. In the current work, the suppression of $\varepsilon_D(hcp)$ martensite is observed above SFE of 17 ± 0.5 mJ/m². At SFE values >40 mJ/m², mechanical twinning gets progressively suppressed and dislocation glide becomes the dominant deformation mechanism [85][90][195]. However a strict division between the SFE values in the transition regions is not yet clear and often depends on the investigated alloying system. **Fig. 5.1-2** represents the change of SFE with temperature determined by thermodynamic calculations [114][156] and experimental observations [118][156][196], with respect to the calculated SFE of 27 mJ/m² for the investigated alloy comp IC at RT and the observed deformation microstructures with LOM at various temperatures (**Fig. 4.3-11**). At T>RT the linear temperature coefficient of 0.1 mJ/m²K [196] is found convenient to reproduce the temperature dependent SFE, as the SFE would be overestimated by the thermodynamic calculations. In the applied thermodynamic subregular models [118][156] the interstitial elements are considered to be in a substitutional solution without taking vacancies into account. Consequently, the effect of interstitial elements on the SFE is

insufficiently described [58]. The SFE increases from 27 mJ/m^2 at RT, calculated with the employed SFE model, to 49.5 mJ/m^2 at 250°C after [196]. The determined SFE of ~50 mJ/m² is related to the range where dislocation glide is the dominant deformation mechanism, correlating the deformation microstructure with nearly no deformation twinning observed at 250°C (**Fig. 4.3-11f**). However, at T<RT the SFE over temperature follows the thermodynamic based model calculations by Saeed-Akbari *et al.* [114], that consider the contribution of magnetic ordering. Despite minor islands of ε(*hcp*)-martensite in the low temperature samples (**Fig. 4.3-11a+b**), that can be explained by local differences in the chemical composition, mechanical twinning is the only type of secondary deformation mechanism observed until -150°C, and the SFE is assumed to be ~19 mJ/m². According to the present results, mechanical twinning is the dominant secondary deformation mechanism over the tested temperature range of -150°C up to 250°C. Deformation induced ε(*hcp*)- and α$'$(*bcc*)-martensite formation is not observed for the Fe-14Cr-23Mn-0.4N alloy of comp IC, which implies that the transition temperature $T_0^{\gamma \rightarrow \varepsilon}$ is below -150°C.
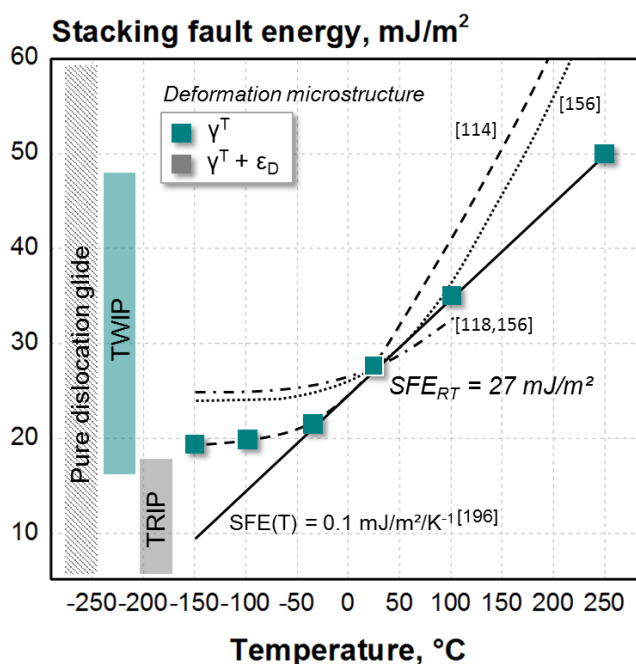
Fig. 5.1-2 SFE as function of temperature after calculations for Fe-22Mn-0.6 [114][156], Fe-5Cr-20Mn-0.5C [118][156] and type 304 stainless steel [196] with respect to the deformation microstructure of comp IC determined with LOM.

As an intrinsic materials property, the SFE gives the ability of a material to deform by TWIP, TRIP and/or pure dislocation glide. Hence, the SFE is a widely used parameter to define the activation or suppression of deformation induced mechanisms as mechanical twinning or strain induced martensite formation for various systems. However, the evolution of deformation mechanisms in austenitic steel is also influenced by factors other than the SFE. The crystallographic orientation [13], dislocation density [195] and dislocation-solute interactions [24] are further relevant microstructure parameters that play a major role in the critical stress for mechanical twinning and the control of the dislocation dynamics.

5.2 Flow behavior and strain hardening

5.2.1 Flow behavior

The stress-strain curves of the investigated Fe-Cr-Mn-N alloys exhibit a homogenous flow behavior at room temperature and over the tested temperature range at strain rate of 10^{-3} s^{-1} and no periodic serrations have been detected in the flow curves. The phenomena of serrated yielding or jerky flow is described in the literature as macroscopic evidence of dynamic strain aging (DSA), known to occur in high manganese TWIP steels containing solute carbon [52][183][197][198]. The serrated yielding is characterized by the formation and motion of localized deformation bands (Portevin Le-Chatelier phenomena) during plastic deformation [198]. From a technological point of view, the non-homogeneous plastic flow may lead to surface defects on formed parts during sheet forming processes, which makes it disadvantageous for the quality of sheet products [197]. Proposed by Lee *et al.* [199], the DSA arises from interactions between stacking faults (SF) and local ordered C-Mn SRO complexes in austenitic Fe-Mn-C steels by braking away of SF and dislocations from the point-defects, which requires higher stresses. In the presence of C-Mn complexes, the dislocation movement not only requires additional force to pass the local ordered zone, but also causes a disordering effect of the C-Mn complexes, which may occur by a single diffusive jump of C atoms [183]. In low-SFE material with wider SF the reorientation of C-Mn complexes within the SF region is favored and occurs before the SF is removed by the trailing partial (dislocation waiting time [200]), leading to higher stresses for reinitiating of the dislocation glide, enhancing the DSA mechanism [183]. The DSA however is reduced in high-manganese TWIP steels containing aluminum (see **Fig. 5.2-2**), which decreases the carbon activity [52], increases the activation energy for reorientation of the C-Mn point defects [183][201], and results in smaller SF widths due to the increasing effect on SFE. Still there is an ongoing discussion about the effect of nitrogen on DSA. The addition of nitrogen was reported to increase the critical strain for the onset of serrations or even suppress the serrated yielding in Fe-Cr-Ni-Mo [24][200][202][203][204][105], Fe-Mn-C [197][199][205][206] and Fe-Cr-Mn-C [76][201] systems. The addition of 0.09 wt.% nitrogen to the Fe-18Mn-0.6C alloy was reported by [199] to decrease the SF width with increase in SFE, reducing the probability that the C-Mn complexes can reorient before the SF is removed by the trailing partial, which delays the onset of DSA. According to Bracke [206], nitrogen atoms interfere with point-defect complexes involving interstitial C, reducing the formation of Mn-C dipoles and limiting them as a possible source of DSA. The finding suggest that the critical strain for DSA is related to both, the SF width and the type of SRO complexes [181][183][199]. In Cr-N steels the strong affinity between chromium and nitrogen atoms result in the formation of local Cr-N SRO as extensively discussed in literature [14][15][16]. The interatomic attraction (I) of interstitial nitrogen and carbon to manganese and chromium-substitutes have been calculated by Xie *et al.* [207] to be $I_{Cr-N} > I_{Mn-N} > I_{Cr-C} > I_{Mn-C}$, with the attraction of Cr-N and Mn-N significantly greater than the Cr-C and Mn-C. In nitrogen alloyed Fe-Cr-Mn and Fe-Cr-Mn-C steels, Cr-N SRO is assumed to be the preferred ordered structure [208] rather than Mn-C SRO [209][210]. To justify the occurrence of Cr-N SRO under the present annealing conditions (Chapter 4.2.3) the following assumption have been made. According to [Kha78], SRO parameters are proportional to the pair-site probabilities. With this, the problem of SRO kinetics is reduced to the solution of kinetic equations for a pair-site probability, and further to the simple problem of usual discrete diffusion of an atom in an external field formed by a fixed atom. SRO in Ni-Cr austenitic steels [208] and HMnS [212] have been successfully calculated by the McLellan's model [213] where substitutional atoms are assumed to be randomly distributed while

interstitials jump (short range jump) to the energetically favorable interstices. Therefore, N diffusion is the crucial factor to achieve such ordering. For the given recrystallization annealing conditions for comp I-III and comp IC at 1150°C for 2-30 min, the calculated characteristic diffusion length of N = 80-326 μm, by using the diffusion coefficient of N in *fcc* iron from [214]; which is sufficient for N to generate such ordering. Experimental evidence of Cr-N SRO arises from Oda *et al.* [14] using X-ray absorption fine structure analysis of the austenitic Fe-1.5Mn-15Cr-15Ni alloy and, more recently, Li *et al.* [17] applying the atom probe tomography method to analyze Cr-N SRO in the Co-29Cr-6Mo-(0.1-0.16)N alloy. According to [14], during plastic deformation interstitial nitrogen breaks away from the Cr-N SRO complexes that form around chromium atoms in the solution treated condition of Fe-Cr-Mn alloys, which is similar to the assumptions by [183] and others on Mn-C SRO in Fe-Mn-C steels. One main difference in the interaction between dislocations and SF with Cr-N or Mn-C SRO complexes is proposed to be related to the activation energy for reorientation of the point defects, in order to generate serrated yielding. The activation energy for stress induced reorientation of Mn-C SRO is 1.02 eV, which is about half the value of the activation energy for carbon diffusion in *fcc* iron [215]. Experimental measured activation energy for Cr-N reorientation is not available in the literature. However, it can be assumed that the activation energy for Cr-N reorientation is much higher than for Mn-C. Furthermore, chromium additions, which significantly reduce the diffusivity of carbon in austenite [216], may also increase the activation energy of reorientation of the point defect complexes, similar to the effect of aluminum [201]. Thus, the type of SRO and the activation energy for reorientation of the point defects, rather than the SFE may be the reason for the homogenous flow behavior of the investigated Fe-Cr-Mn-N alloys.

5.2.2 Strain hardening as function of strain

The strain hardening rates, SHR, of the as-cast and cold-rolled/RX strip material show differences in the level and shape of the SH curve for all the investigated alloys (**Fig. 4.4-1**). While the SHR of the cold-rolled/RX strip reveals a general drop down behavior, a slightly concave shape of the SHR is observed for the as-cast strip material with an inflection to occur at around 0.05 strain. Characteristics in the SH behavior with respect to the as-cast and cold-rolled/RX condition of the same alloy can be attributed to the change in grain size (from >100 μm to 50 μm, respectively), differences in the density and distribution of the deformation induced dislocation substructure and the critical stress for the onset of deformation twinning. The latter are strongly influenced by the local chemical composition. According to Wang *et al.* [40] the critical resolved shear stress for the activation of deformation twinning increases with dislocation density and decreases with grain size. The grain refinement in the cold-rolled/RX material may have led to an increase in the twinning critical resolved shear stress. This results in retarded generation of deformation twinning, that is macroscopically reflected in the drop down behavior of the SHR. As can be seen from the LOM (**Fig. 4.3-6d**) and EBSD (**Fig. 4.3-7d**) analysis, intensive deformation twinning is not observed until fracture. In contrast the SHR of the as-cast strip materials reveals a minimum at 0.05 strain. After Gutierrez *et al.* [13], the SH in the intermediate strain regime (0.05-0.12 logarithmic strain) can be quantified in terms of the dislocation mean free path. The refinement in the dislocation mean free path occurs due to the formation of a well-defined deformation twin substructure, described for high-manganese Fe-Mn-C TWIP steels [13]. In the cast-microstructure the dendritic microsegregations within the austenitic grains are believed to act as additional phase boundaries besides the twin substructure, leading to a more effective reduction in the dislocation mean free path. The kernel average misorientation (KAM) maps of the as-cast and cold-rolled/RX strip material of comp II after a logarithmic strain of 0.14 are shown in **Fig. 5.2-1**.
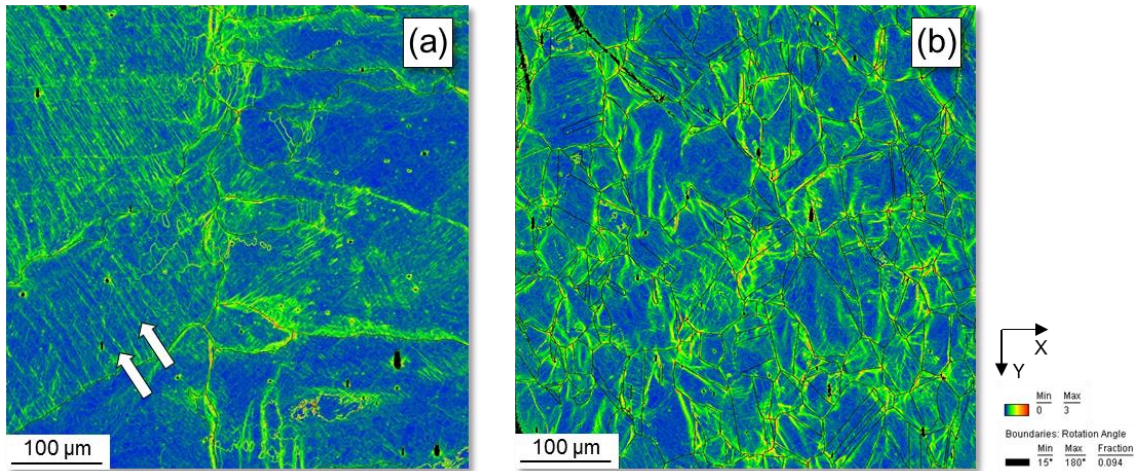
Fig. 5.2-1 KAM maps of the (a) as-cast and (b) cold-rolled/RX strip material of comp II showing the samples deformed to 0.14 strain at RT.

Intensive lattice distortions, related to high dislocation densities, are observed at the grain boundaries in the as-cast and cold-rolled strip. Thought, in the as-cast strip distinct local lattice misorientation are also evident within the austenitic grains, likely in between the dendrites (**Fig. 5.2-1a**, indicated by white arrow). The dislocation substructures that develop in the interdendritic spacing are assumed to act as strong barriers to the dislocation glide and deformation twin growth that, besides the grain size effect, defines the differences in the level and characteristics of the SHR between the as-cast and cold-rolled/RX material. One interesting feature is observed for the twin evolution in the as-cast material. As observed from the deformation microstructure analysis (e.g. for comp II, **Fig. 4.3-4**), the deformation twins originate at the grain boundaries and growth further until they reach the next grain boundary, thereby penetrating the dendrites regardless of the microsegregation. The local change in chemical composition, which influences the local SFE to vary between 24-34 mJ/m² of comp II, seems to not affect the deformation twin growth as long as the SFE value is in the range, where TWIP is the preferred deformation mechanism. Besides grain boundaries, areas of low-SFE are assumed to act as potential twin nucleation sites, since the interdendritic regions reveal high local dislocation density (**Fig. 5.2-1a**).

The SHR of the cold-rolled/RX materials of comp I-III will be discussed in the following in more detail. The SHRs as function of strain at 300K are plotted in **Fig. 4.4-1**, showing four SH-stages. The initial stage A hardening is characterized by a sharp drop of the SHR until strain~0.05. Within stage B the SHR is nearly constant, revealing a plateau like trend. Then the SHR steadily decreases in stage C until stage D, where the SHR rapidly drops until fracture (**Fig. 4.4-1a**). The strain-hardening (SH) behavior of the investigated Fe-Cr-Mn-N alloys is characterized by a multistage intermediate hardening, associated with general high SH (**Fig. 4.4-1** and **Fig. 4.4-2**). The SHR of the low-nitrogen alloys of comp I and II indicates four SH stages, while the SHR of the high alloyed comp III reveals mainly three distinct SH stages (see **Fig. 4.4-1**). The initial stage A hardening is mainly controlled by dynamic recovery of dislocations and the formation of SFs [9][48], characterized by a sharp drop of the SHR. No mechanical twins are detected by EBSD (**Fig. 4.3-7a**). Parallel slip traces are observed that can be indicated as macroscopic evidence for planar glide (**Fig. 4.3-6a**). Planar glide is facilitated by a low SFE and nitrogen, which both promote planar glide of

dislocations by reducing the ability of a material to cross slip; in accordance to the characteristics observed in the Fe-14Cr-16Mn-0.3C-0.3N [76] and Fe-2Cr-15Mn-0.6C-0.1N [217] alloys. The activation of cross slip in high nitrogen steels occurs only over short range distance [71][197][218]. The transition between stage A and B is reported to correspond to the onset of deformation twinning [12], the formation of SFs and the evolution of planar dislocation slip due to Cr-N SRO with increase in nitrogen concentration, as reported by Jung *et al.* [217]. In the investigated alloys, the nearly constant stage B hardening is assumed to be associated with the probability of Cr-N SRO and its assistance of planar glide. However, further TEM analysis needs to be carried out in order to investigate the existence of deformation twinning in this SH stage. Within stage C the SHR steadily decreases. Up to at least 0.31 logarithmic strain the fraction of deformation twins increases slightly (as can be seen in the deformation microstructure of comp II in **Fig. 4.3-6b**+**c**), likely facilitated by increasing stress and dislocation density [195]. The observed mechanical twinning is mainly confined to one preferred twin system, which can be attributed to primary twinning initiated in the lower stress regime at around ε=0.14 [60][217]. As can be seen from the IPF maps of comp II in **Fig. 4.3-7**, with increasing strain, more grains show orientation between the <001>//TA and <111>//TA direction, characteristic for grains with a well-developed twin substructure of at least one active twinning system [13]. For the low-nitrogen alloys of comp I and II a second inflection occurs in the SH stage C, which is referred as stage C'. After [217] stage C' is characterized by active secondary mechanical twinning and less active primary twinning. Likewise, Jin and Lee [219] suggest the existence of a single intermediate hardening stage is due to less active secondary mechanical twinning in Fe-Mn-C-Al TWIP steels. This is in agreement to the experimental observation from comp III. With increasing the SFE to 31 mJ/m² by enhancing the alloying content of manganese and nitrogen in comp III, the onset of deformation twinning is shifted to higher strain levels and the deformation twinning is shown to originate prevalently in one twin system (**Fig. 4.3-8b**). In this case, the SH stage C' is not observed (**Fig. 4.4-1c**). Other authors explain planar slip and the resulting anisotropic and homogeneously spread of dislocation substructures as a sufficient condition for the linear hardening behavior in *fcc* materials [52]. The decreasing effective SHR over stage C can be discussed after Feaugas [220] as a result of the enhanced dynamic competition between storage and annihilation of dislocations, pronounced due to the nitrogen assisted development of a fine deformation substructure. The high dislocation activity is further indicated to enhance glide plane softening diminishing the hardening effect of deformation twinning [221][222]. According to Müllner *et al.* [66], nitrogen changes the glide distribution leading to an increased local dislocation density. By that, mechanical twinning not only occurs earlier but also at more positions causing a finer deformation substructure. A reduced twin thickness with increasing nitrogen content is also reported by Jung *et al.* [217] in austenitic stainless steels. Thinner twins provide stronger barriers for dislocation glide with more dislocation pile-ups required to generate the required stress to propagate dislocations across the twin leading to increased SH level. In stage D the twin fraction and thickness of twin bundles increases significantly and twinning occurring in more than one active twin system is more dominant (**Fig. 4.3-6d** and **Fig. 4.3-7d**), which contributes to the large post uniform elongation. The development of intense dislocation accumulations within the refined microstructure results in pronounced deformation localization, which finally leads to the samples fracture [12]. In the SH behavior of the high alloyed comp III stage D hardening is not clearly defined from stage C (**Fig. 4.4-1c**). This can be explained due to the suppressed deformation twinning in favor of dislocation glide, attributed to the high SFE, which may intensify the deformation localization resulting in sudden fracture. Increased dislocation accumulation during deformation attributed to the dendritic

microstructure is further believed to suppress stage D hardening of the as-cast material and leads to general lower elongation in comparison to the cold-rolled/RX material (**Fig. 4.4-1a**+**c**). The effect of the cast-microstructure and, particularly, the influence of the dendritic arm spacing λ_2 on mechanical properties have been investigated in various studies. It was found that UTS and elongation decrease with increasing dendritic arm spacing [18]. This correlates with the results for comp I and II in the current work (Tab. 4.4-1), while the low total elongation of comp III is explained by a high amount of detected manganese-sulphides. Heat transfer conditions during the strip-casting process play a major role for the evolution of morphological structure parameters like grain size and dendritic arm spacing. Therefore, further investigations need be carried out in order to control the casting process with respect to the microstructure and mechanical properties of the material. In comparison to conventional nickel-containing stainless steels the strip cast Fe-Cr-Mn-N steels show quite promising mechanical characteristics already in the as-cast condition. Mechanical twinning has been identified as the main secondary deformation mechanism of the investigated Fe-Cr-Mn-N alloys at RT. The interstitial nitrogen strongly influences the activation of deformation twinning, by affecting the SFE. Due to the nitrogen alloying the deformation substructure is characterized by a local increased dislocation density causing a fine deformation twin structure. The occurrence of Cr-N SRO phenomena [14][15][16] and the resultant interactions with dislocations and stacking faults [75], are further believed to play a major role in the deformation behavior of these alloys.

In comparison to conventional high-Mn TWIP steels, the investigated high nitrogen alloys exhibit extra-ordinary high flow stress and strain hardening behavior. The effect of nitrogen alloying on the SHR in Fe-Cr-Mn steels is discussed in comparison to other high-manganese TWIP steels. **Fig. 5.2-2** shows the stress strain curves and SHR for different high manganese systems with similar interstitial content compared to the investigated Fe-13Cr-25Mn-0.6N alloy (comp III).
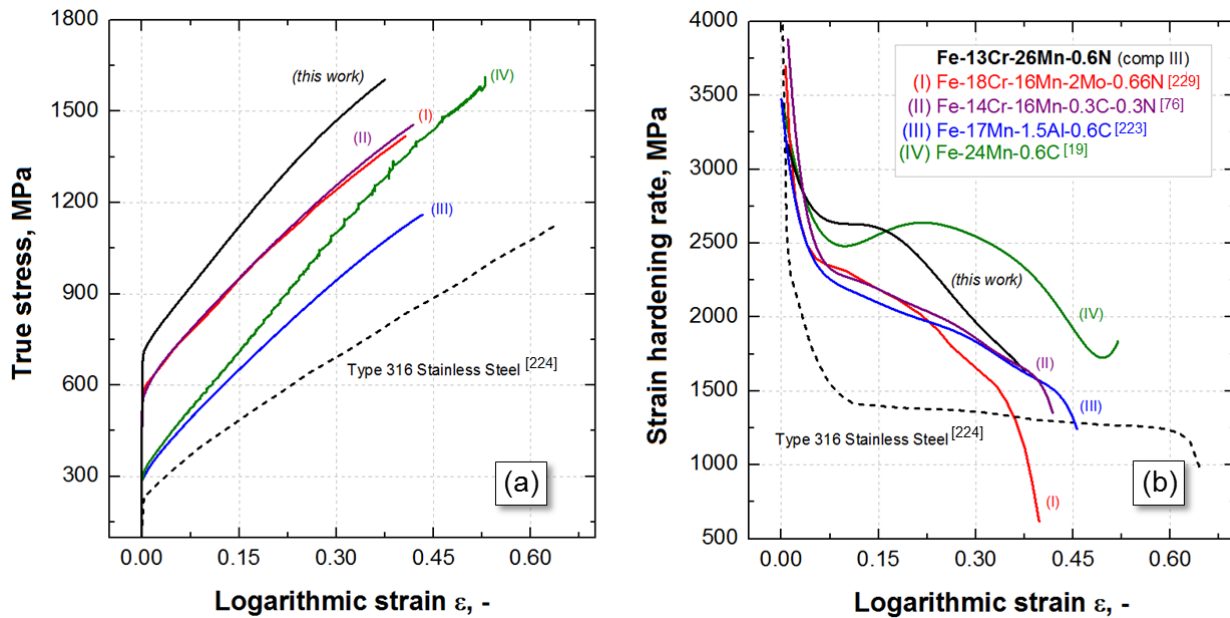

Fig. 5.2-2 Stress-strain curves (a) and strain hardening rates (b) for different high-Mn systems FeMnC [19], FeMnAlC [223], FeCrMnCN [76] and the FeCrMnMoN [229] compared to the investigated Fe-13Cr-25Mn-0.6N alloy (comp III) and the type 316 stainless steel [224].

The contribution of deformation twinning is reflected in the high SH of steel I-IV and the investigated alloy of comp III, where mechanical twinning is the main secondary deformation mechanism. The SHR of the type 316 stainless steel, where strain induced formation of α'(*bct*) martensite occurs, exhibits quite lower SH. The flow stress of the Fe-13Cr-25Mn-0.6N alloy (comp III) is superior to the considered steels in the initial (YS) and intermediate stages of deformation. This can be attributed to the larger solid solution strengthening of N relative to C [203], the Cr-N SRO [24][212] and the effect of nitrogen on the dislocation glide distribution, causing a finer deformation twin structure that leads to increased strengthening; as discussed earlier in this section. After Terazawa *et al.* [45], the observed planar dislocation glide in high nitrogen steels is suggested to cause marked stress concentration at the grain boundaries which results in high grain boundary hardening and increased strengthening [45]. While in nitrogen free austenitic steels cross-slip of screw dislocations is more likely to occur, resulting in the formation of dislocation cells [13], dynamic softening (recovery) contributes to the lower yield strength. After Karaman *et al.* [71], Cr-N SRO increases the twinning stress as the SRO zone needs to be destroyed in the successive twin planes during twin growth, which induces general high SH. The effect of SRO on SH was in detail investigated by Saeed-Akbari *et al.* [19] to explain the variations in the SHR diagrams of iso-SFE Fe-Mn-C TWIP steels. An empirical criterion for the possibility and population density of Mn-C SRO was proposed. The so-called theoretical ordering index (TOI = x_C/x_{Mn}) was defined as semi-empirical dimensionless parameter and calculated as relative molar fraction of carbon and manganese atoms in different Fe-Mn-C steels. With respect to the strong affinity between chromium and nitrogen atoms, the TOI of Cr-N SRO in Fe-Cr-Mn-N steels can be estimated using the same approach. In Tab. 5.2-1 the TOI and SFE of alloy I-IV and the Fe-13Cr-25Mn-0.6N alloy (comp III) are listed. According to the discussion in Chapter 5.2.1 on the type of SRO in carbon and nitrogen alloyed steels, the TOI of Mn/C and Cr/N are differentiated, while for di-interstitial Fe-14Cr-16Mn-0.3C-0.3N alloy II only Cr-N SRO is assumed [76].

Tab. 5.2-1 Mechanical properties, calculated SFE and TOI of the as-cast/hot-rolled and cold-rolled/RX strip material of comp IC.

Alloy	Chemical Composition, wt.%					SFE	TOI	
	Cr	Mn	Mo/*Al	N	C	mJ/m²	Cr/N, -	Mn/C, -
this work	13	25	-	0.61	0.10	31	0.17	-
I	18	16	2.2	0.66	-	25	0.14	-
II	14	16	-	0.30	0.30	21 (±6)*	0.08	-
III	-	17	*1.5	-	0.60	29 *	-	0.16
IV	-	24	-	-	0.60	31	-	0.11

* experimentally measured SFE

The SH curve of the Fe-24Mn-0.6C alloy shows distinct parabolic behavior in the intermediate and final stages of deformation in comparison to the Fe-13Cr-25Mn-0.6N alloy (**Fig. 5.2-2b**). The calculated SFE for both alloys is 31 mJ/m². One main reason is the occurrence of serrated yielding or DSA in Fe-Mn-C systems, as described earlier (Chapter 5.2.1). The DSA results in inhomogeneous plastic flow and unstable flow behavior that significantly enhances the strain hardening [21][197][225]. The DSA is suppressed in the aluminum alloyed Fe-17Mn-1.5Al-0.6C steel causing the divergent trend of the flow and SH curve after YS (**Fig. 5.2-2a**). Revealing similar SFE and TOI, the SHR of the Fe17-Mn-1.5Al-0.6C and Fe-13Cr-26Mn-0.6N alloys are substantially different. The difference in the SH behavior is attributed to the interstitial alloying with carbon and nitrogen,

assumed to change the evolution and characteristics of the dislocation and deformation twin substructures. In this regard, differences in the interaction between dislocations and SF may be related to the type of SRO. This could also explain the clearly improved flow stress and the SRH of the Fe-13Cr-25Mn-0.6N alloy in comparison to the Fe-14Cr-16Mn-0.3C-0.3N alloy. The mechanical properties of the cold-rolled/RX laboratory strip cast alloys of comp III, with YS ~ 660 MPa and $Tel(A_{50})$ ~ 47%, met the requirements for the application in automobile industry. While the total elongation of comp I+II and IC with $Tel(A_{50}) > 40\%$ is sufficient, the YS of ~550 MPa is deficient, due to the low nitrogen contents. Improvement of the yield strength can be obtained by adjusting the cold-rolling and recrystallization conditions. The strategies discussed in Chapter 2.1.2 are: grain size refinement, pre-straining of the cold-rolled/RX material and control of the recovery/ partial recrystallization annealing conditions of pre-strained sheets [52]. The YS as function of grain size follows the standard Hall-Petch relation [27]. With decreasing the mean grain size the yield strength of the material can be effectively increased. However, the reduction in grain size is dependent on the industrial process limitations for the respective production line [52]. The grains size further controls the deformation twin evolution and the dynamic recovery; by that affecting the work hardening behavior. With decrease in the mean grain size of austenitic TWIP steels the strength increases, while the elongation decreases, which is due to the suppressed dynamic recovery and deformation twinning, respectively [19][54][94]. By applying a defined degree of pre-straining/ cold deformation, the yield strength can be improved with respect to the remained ductility [55][226]. Additional annealing treatment to obtain subsequent recovery or partial recrystallization can be used to tailor the mechanical properties [52][57]. By that the formability of pre-strained sheets is enhanced without significantly reducing the yield strength. The ideal yield strength to ductility relation results from a combination of high cold rolling reduction and annealing at the lower limit of partial recrystallization [94]. Intensive research is required to identify the optimal conditions for the Fe-Cr-Mn-N steels.

5.2.3 Normalized yield strength - Thermal activation of dislocation glide

Interstitial elements in solid solution, such as nitrogen, and to a lesser extent carbon, in austenitic stainless Fe-Cr-Mn steels play a major role in the activation of deformation twinning, by influencing the SFE, and in the modification of the dislocation dynamics in these alloys [52]. In this regard, the YS is the most representative parameter to define the thermal activated nature of dislocation motion with respect to the effect of interstitial nitrogen [52]. The normalized YS (normalized by the room temperature YS), which excludes microstructural or solid solution hardening effects, is plotted as function of temperature in **Fig. 5.2-1** for the designed Fe-Cr-Mn-N steels. In order to discuss the effect of nitrogen on the dislocation glide dynamics, the normalized YS is furthermore plotted for various Fe-Mn-C alloys [52][227], conventional type 316 stainless steel [224][228], the high-nitrogen Fe-18Cr-16Mn-2Mo-0.7N alloy [229], the recently developed di-interstitial Fe-14Cr-16Mn-0.3C-0.3N alloy [76] and the interstitial free Fe-14Cr-14Mn-2Cu alloy. As presented by Allain *et al.* [52][227], the Fe-Mn-C alloys reveal very similar activation transition temperatures, defining the transition from thermally to athermal activated dislocation motion with increase in temperature (**Fig. 5.2-1**, grey area). Within the thermal activated range the temperature sensitivity is strongly influenced by the carbon content while the manganese content and the magnetic state have no significant effect [227]. In the athermal range the influence of temperature and carbon content is low, indicated by a minor slope above RT of -0.25. The change in the yield strength at these temperatures is attributed to the linear decrease of the elastic bulk modulus with increasing temperature and to the occurrence of strain aging that favors an increase in yield strength in the considered temperature range [169][227].
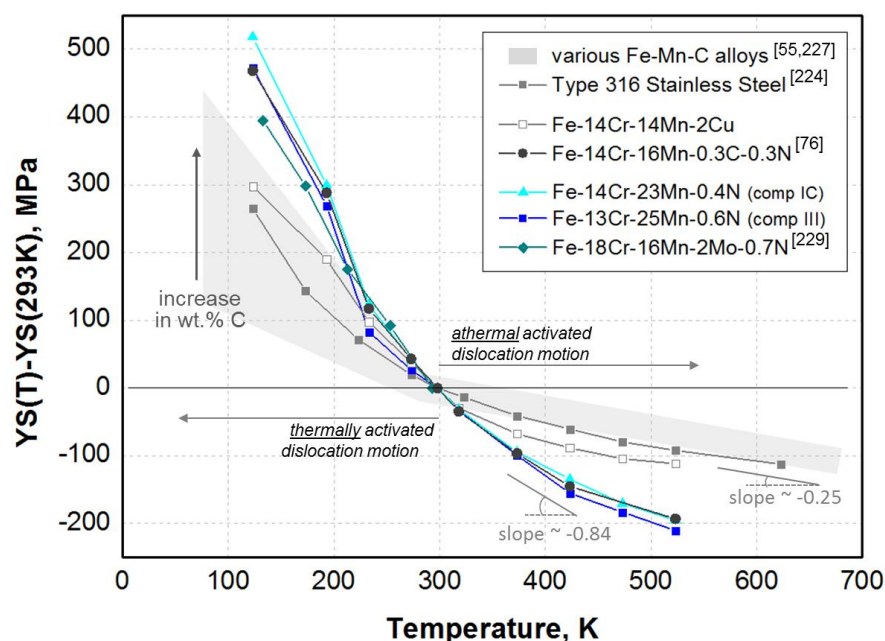
Fig. 5.2-1 Normalized yield strength (YS) as function of temperature for the investigated alloys of comp III and comp IC in comparison to the overall trend of various Fe-Mn-C steels [52][227], type 316 stainless steel [224], the high-nitrogen Fe-18Cr-16Mn-2Mo-0.7N alloy [229], the di-interstitial Fe-14Cr-16Mn-0.3C-0.3N [76] and interstitial-free Fe-14Cr-14Mn-2Cu alloy.

The investigated Fe-Cr-Mn-N alloys exhibit high temperature sensitivity in the variation of YS, both within the thermal and athermal temperature range (slope~-0.84), while the transition temperature is comparable to the alloys in the Fe-Mn-C system. Reported by Byrnes *et al.* [24], the significant high athermal flow stress in high-nitrogen austenitic stainless steels is attributed to Cr-N SRO, increasing with N content [24]. It is assumed that the SRO zones locally increase the elastic shear modulus and induce anisotropic elastic strain in the nearest surrounding of nitrogen atoms. The Cr-N SRO induced increase in strength was verified by Zhou and Grujicic [230] using a statistical thermodynamics based model of SRO. Compared to the Fe-Mn-C alloys, the slope of YS as a function of temperature for the Fe-Cr-Mn-N alloys is more pronounced at lower temperatures, as result of the solid solution strengthening of interstitial N, which is approximately 40% more effective than C [231], influencing the thermally activated dislocation glide dynamics [24]. Due to the increased conduction electrons around the nitrogen atoms compared to carbon [47], nitrogen atoms carry an effective negative electric charge, whereas the cores of screw dislocations reveal shortage of electrons. The resultant large electrostatic attraction between the nitrogen atoms and dislocations leads to enhanced binding and increased sensitivity of the thermally activated dislocation motion in comparison to Fe-Mn-C alloys. The effect of nitrogen on temperature dependence of the thermal stress was identified for the strengthening at low temperatures rather than its role in promoting the SRO [230]. Alloying carbon and nitrogen is found to increase the YS similar to nitrogen, which can be confirmed by the identical slope of YS over temperature for the Fe-13Cr-26Mn-0.6N alloy of comp III and the Fe-14Cr-16Mn-0.3C-0.3N, with the same total interstitial content. However after Gavriljuk *et al.* [47][48], the synergistic enhanced solid solution strengthening of carbon and nitrogen alloying is more effective than alloying with only nitrogen or carbon. In that regards, the carbon/nitrogen ratio of 0.5 was found

to be more favorable for stabilizing the austenite phase than 1.0 [48], which might explain the current results. The results on the interstitial free Fe-14Cr-14Mn-2Cu alloy and the type 316 stainless steel showing a similar trend of the YS(T)-YS(293K) over temperature as the Fe-Mn-C alloys, support the discussion on Cr-N SRO complexes dominating the dislocation dynamics in these materials, rather than Mn-C SRO. These finding are of major importance particularly for the analysis of di-interstitial carbon and nitrogen austenitic steels [230].

5.2.4 Temperature effect on strain hardening and mechanical properties

The influence of temperature on the flow behavior, strain hardening (**Fig. 4.4-3**) and mechanical properties (**Fig. 4.4-4**) was investigated on the cold-rolled/RX material of the industrial strip-cast alloy Fe-14Cr-22Mn-0.4N (comp IC). In the tested temperature range between -150°C to 100°C mechanical twinning is the dominant secondary deformation mechanism. The SHRs of the samples tested from in this temperature range exhibit remarkable similarity, characterized by a single intermediate hardening stage. The SFE ranges about 19 to 34.5 mJ/m^{-2} (**Fig. 5.1-2**). In the low-SFE range deformation twinning occurs gradually over the entire deformation process, while the majority of mechanical twin formation and mechanical twinning in multiple slip systems occurred at high strain level (compare **Fig. 4.3-6**; comp II). This leads to a homogeneous strain-hardening, prolongation of local necking, and enhanced of the post-uniform elongation [232]. The flow stress for samples tested at -150°C and -100°C are significantly larger than at the higher test temperatures. This temperature range corresponds to the region of thermally activated dislocation motion where larger stresses are required for dislocation glide, enhancing the flow stress. Minor traces of ε(*hcp*) martensite have been detected at both temperatures (**Fig. 4.3-11a+b**, white arrows). In this temperature region the estimated SFE values are near 19 mJ/m^{-2} (**Fig. 5.1-2**), which is close to the transition between the activation of TRIP and TWIP mechanism (estimated with 17±0.5 mJ/m²), promoting the formation of strain-induced ε(*hcp*) martensite besides mechanical twinning. Previous investigations on a Fe-22Mn-3Al-3Si alloy indicates dislocation cross slip is strongly impeded at low SFE [90]. The reduced ability for dislocation cross slip and the formation of ε(*hcp*) martensite laths acting as barriers to dislocations gliding on other slip system [90], further hinder dislocation mobility and are likely enhancing the flow stress, while the elongation is reduced. The hardening associated with the formation of ε(*hcp*) martensite typically occurs in the early and intermediate ranges of strain [85] which may reduce the capacity for the steel to further harden after uniform elongation, resulting in the lower post uniform elongation values at -150°C. The flow stresses and SHR rates corresponding to samples tested from 100 to 250°C exhibit similar behavior in stage (I) but different characteristics in the intermediate and final SH stages compared to samples tested at temperatures from -150 to 45°C. At approximately 0.1 logarithmic strain the SHR of the samples tested from 100 to 250°C experience an inflection followed by a rapid decrease in the strain-hardening rate. A second inflection in the SHR occurs at logarithmic strains of approximately 0.25, that is thought to correspond to the onset of mechanical twinning and its associated contribution to hardening [90][195]. The investigated alloy Fe-14Cr-22Mn-0.4N appears to show optimized ductility between -40°C and 45°C. In this range the highest twin activity was observed corresponding to the SFE calculated between 21-29 mJ/m², typical for low SFE high-Mn TWIP steels [232][233]. The increase in temperature delays the onset of mechanical twinning by reducing the flow stress, increasing the rate of dislocation annihilation and increasing the SFE, which raises the critical stress for activating mechanical twinning [195]. Consequently, as temperature increases lower twin fractions are observed (**Fig. 4.3-11d-f**) and mechanical twinning becomes progressively suppressed in favor of

pure dislocation glide. At temperature of 250°C, where the stress and elongation values are almost constant only minor mechanical twinning is observed, while some grains exhibit intense slip markings (**Fig. 4.3-11f**). The reduction in mechanical twinning with increasing temperature causes a slight reduction in TE. In comparison, the hardening contribution due to mechanical twinning is almost completely suppressed in lower C TWIP alloys at 200°C, such as Fe-17Cr-7Mn-3Ni-0.2N [228] and Fe-25Mn-3Al-3Si [232][90], which results in a remarkable decrease in TE. The occurrence of high temperature deformation twinning in the Fe-14Cr-22Mn-0.4N alloy may be attributed to the effect of nitrogen on the dislocation arrangements (dislocation-solute interactions) and the probability of Cr-N SRO affecting the deformation substructure (thinning of mechanical twins) and increasing the austenitic phase stability. It can be assumed that with increasing the interstitial nitrogen content and the probability SRO, correlated to the TOI and the relative Cr/N concentration, the effect of SFE on the activity and character of the mechanical twins becomes less important. Thereby, the strain hardening and ductility revealed constant high values over a wide range of temperature between -100°C and 100°C, compared to other austenitic stainless steels [76][228].

5.3 Materials design of Fe-Cr-Mn-N alloys for strip casting

The materials design of high nitrogen austenitic stainless steels considers the two main aspects for the materials production of these alloys via strip casting: (1) adjustment and prediction of the nitrogen solubility in the melt at atmospheric pressure and (2) control of the phase stabilities with respect to the suppression of the delta-ferrite region during solidification.

In this work, the effect of various parameter was determined to calculate the *nitrogen solubility* in the melt as function of chemical composition and temperature within the Fe-Cr-Mn-N system with small additions of 0.5 wt.% nickel and 0.1 wt.% carbon. One main aspect of the model development for nitrogen solubility calculations is the reliable thermodynamic description of the interaction parameter between Mn and N, to control the formation of nitride inclusions [162]. According to Shin *et al.* [162], the reported e_N^{Mn} differ in terms of the absolute values from -0.01 to 0.04 at 1873 K and the temperature dependency of e_N^{Mn} is not sufficiently described, particularly for high manganese contents. In the developed model, the first order interaction parameter in the range of -0.023 was identified to sufficient predict the nitrogen solubility in Fe-Mn alloys with up to 35 wt.% manganese. The second order interaction parameter r_N^{Mn} was found to play a major role, as it defines the deflection of the solubility curve especially at higher manganese content. Using the proposed r_N^{Mn} after Satir *et al.* [32][34] and Christmann *et al.* [163] the calculated nitrogen solubility at 1786 K was highly overestimated for manganese contents from 20 wt.% (**Fig. 4.2-3**). Adding chromium to the Fe-Mn system increases the nitrogen solubility [6][38]. The effect of chromium on the nitrogen solubility was reported to be two times stronger than the effect of manganese [32]; reflected in the e_N^{Cr} parameter that is double the value of the e_N^{Mn} and r_N^{Cr} to be four times the value of r_N^{Mn} (Tab. 4.2-2). To imply the temperature dependency between manganese and nitrogen in Fe-Mn-N melts, Shin *et al.* [162] proposed a temperature dependent interaction parameter $e_N^{Mn}(T)$, valid for high manganese TRIP, TWIP added steels and Mn-N-alloyed stainless steels. According to Shin *et al.* [162] the activity coefficient of manganese and by that the nitrogen solubility increases with temperature in low-manganese alloy melts. However in high-manganese alloy melts the activity coefficient of manganese decreases with increase in temperature, resulting in a decrease of nitrogen solubility (**Fig. 4.2-4a-c**). The inflection to decreasing nitrogen solubility at high manganese contents with increase in temperature was described to occur around 12 wt.% manganese, based on experimental [162][234] and theoretical observations [235][236]. In this work, the interaction

parameter after Rasev and Ivanov [160] have been found to accurately reproduce the temperature effect of manganese on the nitrogen solubility for the relevant melting temperatures during strip casting of the designed Fe-Cr-Mn-N alloys (compare **Fig. 4.2-4d** and Tab. 4.2-3).

The control of the phase stabilities during solidification is of main importance for the alloy design of Fe-Cr-Mn-N steels. As described in Chapter 4.2.1, the solidification through the liquid/δ-ferrite/austenite regions, associated with the formation of δ-ferrite, results in a wide nitrogen solubility gap, formation of pores and outgassing of nitrogen, which leads to degraded surface quality of the strip and the loss of nitrogen in the austenitic microstructure [28]. With increased chromium content, the δ-ferrite solidification region is extended (**Figure 5.3-1**). In order to suppress the δ-ferrite solidification, the chromium content needs to keep low. Though, with decreasing chromium content a distinct loss of the nitrogen solubility in the melt occurs. To meet the industrial requirements for automotive application of Fe-Cr-Mn-N alloys, a minimum chromium content of 13 wt.% is required to ensure a sufficient ability for nitrogen solubility and appropriate wet-corrosion resistance. **Figure 5.3-1** represents the nitrogen solubility limit (max/min) within the liquid/austenite solidification region as function of chemical composition. For alloys with chromium contents of 13 wt.%, a stable liquid/austenite solidification is achieved for manganese contents of at least 19 wt.%. With increasing the alloying content of manganese, the liquid/austenite solidification area expands with respect to the max/min limits of the nitrogen content. A wide liquid/austenite solidification area offers the best conditions in terms of technical feasibility for the strip-casting process, as variations in the process temperature, pressure or impurities in the melt influence the phase equilibrium. For Fe-Cr-Mn-N alloys with 13 wt.% chromium content, the 2D-SFE map is shown in **Figure 5.3-2** as function of chemical composition. The red colored area indicates the area of validity for the materials design of high nitrogen stainless steels for strip casting. For the base alloy design of Fe-13Cr-19Mn a stable liquid/austenite solidification is reached for nitrogen contents between 0.44-0.46 wt.%. Increasing the alloying content of chromium and/or manganese will further increase the resultant nitrogen concentration and overall limits. It can be concluded that Fe-Cr-Mn-N alloys suitable for strip casting are characterized by content as materials of single austenitic phase with high SFE that show TWIP effect and/or deformation by pure DG. A characteristic TRIP effect was not observed for these materials.

Industrial strip-cast lines are combined with an inline hot-rolling step of the strip-cast sheet material. With the hot-rolling the two strip shells are consolidated, solidification pores are closed and the microstructure is fined due to dynamic recrystallization. The hot workability during strip casting of high nitrogen steels strongly depends on the content of additional elements. Impurities that segregate at the grain and solidification boundaries, e.g., sulphur, phosphorus and oxygen decrease the hot workability [237].The effect of impurities on the workability is much stronger in the case of solidification to austenite; causing edge cracking of the strip during hot rolling and effect adversely toughness [6]. After [237], theses impurities are introduced into the melt with the charge, metallic and non-metallic additions during melting and with the secondary treatment of the molten steel. With the increasing use of steel scrap, the content of some impurities has increased and there removal requires additional processing. However, in order to obtain good hot workability auf high nitrogen austenitic stainless steels the amount of hot workability reducing elements need to be kept low [6]. Therefore the steel making process plays a major role.
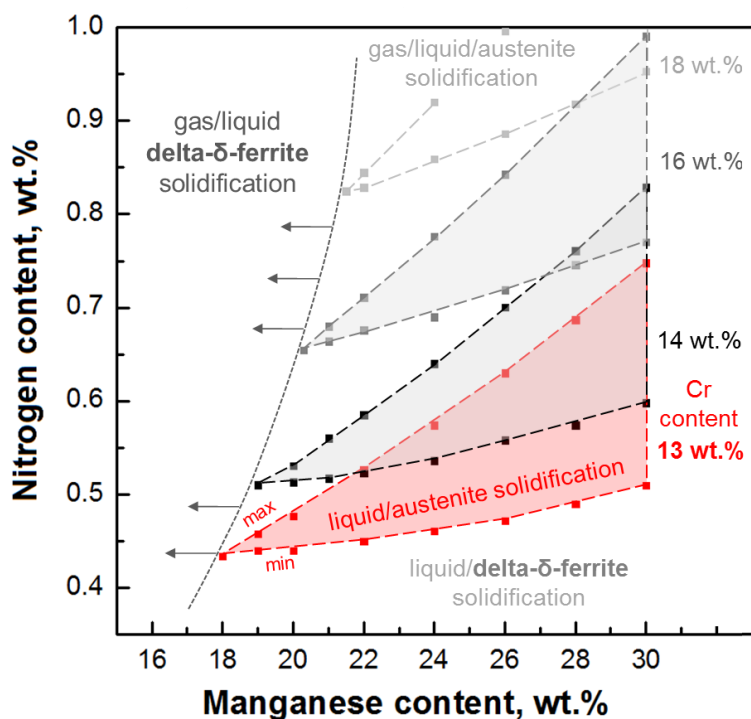
Figure 5.3-1 Nitrogen solubility limit (max/min) within the liquid/austenite solidification region as function of chemical composition.
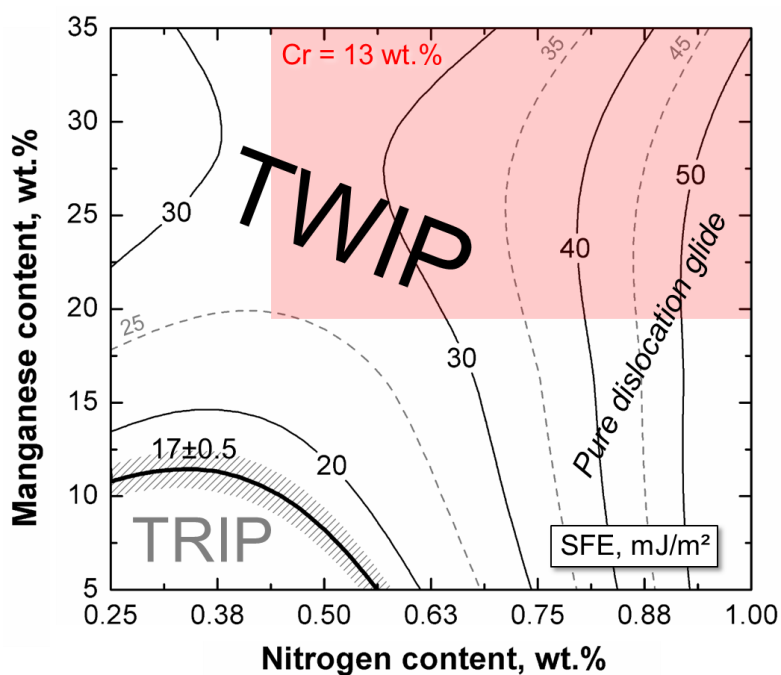

Figure 5.3-2 SFE-map for the Fe-13Cr-Mn-N system, showing the area of validity (red colored) for the materials design of high nitrogen stainless steels that fulfill the conditions for strip casting.

5.4 Strip-cast vs. continuous-cast alloy

Thin strip casting of austenitic stainless steels offers a number of significant advantages in comparisons to the conventional slab cast method, Chapter 2.1.1. Based on the alloying concept of comp I, a continuous-cast slab was produced at Outokumpu Nirosta GmbH, Sweden. The slab was hot-rolled to 3.3 mm and solution annealed, further cold-rolled to a final thickness of 1.0 mm and recrystallization annealed. In Table 5.4-1 the nominal compositions and the mechanical properties of the cold-rolled/RX strip material are listed in comparison to the strip-cast material of comp I.

Table 5.4-1 Chemical compositions and mechanical properties of the cold-rolled/RX strip-cast and continuous-cast material of the investigated alloy design of comp I.

Comp	Chemical composition, wt.%					Mechanical properties			
						YS*	UTS	UE	TE**
	Cr	Mn	Ni	C	N	[MPa]	[MPa]	[%]	[%]
target	13.0	20.0	0.50	0.10	0.43 ±0.05				
I	12.7	19.2	0.55	0.09	0.40	540	910	50	53
CC	13.1	20.0	0.19	0.08	0.43	530	860	43	54

*YS at 0.2% strain, ** A_{50} samples DIN 50114*

The nominal composition of the continuous-cast material is in accordance to the target chemical composition. The proposed solubility model within this work, accurately predicts the equilibrium nitrogen solubility in the melt, even for different production routs (Chapter 4.2.2). The mechanical properties of the cold-rolled/RX CC strip is comparable to the strip-cast material. Differences are observed for the UTS and UE that can be explained due to the observed macrosegregation, **Figure 5.4-1**. The intense formation of segregation bands is known to occur for high manganese steels [238]. Variations in the local chemical composition further leads to differences in the deformation microstructure. Within the segregation bands, deformation twinning seems to be increased, indicated in **Figure 5.4-1b** (white arrow). As a result, pronounced deformation localization causes irregular hardening, reduced uniform elongation and early necking. While the rapid solidification during strip casting enables the production of high manganese steels with improved macrostructure homogeneity and reduced anisotropy [35][36]. In this study the mechanical properties of the strip-cast material have been found to be superior to the continuous-cast materials, strengthening the high potential for the production of austenitic stainless Fe-Cr-Mn-N steels via thin strip-casting.
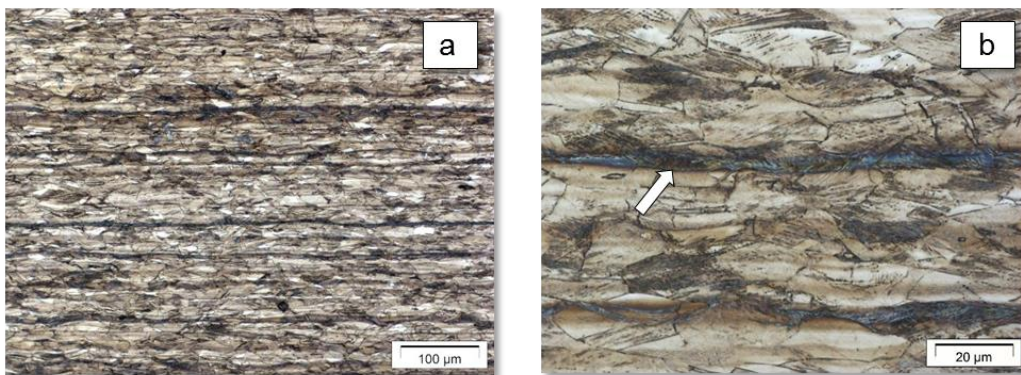

Figure 5.4-1 Deformation microstructure of the cold-rolled/RX continuous-cast material with different magnification of (a) 200x and (b) 1000x.

6 Summary

High nitrogen manganese austenitic stainless TWIP steels exhibit exceptional combination of high strength, ductility and excellent strain hardening behavior that offer high potential for application e.g. in car bodies. The application of austenitic Fe-Cr-Mn-N steels in automobile industry is yet limited mainly due to the higher production costs. High nitrogen steel melting methods are generally associated with high pressures to enhance the nitrogen solubility in the melt. Moreover, the phase stabilities during solidification of the cast materials needs to be controlled with respect to the suppression of the delta-ferrite region associated with the formation of pores and outgassing of nitrogen. Thin strip casting offers an attractive option that not only shortens the process route but also allows the alloying with nitrogen within the equilibrium solubility at atmospheric pressure. In the reported work, the materials design of high nitrogen Fe-Cr-Mn-N austenitic steels for strip casting was presented. To meet the industrial application and economic requirements, the materials design approach was defined by the three main parts: (1) prediction and control of the thermal und mechanical phase stability using CALPHAD based methods, (2) defining the boundary conditions for the materials production via strip casting, and (3) adjustment and characterization of the mechanical properties, flow and work hardening behavior.

A CALPHAD based method was used and evaluated for the Fe-Cr-Mn-N system by the state of the art approaches to derive deformation mechanism maps from thermodynamics based stacking fault energy (SFE) calculation. In order to consider higher order interactions and the effect of interstitial nitrogen on the thermal and mechanical phase stability, the sublattice model has been applied for the $\Delta G^{\gamma \to \varepsilon}$ calculation in this work, rather than the simplified subregular model. The currently available thermodynamic data for the calculation of $\Delta G^{\gamma \to \varepsilon}$ have been found to accurately define the upper limit of $\varepsilon(hcp)$ martensite formation across a broad range of chemical compositions. The interaction parameter between chromium and nitrogen, $L^{(fcc)}_{Cr,Fe:N}$ and $L^{(fcc)}_{Cr,Fe:N,Va}$, were adjusted to reproduce experimental observations. It appeared that manganese and nitrogen both stabilize the *fcc* phase. However, adding chromium to the system results in the stabilization of the *fcc* phase at low nitrogen contents, while at higher nitrogen contents, the *hcp* phase becomes more favorable. This was explained by the thermodynamic description of the *hcp* phase as Cr_2N nitride. The two common methods for the SFE calculation in the Fe-Cr-Mn-N system using (1) a constant interfacial energy to calculate SFE_{linear} and (2) including a segregation term to determine SFE_{segr} were discussed and found not to suitable reproduce the non-monotonous effect of nitrogen on SFE. Therefore a composition-dependent description of the interfacial energy, $\sigma^{\gamma/\varepsilon}_{comp}$, was proposed to calculate SFE_{comp} that could be successfully assigned for the activation of deformation induced twinning in Fe-Cr-Mn-N stainless steels. The model validity was set to the following range of chemical compositions: nitrogen 0.23-1.0 wt.%, chromium 0-25 wt.%, and manganese 5-30 wt.%. Furthermore, the influence of the coherency strain energy E_{strain} on the stacking fault energy was investigated that plays a major role for the validation between experimental and theoretical estimated SFE values. The contribution of E_{strain} to the fault energy arises from the additional strains, necessary to complete the *fcc* to *hcp* transformation. Considering E_{strain} a shift in the calculated $SFE_{effective}$ relative to the SFE_{comp} values was observed, that was more dominant in the TWIP region, than in the TRIP region. This result has been explained by the change in the description of the $\sigma^{\gamma/\varepsilon}_{comp}$ over manganese, with the effect of manganese on $\sigma^{\gamma/\varepsilon}_{comp}$ to become more significant if E_{strain} is considered. The dependency of SFE over temperature has been identified to exhibit a linear behavior

at T>RT. While at T<RT the contribution of magnetic ordering has to be considered that resulting in distinct deviation from the linear relation between SFE and temperature.

High nitrogen Fe-Cr-Mn stainless TWIP steels with nominal chemical composition in the range of 13-14 wt.% Cr, 20-26wt.% Mn and 0.4-0.6 wt.% N were successfully melted and processed by strip casting in laboratory and industrial scale. Based on thermodynamic methods the solubility of nitrogen in the melt and the phase stability during solidification at atmospheric pressure were accurately predicted as function of balanced chromium to manganese concentration, in order to prevent pore formation. In the model development for the nitrogen solubility calculations, the first order interaction parameter between manganese and nitrogen, e_N^{Mn}, was evaluated with respect to control the formation of nitride inclusions, particularly for high manganese contents. The e_N^{Mn} in the range of -0.023 has been identified to sufficient predict the nitrogen solubility in Fe-Mn alloys with up to 35 wt.% manganese. The second order interaction parameter r_N^{Mn} was found to play a major role, as it defines the deflection of the solubility curve especially at higher manganese content. In the presented model, the effect of chromium on the nitrogen solubility has been identified to be two times stronger than the effect of manganese, which is in accordance to various literature. To control of the phase stabilities during solidification, the phase equilibria in the Fe-Cr-Mn-N system were calculated and presented as isoplethal phase diagram over temperature and nitrogen content. It was shown that with increased chromium content, the δ-ferrite solidification region was extended, resulting in a wide nitrogen solubility gap. However, with decreasing chromium content a distinct loss of the nitrogen solubility in the melt occurred. Industrial requirements for automotive application of Fe-Cr-Mn-N alloys assume a minimum chromium content of 13 wt.%, necessary to ensure a sufficient ability for nitrogen solubility and appropriate wet-corrosion resistance. For chromium contents of 13 wt.%, a stable liquid/austenite solidification was achieved for at least 19 wt.% of manganese content. It was concluded that <u>Fe-Cr-Mn-N alloys suitable for strip casting are characterized by content as materials of single austenitic phase with high SFE that show TWIP effect or deformation by pure DG</u>. A characteristic TRIP effect was not observed for these materials.

The deformation mechanisms and mechanical properties of the investigated Fe-Cr-Mn-N alloys were discussed to depend on temperature, SFE and ordered microstructural phenomena like short range ordering (SRO). In the temperature range between -150 to 250°C the flow behavior of the analyzed steels was homogenous and no serrations in the flow stress occurred during tensile deformation. The absence of dynamic strain aging was attributed to the type of SRO and the activation energy for reorientation of the point defects, rather than the SFE. The RT SFE of the examined steels could be determined to be in the range of 24-31 mJ/m² which defines mechanical twinning as the dominant secondary deformation mechanism in these steels resulting in high work hardening rate and formability. The strain hardening rate (SHR) of the as-cast and cold-rolled/RX strip material showed differences in the level and the shape of the strain hardening curve for all the investigated alloys. The observed characteristics in the strain hardening behavior were attributed to the change in grain size, differences in the density and distribution of the dislocation substructure and the critical stress for the onset of deformation twinning. In the cast-microstructure the dendritic microsegregations within the austenitic grains have been discussed to act as additional phase boundaries, besides the twin substructure, leading to a more effective reduction in the dislocation mean free path and by that acting as strong barriers to the dislocation glide and deformation twin growth, leading to high SH level. Deformation twins were found to preferentially originate at the grain boundaries, penetrating the dendritic areas with further growth, regardless of the microsegregations. Hence, besides grain boundaries, areas of low-SFE were assumed to act as potential twin nucleation sites in the as-cast

material. In the cold-rolled condition, the designed alloying concepts showed excellent mechanical properties with YS up to 660 MPa and total elongation A_{50} of 47 %, meeting the requirements for application in automobile industry. Distinct temperature sensitivity of the yield strength within the thermal and athermal temperature range was observed and attributed to N additions and Cr-N SRO. The RT SH behavior was found mainly controlled by dislocation glide at low strain, competition between dislocation dynamics and mechanical twinning in the intermediate strain regime and mechanical twinning and dislocation accumulation at fracture strain. For the low-nitrogen alloys a second inflection in the SH occurred that was characterized by active secondary mechanical twinning. In the high alloyed material with 0.61 wt.% nitrogen, the observed mechanical twinning was mainly confined to one preferred twin system, which has been attributed to primary twinning initiated in the lower stress regime. The decreasing effective SHR was discussed as a result of the enhanced dynamic competition between storage and annihilation of dislocations, pronounced due to the nitrogen assisted development of a fine deformation substructure. In accordance to literature, nitrogen changes the glide distribution leading to an increased local dislocation density. By that, mechanical twinning not only occurs earlier but also at more positions causing a finer deformation substructure. Thinner twins provide stronger barriers for dislocation glide with more dislocation pile-ups required to generate the required stress to propagate dislocations across the twin, leading to increased SH level with higher nitrogen contents. In comparison to conventional high-Mn TWIP steels, the investigated high nitrogen Fe-Cr-Mn alloys exhibit extra-ordinary high flow stress and strain hardening behavior. This was attributed to the larger solid solution strengthening of N relative to C, the occurrence of Cr-N SRO and the effect of nitrogen on the dislocation glide distribution, causing a finer deformation twin structure that leads to increased strengthening. In this study the mechanical properties of the strip-cast material have been found to be superior to the material produced as continuous-cast slab.

The influence of temperature on the flow behavior, strain hardening and mechanical properties was investigated on the industrial strip-cast alloy Fe-14Cr-22Mn-0.4N. In the tested temperature range between -150°C to 100°C mechanical twinning is the dominant secondary deformation mechanism, with SFE between 19 to 34.5 mJ/m^{-2}, respectively. The SHRs were characterized by a single intermediate hardening stage. Deformation twinning was found to occur gradually over the entire deformation process, leading to homogeneous strain-hardening, prolongation of local necking, and enhanced of the post-uniform elongation. The highest twin activity and ductility was observed in the intermediate temperature interval from -40 to 45°C with the SFE ranging from 21 to 29 mJ m^{-2}, respectively. Significant high flow stress was observed in the region of thermally activated dislocation glide, contributing to the strain hardening at low temperatures in the range of -150°C and -100°C. With increase in temperature the onset of mechanical twinning was delayed reducing the flow stress and increasing the rate of dislocation annihilation. The occurrence of high temperature deformation twinning at 250°C was attributed to the effect of nitrogen on the dislocation arrangements and the probability of Cr-N SRO. It was assumed that with increasing the interstitial nitrogen content the effect of SFE on the activity and character of mechanical twinning becomes less dominant. In comparison to conventional austenitic stainless steels and high-manganese steels the Fe-Cr-Mn-N alloys exhibit constant high values of strain hardening and ductility over a wide range of temperature.

7 Appendix

Tab. 4.4-3 Mechanical properties of the as-cast/hot-rolled and cold-rolled/RX strip-cast material of comp IC tested in 0°, 45° and 90° to rolling direction.

Composition				Mechanical properties			
				YS^*	UTS	A_u	Tel^{**}
	Condition			[MPa]	[MPa]	[%]	[%]
	as-cast/hot-rolled		0°	716	876	24	33
			45°	663	838	25	35
			90°	662	828	26	30
IC	*cold-rolled/RX*	B	0°	489	820	42	54
			45°	491	834	38	44
			90°	497	842	42	48
		E	0°	518	852	44	51
			45°	515	852	42	49
			90°	518	864	42	48

* YS at 0.2% strain, ** A_{30} samples DIN 50114, B/E...begin/end of strip

8 List of nomenclature

α	…	*bcc* phase/ martensite
α'_D	…	deformation induced *bcc/bct* martensite
β	…	total dislocation character angle
β^Φ	…	total magnetic entropy
γ	…	*fcc* phase/ austenite
γ^T	…	mechanical twinning
γ^∞	…	interfacial energy per unit area of the interface
δ	…	*bcc* phase/ delta-ferrite
ε	…	*hcp* phase/ epsilon martensite
ε_D	…	deformation induced *hcp* martensite
ε_S	…	strain normal to the fault plane
λ_2	…	secondary dendrite arm spacing
μ	…	shear modulus
ν	…	Poisson's ratio
ρ	…	molar surface density along {111} planes
ρ_A	…	density of atoms in a closed packed plane in moles per unit area
σ	…	interfacial energy per unit area of the interface boundary
$\sigma^{\gamma/\varepsilon}$	…	interfacial energy of the γ/ε-interface
Λ_N	…	interaction energy of nitrogen atoms with dislocations in the *fcc* structure
Φ	…	phase
$\Omega^{\varepsilon\rightarrow\gamma}$	…	interaction parameter of the excess Gibbs free energy term in the subregular model
bcc	…	body centered cubic
bct	…	body centered tetragonal
fcc	…	face centered cubic
hcp	…	hexagonal close-packed
a_γ	…	lattice parameter of austenite
a_N	…	chemical activity of nitrogen in solution
a,c	…	site numbers in each sublattice
b_p	…	Burgers vector of a partial dislocation
d_{actual}	…	actual partial dislocation separation
comp	…	composition (alloys I-III,IC)
$e_N^{(X)}$	…	first order interaction parameter of the alloying element X with the concentration [%X]
f_N	…	activity coefficient
$f_N^{(T)}$	…	f_N with temperature correction term (for T other than 1600°C)
p_{N_2}	…	partial pressure of nitrogen in the surrounding gas atmosphere
$r_N^{(X)}$	…	second order interaction parameter of the alloying element X with the concentration [%X]
s	…	interplanar spacing
va	…	vacancies
x_i	…	molar fraction of element i

List of nomenclature

x_N ... molar fraction of nitrogen in the bulk

$x_{s(N)}$ ... molar fraction of nitrogen at the stacking faults

$y_{i,j}$ ... site fractions of the component i,j (i,j = Fe, Mn, Cr)

y_N ... site fraction of nitrogen in the interstitial sublattice with vacancies

y_{va} ... site fraction of vacancies in the interstitial sublattice

A ... interfacial area

AOD ... argon oxygen decarburization

CC ... continuous cast alloy

DG ... dislocation glide

EBSD ... electron back-scatter diffraction

EPMA ... electron probe microanalysis

ERS ... electro slag remelting furnace

E_{strain} ... coherent strain energy

FESEM ... field emission scanning electron microscopy

G^{Φ} ... Gibbs free energy of phase Φ

$G^{\Phi}_{i:va}$ ... Gibbs free energy in which all interstitial sites are filled with nitrogen

$G^{\Phi}_{i:N}$ ... Gibbs free energy of the pure elements in a hypothetical nonmagnetic state

G^{Φ}_{chem} ... chemical Gibbs free energy

G^{Φ}_{excess} ... contribution to the Gibbs free energy due to the interactions between different elements

G^{Φ}_{magn} ... contribution to the Gibbs free energy due to magnetic ordering

$\Delta G^{\gamma \to \varepsilon}$ ... effective Gibbs free energy for the $\gamma \to \varepsilon$ phase transformation

$\Delta G^{\gamma \to \varepsilon}_{segr}$ ... segregation free energy term

$\Delta G^{\gamma \to \varepsilon}_{chem}$ ... chemical free energy due to Suzuki segregation

$\Delta G^{\gamma \to \varepsilon}_{surf}$ ... surface free energy due to the difference in concentration of nitrogen between matrix and stacking faults

$\Delta G^{\gamma \to \varepsilon}_{elast}$ ... elastic free energy related to the segregation of substitutional and interstitial elements with different atomic sizes

G^M_V ... Gibbs free energies per unit volume of the matrix

G^{SFP}_V ... Gibbs free energies per unit volume of SFP

HIP ... hot isostatic processing

IC ... industrial strip-cast alloy

IPF ... inverse pole figure (map) determined by EBSD

IQ ... image quality (map) determined by EBSD

L ... interaction parameters in the excess Gibbs energy term

LOM ... light optical microscopy

RX ... recrystallized microstructure

SFE ... stacking fault energy

SFE_{comp} ... SFE with $\sigma^{\gamma/\varepsilon}$ as function of chemical composition

$SFE_{effective}$ ... SFE_{comp} including E_{strain}

SFE_{linear} ... SFE with $\sigma^{\gamma/\varepsilon}$ as constant value

SFE_{segr} ... SFE with $\sigma^{\gamma/\varepsilon}$ as constant value, including $\Delta G^{\gamma \to \varepsilon}_{segr}$

SFP ... stacking fault phase

SGTE   … Scientific Group Thermodata Europe
SH   …strain hardening
SHR   …strain hardening rate
SRO   … short range ordering
R   … ideal gas constant
ΔR   … constitutes of yield strength
R_i, R_o … inner and outer radius of curvature of the node
RT   … room temperature
T   … temperature
TA   … tensile axis
TE   … total elongation
TOI   … theoretical ordering index
T^{Φ}_{Neel} … critical temperature for the anti-ferromagnetic ordering
T_{liq} … liquidus temperature
T_{sol} … solidus temperature
TEM   … transmission electron microscopy
TWIP   … twinning induced plasticity
UE   … uniform elongation
UTS   … ultimate tensile strength
V^{SFP} … volume of the stacking fault phase
WBBF   … weak-beam bright-field
YS   … yield strength
[%N]   … concentration of dissolved nitrogen
[%X]   … concentration of substitutional element X (X= Cr, Mn, Ni, ….)

9 Literature

[1] M.O. Speidel, Mat Wiss Werkstofftech 37 10 (2006) 875-80.

[2] K.H. Lo, C.H. Shek, and J.K.L. Lai: Mater Sci Eng R 65 (2009) 39-104.

[3] T.H. Lee, C.-S. Oh, S.-J. Kim, and S. Takaki, Acta Mater 55 (2007) 3649-62.

[4] R.P. Reed, JOM 41 3 (1989) 16-21.

[5] O. Bouaziz, C.P. Scott, G. Petitgand, Scripta Mater 60 (2009) 714-716.

[6] H. Hänninen, J. Romu, R. Ilola, J. Tervo, and A. Laitinen, J. Mater. Process. Tech. 117 (2001) 424-30.

[7] L.M. Roncery, S. Weber, W. Theisen, Metall. Mater. Trans. A 41 (2010) 2471-2479.

[8] S.R. Chen, H.A. Davis, W.M. Rainforth, Acta Mater. 47 18 (1999) 4555-4569.

[9] H. Takahashi, Y. Shindo, H. Kinoshita, T. Shibayama, S. Ishiyama et al., J. Nuclear Mater. 258-263 (1998) 1644-1650.

[10] V.V. Naumenko, A.P. Shlyamnev, G.A. Filippov, Metallurgist, 55 5-6 (2011) 410-418.

[11] S. Allain, J.P. Chateau, O. Bouaziz, S. Migot, N. Guelton, Mater. Sci. Eng. A 387-389 (2004) 158-162.

[12] D. Barbier, N. Gey, S. Allain, N. Bozzolo, M. Humbert, Mater. Sci. Eng. A 500 (2009) 196-206.

[13] I. Gutierrez-Urrutia, D. Raabe, Acta Mater. 59 (2011) 6449-6462.

[14] K. Oda, N. Kondo, K. Shibata, ISIJ Int. 30 (1990) 625-631.

[15] J. Rawers, G. Slavens, J. Mater. Eng. Perform. 4 (1995) 697-708.

[16] V.V. Sumin, G. Chimid, T. Rashev, L. Saryivanov, Mater. Sci. Forum 318-320 (1999) 31-40.

[17] Y.P. Li, J.S. Yu, S. Kurosu, Y. Koizumi, H. Matsumoto, A. Chiba, Mater. Chem. Phys. 133 (2012) 29-32.

[18] K. Jeong, J.E. Jin, Y.S. Jung, S. Kang, Y.K. Lee, Acta Mater. 61 (2013) 3399-3410.

[19] A. Saeed-Akbari, L. Mosecker, A. Schwedt, W. Bleck: Metall Mater Trans A 43 (2012) 1688-1704.

[20] Y.N. Petrov, Z. Metallkd. 94 (2003) 1012-1016.

[21] V. Gavriljuk, Y. Petrov, B. Shanina, Scripta Mater. 55 (2006) 237-240.

[22] D. Jandová, J. Řehoř, Z. Nový, J. Mater. Process. Tech. 157-158 (2004) 523-530.

[23] I.A. Yakubtsov, A. Ariapour, D.D. Perovic, Acta Mater. 47 (1999) 1271-1279.

[24] M.L.G. Byrnes, M. Grujicic, W. S. Owen, Acta Metall. 35 (1987) 1853-1862.

[25] C.C. Bampton, I.P. Jones, M.H. Loretto, Acta Mater. 26 (1978) 39-51.

[26] T. Hickel, S. Sandlöbes, R.K.W. Marceau, A. Dick, I. Bleskov et al., Acta Mater. 75 (2014) 147-155.

[27] J.W. Simmons, Mater. Sci. Eng. A207 (1996) 159-169.

[28] H.K. Feichtinger, G. Stein, Mater. Sci. Forum 318-20 (1999) 261-270.

[29] G. Balachandran, M.L. Bhatia, N.B. Ballal, P.K. Rao, ISIJ Int. 41 9 (2011) 1018-1027.

[30] K. Skuin, R. Simmchen, M. Gunzel, C. Voigt, G. Riedel, H. Werner, Werkst.Korros. 43 (1992) 206-214.

[31] J.N. Tarboton, L.M. Matthews, A. Sutcliffe, C.M.P. Frost, J.P. Wessels, Mater. Sci. Forum 318-320 (1999) 777-784.

[32] A. Satir-Kolorz, H.K. Feichtinger, M.O. Speidel, Gießereiforschung 42 1 (1990) 36-49.

[33] A. Satir-Kolorz, H.K. Feichtinger: Z. Metallkde. 82 (1991) 689-97.

[34] A. Satir-Kolorz, H.K. Feichtinger, M.O. Speidel, Gießereiforschung 41 4 (1989) 149-64.

[35] N. Zapuskalov, ISIJ Int. 43 8 (2003) 1115-1127.

[36] M. Daamen, S. Richter, G. Hirt: Key Eng Mat 554-557 (2013) 553-561.

[37] D. Raabe, R. Degenhardt, R. Sellger, W. Klos, M. Sachtleber, L. Ernenputsch, Steel Res. Int. 79 6 (2008) 440-444.

[38] T. Schubert, W. Löser, S. Schinnerling, I. Bächer, Mater. Sci. Tech. 11 (1995) 181-185.

[39] A. Jahn, A. Kovalev, A. Weiß, P.R. Scheller, S. Wolf et al., ESOMAT 2009 05013.

[40] S. H. Wang, Z. Y. Liu, W. N. Zhang, G.H. Wang, J. L. Liu et al., ISIJ Int. 49 (2009) 1340-1346.

[41] Z.Y. Liu, Z.S. Lin, S.H. Wang, Y.Q. Qiu, X.H. Liu et al., Mater. Charact. 58 (2007) 974-979.

[42] M.O. Speidel, HNS 88, Proc. of the 1st Int Conf HNS: The Institute of Metals 92-96.

[43] M.A.E. Harzenmoser, Massiv aufgestickte austenitische-rostfreie Stähle und Duplexstähle, Ph.D. Thesis, TH Zürich, Schweiz, 1959.

[44] P.J. Uggowitzer, M. Harzenmoser, HNS 88, Proc. of the 1st Int Conf HNS: The Institute of Metals 174-179.

[45] Y. Terazawa, T. Ando, T. Tsuchiyama, S. Takaki, Steel Res. Int. 80 7 (2009) 473-476.

[46] Q.X. Dai, A.D. Wang, X.N. Cheng, L. Cheng, Mater. Sci. Eng. A 311 (2001) 205-210.

[47] V.G. Gavriljuk, V.N. Shivanyuk, B.D. Shanina, Acta Mater. 53 (2005) 5017-5024.

[48] V.G. Gavriljuk, B.D. Shanina, H. Berns, Mater. Sci. Eng. A 481-482 (2008) 707-712.

[49] K.O. Bazaleeva, Met. Sci. Heat Treat. 47 (2015) 455-461.

[50] V.G. Gavriljuk, H. Berns, High Nitrogen Steels, Berlin Heidelberg: Springer-Verlag; 1999.

[51] S. Lin, H. Ledbetter, Mater. Sci. Eng. A 167 (1993) 81-85.

[52] O. Bouaziz, S. Allain, C. P. Scott, P. Cugy, D. Barbier, Curr. Opin. Solid St. M. 15 (2011) 141-168.

[53] G. Dini, A. Najafizadeh, R. Ueji, S.M. Monir-Vaghefi, Mater Design 31 7 (2010) 3395-3402.

[54] R. Ueji, N. Tsuchida, D. Terada, N. Tsuji, Y. Tanaka, et al., Scripta Mater. 59 (2008) 963-966.

[55] L.P. Karjalainen, T. Taulavuori, M. Sellman, A. Kyröläinen, Steel Res. Int. 79 (2008) 404-412.

[56] S. Kang, Y.S. Jung, J.H. Jun, Y.K. Lee, Mater Sci Eng A 527 (2010) 745-751.

[57] C. Haase, L.A. Barrales-Mora, F. Roters, D.A. Molodov, G. Gottstein, Acta Mater. 80 (2014) 327-340.

[58] L. Mosecker, A. Saeed-Akbari, Sci. Technol. Adv. Mater. 14 (2013) 1-14.

[59] A. Dumay, J.P. Chateau, S. Allain, S. Migot, O. Bouaziz, Mater. Sci. Eng. A 483-484 (2008) 184-187.

[60] T.H. Lee, E. Shin, C.S. Oh, H.J. Ha, S.J. Kim, Acta Mater. 58 (2010) 3173-3186.

[61] G. Saller, K.S.-Hahn, C. Scheu, H. Clemens, Mater. Sci. Eng. A 427 (2006) 246-254.

[62] S. Kibey, J.B. Liu, M.J. Curtis, D.D. Johnson, H. Sehitoglu, Acta Mater. 54 (2006) 2991-3001.

[63] B.X. Huang, X.D. Wang, L. Wang, Y.H. Rong, Metall. Mater. Trans. 39A (2008) 717-724.

[64] L. Bracke, G. Mertens, J. Penning, B.C. De Cooman, M. Liebeherr, N. Akdut, Metall. Mater. Trans. 37A (2006) 307-317.

[65] L. Bracke, J. Penning, N. Akdut, Metall. Mater. Trans. 38A (2007) 520-528.

[66] P. Müllner, C. Solenthaler, P. Uggowitzer, M.O. Speidel, Mat. Sci. Eng. 164A (1993) 164-169.

[67] R.J. Ilola, H.E. Hänninen, K.M. Ullakko, SIJ Int. 36 (1996) 873-877.

[68] R.E. Schramm, R.P. Reed, Metall. Mater. Trans. 6A (1975) 1345-1351.

[69] R.E. Stoltz, J.B. Vander Sande, Metall. Mater. Trans.11A (1980) 1033-1037.

[70] Y.K. Lee, J. Mater. Sci. Lett. 21 (2002) 1149-1151.

[71] I. Karaman, H. Sehitoglu, H.J. Maier, Y.I. Chumlyakova, Acta Mater. 49 (2001) 3919-3933.

[72] Y.N. Petrov, Scripta Mater. 53 (2005) 1201-1206.

[73] T.H. Lee, H.Y. Ha, B. Hwang, S.J. Kim, E. Shin, Metall. Mater. Trans. 43A (2012) 4455-4459.

[74] H. Suzuki, Sci. Rep. Res. Inst. Tohoku Univ. 4 (1952) 455-463.

[75] P.A. Flinn, Acta Metall. Mater. 6 (1958) 631-635.

[76] L. Mosecker, D.T. Pierce, A. Schwedt, M. Beighmohamadi, J. Mayer, et al., Mater. Sci. Eng. A 642 (2015) 71-83.

[77] L. Vitos, J.O. Nilsson, B. Johansson, Acta Mater. 54 (2006) 3821-3826.

[78] A. Dick, T. Hickel, J. Neugebauer, Steel Res. Int. 80 (2009) 603-608.

[79] K. Ishida, Phys. Status Solidi 36A (1976) 717-728.

[80] A.P. Miodownik, CALPHAD 2 (1978) 207-226.

Literature

[81] P.J. Ferreira, P. Müllner, Acta Mater. 46 (1998) 4479-4484.

[82] Q.X. Dai, A.D. Wang, X.N. Cheng, X.M. Luo, Chin. Phy. 11 (2002) 596-600.

[83] F.B. Pickering, Physical metallurgical development of stainless steels. In: G.L. Dunlop (Ed.), Proceedings of the Stainless Steels 84, Chalmers University of Technology, Goteborg: The Institute of Metals; 1985.

[84] J.Y. Choi, J.H. Ji, S.W. Hwang, K.T. Park, Mater. Sci. Eng. A 528 (2011) 6012-6019.

[85] D.T. Pierce, J.A. Jiménez, J. Bentley, D. Raabe, C. Oskay and J.E. Wittig, Acta Mater. 68 (2014) 238-253.

[86] A. Kibey, Mesoscale models for stacking faults, deformation twins and martensitic transformation: Linking atomistics to continuum, Ph.D. Thesis, University of Illinois at Urbana-Champaign, Urbana, Illinois, 2007.

[87] P.Y. Volosevich, V.N. Gridnev, Y.N. Petrov, Phys. Met. Metallogr. 42 (1976) 372-376.

[88] M. J. Whelan, Proc. Roy. Soc. 249 (1959) 114-137.

[89] A.W. Ruff, K.L. Ives, Acta Metall. Mater. 15 (1967) 189-198.

[90] D. Pierce, The Influence of Manganese Content and Temperature on the Relative FCC/HCP Phase Stability and Strain-Hardening Behavior of High-Manganese TRIP/TWIP Steels, Ph.D Thesis, Vanderbilt University, Nashville, TN, 2014.

[91] J. P. Hirth, Theory of Dislocations, 2nd ed., John Wiley and Sons, 1982.

[92] H.M. Otte, J. Appl. Phys. 38 (1967) 217-222.

[93] R.P. Reed, R.E. Schramm, J. Appl. Phys. 45 (1974) 4705-4711.

[94] G. Dini, R. Ueji, A. Najafizadeh, S.M. Monir-Vaghefi, Mater. Sci. Eng. A 527 (2010) 2759-2763.

[95] G.B. Olsen, M. Cohen, Metall. Trans. 7A (1976) 1897-1923.

[96] S.M. Cotes, A. Fernández Guillermet, M. Sade: Metall. Mater. Trans. A 35 (2004) 83–91.

[97] W. Huang: CALPHAD 13 (1989) 243-252.

[98] D. Djurovic, B. Hallstedt, J. v Appen, R. Dronskowski: CALPHAD 35 (2011) 479-491.

[99] J. Miettinen, Calphad 23 2 (1999) 231-248.

[100] S. Curtze, V.T. Kuokkala, A. Oikari, J. Talonen, H. Hänninen, Acta Mater. 59 (2011) 1068-1076.

[101] L. Mujica, S. Weber, W. Theisen, Mater. Sci. Forum 706-709 (2012) 2193-2198.

[102] S. Lu, Q.M. Hub, B. Johansson, L. Vitos, Acta Mater. 59 (2011) 5728-5734.

[103] M. Hillert, L.I. Staffansson, Acta Chem. Scand. 24 (1970) 3618-3626.

[104] K. Frisk, K 1993 CALPHAD 17 (1993) 335-349.

[105] K. Frisk, Metall. Mater. Trans. 21A (1990) 2477-2488.

[106] C. Qiu, Metall Mater Trans A 24 (1993) 2393-2409.

[107] A.T. Dinsdale, CALPHAD 15 (1991) 317-425.

[108] O. Redlich, A.T. Kister, J. Eng. Chem. 40 (1948) 345-348.

[109] M. Hillert, M. Jarl, CALPHAD 2 (1978) 227-238.

[110] G. Inden, Bull Alloy Phase Diagrams 2 (1982) 412-422.

[111] K. Frisk, CALPHAD 15 (1991) 79-106.

[112] J. Nakano, Sci. Technol. Adv. Mater. 14 (2013) 014207.

[113] P.H. Adler, G.B. Olsen, W.S. Owen, Metall. Mater. Trans. 17A (1986) 1725-1737.

[114] A. Saeed-Akbari, J. Imlau, U. Prahl, W. Bleck, Metall. Mater. Trans. 40A (2009) 3076-3090.

[115] J. Nakano, P.J. Jacque: Calphad 34 (2010) 167-175.

[116] A. G. Svyazhin, J. Siwka and T. S. Rashev: Proc. 5th Int. Conf. On HNS, Mater., Sci. Forum, V. 318–320, Trans Tech. Pub. Ltd., Zürich, (1999), 131.

[117] E. Schürmann, H.D. Kunze, Gießereiforschung 19 (1967) 101-8.

[118] L. Remy, A. Pineau, Mat. Sci. Eng. 28A (1977) 99-107.

[119] U.R. Lenel, B.R. Knott, Metall. Mater. Trans. 18A (1987) 847-855.

[120] A. Nylas, B. Obst, Proceedings of the 1st Int Conf HNS: The Institute of Metals (1989) 194-198.

[121] Y. Kitamura, T. Tsuchiyama, H. Kikuchi, K. Suzuki, M. Okamura, Proceedings of the 2nd Int Conf HNS: Stahl und Eisen (1990) 171-176.

[122] M. Földéaki, H. Ledbetter, J. Magn. Mater. 110 (1992) 185-196.

[123] P.J. Uggowitzer, R. Magdowski, M.O. Speidel, ISIJ Int. 36 (1996) 901-908.

[124] J.B. Vogt, A. Messai, J. Foct, ISIJ Int. 36 (1996) 862-866.

[125] M. Onozuka, T. Saida, S. Hirai, M. Kusuhashi, I. Sato, T. Hatakeyama, J. Nucl. Mater. 255 (1998) 128-138.

[126] Y. Tomota, Y. Xia, K. Inoue, Acta Mater. 46 (1998) 1577-1587.

[127] Y. Tomota, J. Nakano, Y. Xia, K. Inoue, Acta Mater. 46 (1998) 3099-3108.

[128] D.J. Mills, R.D. Knutsen, Wear 215 (1998) 83-90.

[129] S.C. Liu, T. Hashida, H. Takahashi, H. Kuwano, Y. Hamaguchi, Metall. Mater. Trans. 29A (1998) 791-798.

[130] S. Liu, S. Liu, D. Liu, J. Mater. Sci. 39 (2004) 2841-2848.

[131] N.A. Sorokina, A.P. Shlyamnev, Met. Sci. Heat Treat. 41 (1999) 260-265.

[132] H. Okada, H. Sahashi, N. Igata, K. Miyahara, J. Alloy Compd. 355 (2003) 17-21.

[133] N. Efros, L. Korshunov, B. Efros, N. Chernenko, I. Loladze, Proceedings of the 7th Int Conf HNS: Steel Grips (2004) 391-394.

[134] A. Balitskii, Proceedings of the 7th Int Conf HNS: Steel Grips (2004) 585-589.

[135] S. Riedner, H. Berns, A.I. Tyshchenko, V.G. Gavriljuk, C. Schulte-Noelle, W. Trojahn, Materialwiss. Werkst. 39 (2008) 448-454.

[136] T.H. Lee, C.S. Oh, S.J. Kim, Scripta Mater. 58 (2008) 110-113.

[137] S.J. Kim, T.H. Lee, C.S. Oh, Steels Res. Int. 80 (2009) 467-472.

[138] B. Hwang, T.H. Lee, S.J. Park, C.S. Oh, S.J. Kim, Mater. Sci. Eng. 528A (2011) 7257-7266.

[139] B. Hwang, T.H. Lee, S.J. Kim, Proc. Eng. 10 (2011) 409-414.

[140] M. Milititsky, D.K. Matlock, A. Regully, N. Dewispelaere, J. Penning, H. Hanninen, Mater. Sci. Eng. 496A (2008) 189-199.

[141] K. Yang, Y. Ren, Sci. Technol. Adv. Mater. 11 (2010) 1-13.

[142] M. Xu, J. Wang, L. Wang, W. Cui, C. Liu, Adv. Mat. Res. 146 (2011) 26-33.

[143] J.Y. Choi, J.H. Ji, S.W. Hwang, K.T. Park, Mat. Sci. Eng. 528A (2011) 6012-6019.

[144] P. Neddermann: Evaluation of Stacking fault Energy by Computational Thermodynamics in the Fe-Cr-Mn-C System. Diploma thesis, RWTH University, Aachen, 2012.

[145] V.T. Witusiewicz, F. Sommer, E.J. Mittemeijer, J. Phase. Equilib. Diff. 25 4 (2004) 346-354.

[146] T. Gebhardt, D. Music, B. Hallstedt, M. Ekholm, I.A. Abrikosov, et al., J. Phys.: Condens. Matter. 22 (2010) 1-5.

[147] V. Dimova, I. Georgiev, I. Pechenyakov, R. Dobrev, Mater. Technol. 6 (1978) 9-14.

[148] B.J. Lee, Metall. Mater. Trans. 24A (1993) 1919-1933.

[149] A.F. Guillermet, P. Gustafson, High Temp. High Press. 16 (1985) 591-610.

[150] J.O. Andersson, A.F. Guillermet, P. Gustafson, CALPHAD 11 (1987) 361-364.

[151] A.F. Guillermet, W. Huang, Int. J. Themophys. 11 (1990) 949-969.

[152] C. Qiu, A.F. Guillermet, Z. Metallk. 84 (1993) 11-22.

[153] N. Saunders, A.P. Miodownik, A.T. Dinsdale, CALPHAD 12 (1988) 351-374.

[154] J.O. Anderson, Int. J. Thermophys. 6 (1985) 411-419.

[155] H.S. Yang, J.H. Jang, H.K.D.H. Bhadeshia, D.W. Suha, CALPHAD 36 (2012) 16-22.

[156] S. Allain, J.P. Chateau, O. Bouaziz, S. Migot, N. Guelton, Mater. Sci. Eng. A 387-389 (2004) 158-162.

[157] N.C. Santhi Srinivas, V.V. Kutumbarao, Scripta Mater. 37 (1997) 285-291.

[158] V.G. Gavriljuk, V.A. Duz, S.P. Yefimenko, O.G. Kvasnevskiy, Phys. Met. Metallogr. 64 (1987) 84-88.

[159] H. Schumann, J. Kristall Technik 9 (1974) 1141-1152.

[160] T. Rasev, R. Ivanov, Arch. Eisenhüttenwesen 50 (1979) 369-371.

[161] G.M. Grigorenko, Y.M. Pomarin, Sov. Tech. Rev. Weld. Surf. 1 (1990) 1-63.

[162] J.H. Shin, J. Lee, D.J. Min, J.H. Prak, Metall. Mater. Trans. B 42 (2011) 1081-85.

[163] K. Christmann, D. Senk, Proc. 2nd Int. Conf. on HMnS, Aachen, 2014.

[164] M.J. Peet, H.S.Hasan, H.K.D.H. Bhadeshia, Int. J. Heat. Mass. Tran. 4 (2011) 2602-2608.

[165] M. Dahmen, O. Güvenc, M. Bambach, G. Hirt, CIRP Annals 63 1 (2014) 265-268.

[166] D. Raabe, Acta Mater. 45 3 (1997) 1137-1151.

[167] L. Bracke, K. Verbeken, L. Kestens, J. Penning, Acta Mater. 57 (2009) 1512-1524.

[168] A.A. Gazder, A.A. Saleha, E.V. Pereloma, Scipta Mater. 68 (2013) 436-439.

[169] N.A. Tereshchenko, V.A. Shabashov, A.I. Urarov, Phys. Met. Metallogr. 109 (2010) 427-437.

[170] Q. Dai, Z. Yuan, X. Chen, K. Chen, Mater. Sci. Eng. A 517 (2009) 257-260.

[171] W.R. Osório, R.R. Goulart, G.A. Santor, C.M. Neto, A. Garcia, Metall. Mater. Trans. 37A (2006) 2525-2537.

[172] B. Sundman, J. Ågren, J. Phys. Chem. Solids 42 (1981) 297-301.

[173] De Cooman BC 2011 Proceedings of the Materials Research Society 1296 1439

[174] Y.K. Lee, J. Han, Mater. Sci. Technol. 31 7 (2015) 843-856.

[175] H. Feichtinger, A. Satir-Kolorz, X.O. Zheng, 1989 Proceedings of the 1st Int Conf HNS: The Institute of Metals 75-80.

[176] Y.K. Lee, C.S. Choi, Metall. Mater. Trans. 31A (2000) 355-360.

[177] A. Holden, J.D. Bolton, E.R. Petty, J .Iron Steel Inst. 209 (1971) 712-28.

[178] K. Ishida, Scripta Mater. 11 3 (1977) 237-242.

[179] M.C.Y. Lee, Metall. Mater. Trans. 24A (1993) 2379-2382.

[180] J.C. Fisher, Acta Metall. Mater. 2 (1954) 9-10.

[181] J. Kim, S.J. Lee, B.C. De Cooman, Scripta Mater. 65 (2011) 363-366.

[182] V.G. Gavriljuk, B.D. Shanina, H. Berns, Acta Mater. 48 (2000) 3879-3893.

[183] S.J. Lee, J. Kim, S.N. Kane, B.C. De Cooman, Acta Mater. 59 (2011) 6809-6819.

[184] V.M. Nadutov, Mat. Sci. Eng. 254A (1998) 234-241.

[185] M. Herbig, M. Kuzmina, C. Haase, R.K.W. Marceau, I. Gutierrez-Urrutia, et al., Acta Mater. 83 (2015) 37-47.

[186] C.G. Rhode, A.W. Thompson, Metall. Mater. Trans. 8A (1977) 1901-1906.

[187] H.M. Otte, Acta Metall. Mater. 5 (1957) 614-627.

[188] Y.H. Ha, T.H. Lee, C.S. Oh, S.J. Kim, Scripta Mater. 61 (2009) 121-124.

[189] C. Ko, R.B. McLellan, J. Phys. Chem. Solids 50 (1989) 619-622.

[190] S. Hertzmann, Metall. Mater. Trans. 18A (1987) 1753-1766.

[191] H. Du, M. Hillert, Z. Metallk. 82 (1991) 310-316.

[192] H. Du, J. Phase Equilib. 14 (1993) 682-693.

[193] F.K. Naumann, G. Langenscheid, Arch. Eisenhüttenwes. 36 (1965) 677-682.

[194] R.P. Reed, M.W. Austin, Scripta Metall. 23 (1989) 1359-1362.

[195] D.R. Steinmetz, T. Jäpel, B. Wietbrock, P. Eisenlohr, I. Gutiérrez-Urrutia, et al., Acta Mater. 61 (2013) 494-510.

[196] J. Talonen , H. Hänninen, Acta Mater. 55 (2007) 6108-6118.

[197] L. Chen, H.S. Kim, S.K. Kim, B.C. De Cooman, ISIJ Int. 47 (2007) 1804-1812.

[198] K. Renard, S. Ryelandt, P.J. Jacques, Mater. Sci. Eng. A 527 (2010) 2969-2977.

[199] S. Lee, J. Kim, S.J. Lee, B.C. De Cooman, Acta Mater. 65 (2011) 528-531.

[200] L.H. de Almeida, I. Le May, P.R.O. Emygdio, Mater. Charact. 41 (1998) 137-150.

[201] I.C. Jung, B.C. De Cooman, Acta Mater. 61 (2013) 6724-6735.

[202] D.W. Kim, W.S. Ryu, J.H. Hong, S.K. Choi, J. Mater. Sci. 33 (1998) 675-679.

[203] M. Ivanchenko, U. Ehrnstén, V. Nevadacha, Y. Yagodzinskyy, H. Hänninen, Proceedings of the 7th Int. Conf. of HNS 2004, Ostend, Belgium, 4 (2004) 641-649.

[204] G.V. Prasad Reddy, R. Sandhya, K. Bhanu Sankara Rao, S. Sankaran, Procedia Eng. 2 (2010) 2181-2188.

[205] S. Lee, J. Kim, S. Kim, K. Chin, B.C. De Cooman, Mater. Sci. Forum 654-656 (2010) 262-265.

[206] L. Bracke, Deformation Behavior of Austenitic Fe-Mn Alloys by Twinning and Martensitic Transformation, Ph.D. Thesis, Ghent University, Belgium, 2007.

[207] J. Xie, L. Teng, N. Chen, S. Seetharaman, Metall. Mater. Trans. A 41 (2010) 172-180.

[208] M. Grujicic, W.S. Owen, Acta Metall. Mater. 43 (1995) 4201-4211.

[209] W.S. Owen, M. Grujicic, Acta Mater. 47 (1999) 111-126.

[210] J. von Appen, R. Dronskowski, Steel Res. Int. 82 (2011) 101-107.

[211] A.G. Khachaturyan, Progress Mater. Sci. 22 (1978) 123-124.

[212] J.-H. Kang. T. Ingendahl, J. v. Appen, R. Dronskowski, W. Bleck, Mater. Sci. Eng. A 614 (2014) 122-128.

[213] R.B. Mclellan, Acta Metall. Mater. 30 (1982) 317-322.

[214] T. Murata, M. Sacamoto, Nitrogen-alloyed steels, fundamentals and application, AGNE Publishing Inc., 1997.

[215] E. Pereloma, D.V. Edmonds, Phase Transformations in Steels, 1st ed.,Woodhead Publishing, 2012.

[216] S.J. Lee, D. K. Matlock, C.J. Van Tyne, ISIJ Int. 51 (2011) 1903-1911.

[217] Y.S. Jung, S. Kang, K. Jeong, J.-G. Jung, Y.-K. Lee, Acta Mater. 61 (2013) 6541-6548.

[218] J. Oddershede, T. L. Christiansen, K. Ståhl, M.A.J. Somers, Scripta Mater. 62 (2010) 290-293.

[219] J.E. Jin, Y.K. Lee, Acta Mater. 60 (2012) 1680-1688.

[220] X. Feaugas, Acta Mater. 47 (1999) 3617-3632.

[221] F. Hamdi, S. Asgari, Metall. Mater. Trans. A 39 (2008) 294-303.

[222] J. Kang, F.C. Zhang, X.Y. Long, Z.N. Yang, Mater. Sci. Eng. A 610 (2014) 427-435.

[223] W. Song, T. Ingendahl, W. Bleck, Acta Metall. Sin. Engl. Lett. 27 (2014) 546-556.

[224] T.S. Byun, N. Hashimoto, K. Farrell, Acta Mater. 52 (2004) 3889-3899.

[225] B.C. De Cooman, O. Kwon, K.-G. Chin, J. Mater. Sci. Technol. 28 (2012) 513-527.

[226] P.J. Uggowitzer, M.O. Speidel, HNS 88, Proc. of the 1st Int Conf HNS: The Institute of Metals 156-160.

[227] S. Allain, O. Bouaziz, J.P. Chateau, Scripta Mater. 62 (2010) 500-503.

[228] A.S. Hamada, L.P. Karjalainen, R.D.K. Misra, J. Talonen, Mater. Sci. Eng. A 559 (2013) 336-344.

[229] W. Wang, W. Yan, K. Yang, Y. Shan, Z. Jiang, J. Mater. Eng. Perform. 19 (2010) 1214-1219.

[230] X.W. Zhou, M. Grujicic, CALPHAD 20 (1996) 257-272.

[231] K.J. Irvine, T. Gladman, F.B. Pickering, J. Iron Steel Inst. 207 (1969) 1017-1028.

[232] O. Grässel, L. Krüger, G. Frommeyer, L.W. Meyer, Inter. J. Plast. 16 (2000) 1391-1409.

[233] S. Curtze, V.T. Kuokkala, Acta Mater. 58 (2010) 5129-5141.

[234] S.Z. Beer: Trans. Metall. Soc. AIME 221 (1961) 2-8.

[235] E. Schürmann, W. Kättlitz: Arch. Eisenhüttenwesen 52 (1981) 219-24.

[236] H. Wada, S.W. Lee, R.D. Pehlke: Metall. Mater. Trans. B 17 (1986) 238-39.

[237] F. Tehovnik, F. Vodopivec, B. Arzensek, R. Celin, Metalurgija 49 1 (2010) 49-52.

[238] D. Senk, H. Emmerich, J. Rezende, R. Siquieri, Adv Eng Mater, 9 (2007), 695-702.